

# PHYSICAL REVIEW D

## PARTICLES AND FIELDS

THIRD SERIES, VOL. 4, No. 9

1 NOVEMBER 1971

### Properties of the $K^*(890)$ and $K^*(1420)$ in $K^-p$ Interactions at 3.9 and 4.6 GeV/c\*

M. Aguilar-Benitez, R. L. Eisner, and J. B. Kinson†

Brookhaven National Laboratory, Upton, New York 11973

(Received 10 June 1971)

Results are presented on the production and decay properties of the  $K(890)$  and  $K(1420)$  mesons as observed in  $K^-p$  interactions at 3.9 and 4.6 GeV/c. In addition, data on the elastic and charge-exchange reactions are also included. Total and differential cross sections, density-matrix elements, and  $S$ - $P$ -wave interference effects are discussed in detail for both neutral and charged modes of the  $K(890)$ . A measurement of the mass difference and comparison between the production properties of these two modes are presented. The mass and width parameters of the  $K(1420)$  meson and the possibility of the presence of more than one resonance in the 1400-MeV mass region are investigated. Branching ratios, total and differential cross sections, and a spin-parity determination are discussed.

#### I. INTRODUCTION

We have previously published several letters<sup>1</sup> concerning the production and decay properties of the  $K(890)$  and  $K(1420)$  bosons. The present work represents the amplification and completion of these studies as well as the presentation of additional data on the elastic and charge-exchange reactions.

In the past years numerous models have been proposed to explain hadron interactions.<sup>2</sup> A thorough comparison of these models with the quasi-two-body reaction,  $KN \rightarrow K^*(890)N$ , at intermediate and high energies has awaited an increase of statistics in these channels. In this study we present an investigation of both neutral and charged  $K^*(890)$  production. We have  $\sim 3000$  events in the  $K^-p \rightarrow K^*(890)n$  and  $\sim 4400$  events in the  $K^-p \rightarrow K^*(890)p$  final state. This large data sample, compared to previous investigations<sup>3</sup> in this energy region, allows a detailed study of the production and decay angular distributions of this resonance. We present, in addition, a determination of the mass difference between the neutral and charged  $K^*(890)$ . We also give a systematic investigation of the behavior of the  $S$ -wave background in the

$K^*(890)$  region.

Recent experimental results on the structure of the  $A_2(1300)$  meson have renewed interest in the properties of the other members of the  $2^+$  nonet. The resonance parameters – mass and width – and the possibility of fine structure in the  $K(1420)$  mass region have been studied for different final states. The greater statistical validity of our data allows us to use the charge-exchange reactions to measure the  $K(1420)$  decay branching ratios and to avoid channels in which the presence of the  $Q$  effect makes the results of any type of analysis particularly dubious. Total and differential cross sections for production of the  $K(1420)$  meson are also included. Finally, we discuss the  $J^P$  assignment of this resonance. A large sample of resonance events shows the presence of interference effects in their respective decay angular distributions, which makes a spin-parity analysis difficult; however, a selected sample of nonperipherally produced, charged  $K(1420)$  events allows us to favor strongly the  $J^P$  assignment  $2^+$  over  $1^-$  and  $3^-$ .

The selection of events and description of final states are given in Sec. II. In Sec. III we present data on the elastic and charge-exchange reactions.

The study of the  $K(890)$  and  $K(1420)$  mesons is presented in Sec. IV and V, respectively.

## II. DESCRIPTION OF FINAL STATES

### I. Event Selection

The data for this study come from exposures of the BNL 80-inch hydrogen bubble chamber to beams of  $K^-$  mesons at 3.9- and 4.6-GeV/ $c$  incident momenta. The events used for this paper come from the topologies listed in Table I. The corresponding events/ $\mu\text{b}^4$  given in the table have been corrected for scanning efficiency, film coverage, fiducial volume, and throughput efficiency. A cut on the proton length in the two-prong topology was imposed in order to eliminate the measurement of the copiously produced elastic events in the forward momentum-transfer region. The minimum projected length selected varied over the experiment from 3 to  $\sim 40$  mm.

The final states of interest for this study are enumerated in Table II (all reaction numbers in the text refer to this table). In the two-prong topology all events that fit the elastic scattering hypothesis were selected into reaction 1 with  $\chi^2$  probability greater than  $10^{-4}$ . Reactions 2 and 3 were chosen if their corresponding  $\chi^2$  probability was greater than that shown in Table II provided it was larger than any other one-constraint probability. Reaction 4 was selected with the indicated probability provided another one-constraint fit did not have a ten-times-larger probability. In addition, as with all other final states, ionization as measured by the BNL flying-spot digitizer (FSD) was required to be consistent with the kinematic track interpretation. The resulting  $\chi^2$ -probability distributions for reactions 2–4 were all consistent with being flat.

TABLE I. Microbarn equivalent of the different topologies used in the present study.

Topology	Events/microbarn	
	3.9 GeV/ $c$	4.6 GeV/ $c$
Two-prong	4.3	2.4
Two-prong + vee	6.6	7.4
Four-prong	6.4	3.6
Zero-prong + vee	2.6	4.0

The level of contamination in reactions 2–4 was estimated by investigation of the corresponding missing-mass-squared distributions, which are shown in Figs. 1–3 for all events that passed ionization criteria. After removal of elastic events, regardless of any other selection, all distributions are observed to center near the appropriate mass value with  $\sim 20\%$  estimated background in the region corresponding to our  $\chi^2$ -probability cuts. As can be seen, all peak regions in Figs. 1–3 are well separated from the multineutral thresholds (i.e.,  $2\pi^0$ ,  $\bar{K}^0 + \pi^0$ ,  $n + \pi^0$ ), which then provide small backgrounds into the chosen reactions. The observed spike at  $MM^2 \sim 0.0$  GeV $^2$  in Fig. 1 was attributed to elastic events which were either mismeasured or gave very low probability to hypothesis 1 of Table II. These events were found not to contribute to reaction 2 after the  $P_{\chi^2} > 10\%$  selection was imposed.

The main contamination into reactions 2 and 3 comes from the  $\pi^-p$  MM and  $K^-p$  MM channels, respectively, in which a large fraction of events had an outgoing positive track which had been identified as protons and in which the negative track could not be identified by ionization. The effect of

TABLE II. Experimental details of the final states used in the present study.

Topology	Final state	Prob. cut	Number of events		Reaction number
			3.9 GeV/ $c$	4.6 GeV/ $c$	
Two-prong	$K^-p \rightarrow K^-p$	$>10^{-4}$	9290 <sup>a</sup>	6084 <sup>a</sup>	1
	$K^-p \rightarrow K^-p\pi^0$	$>10\%$	3074	1794	2
	$K^-p \rightarrow \bar{K}^0\pi^-p$	$>10\%$	2749	1530	3
	$K^-p \rightarrow K^-\pi^+n$	$>5\%$	6048	3377	4
Two-prong + vee	$K^-p \rightarrow \bar{K}^0\pi^-p$	$>1\%$	1841	1741	5
	$K^-p \rightarrow \bar{K}^0\pi^-p\pi^0$	$>5\%$	2442	3092	6
	$K^-p \rightarrow \bar{K}^0\pi^+\pi^-n$	$>5\%$	2039	2341	7
Four-prong	$K^-p \rightarrow K^-p\pi^+\pi^-$	$>1\%$	8470	5399	8
	$K^-p \rightarrow K^-p\pi^+\pi^-\pi^0$	$>5\%$	5474	4740	9
Zero-prong + vee	$K^-p \rightarrow \bar{K}^0n$	MM $^2$ cut	223	269	10

<sup>a</sup> Events in the momentum-transfer region  $0.1 \leq -t \leq 2.0$  GeV $^2$ .

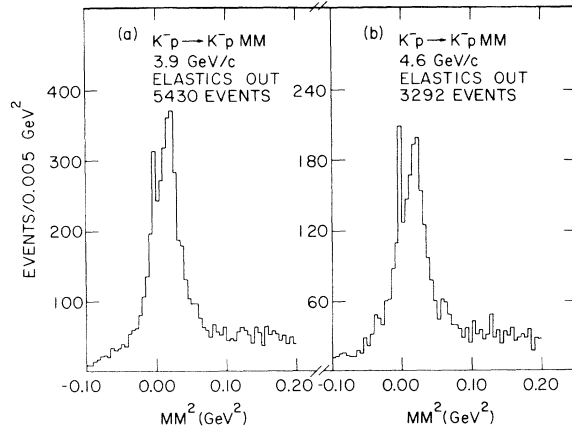


FIG. 1.  $MM^2$  distribution for reaction  $K^-p \rightarrow K^-p$  (MM): (a) at 3.9 GeV/c; (b) at 4.6 GeV/c.

this background on the  $(K\pi)^-$  effective-mass spectrum of reactions 2 and 3 was investigated by examining the effective-mass distribution produced off the recoil proton for events from appropriate side bands to the  $\pi^0$  and  $\bar{K}^0$  missing-mass-squared regions. In addition, after appropriate corrections for probability cuts, visibility factors, and events/ $\mu\text{b}$ , the  $\bar{K}^0\pi^-$  mass spectra of reaction 3 and that of the unambiguous reaction 5 were compared. The results of these studies indicated that a large fraction of the background in both reactions 2 and 3 contributes to the high  $(K\pi)^-$  effective-mass ( $\geq 1.2$  GeV) region. However, after pertinent corrections, the  $K(1420)$ , as well as the  $K^*(890)$  cross section, was found to be in excellent agreement between the two-prong and two-prong-plus-vee topologies, so that studies of these resonances are not in any way biased by this background contamination. (For further details see Sec. V 3.2.)

A large fraction of the background into reaction 4

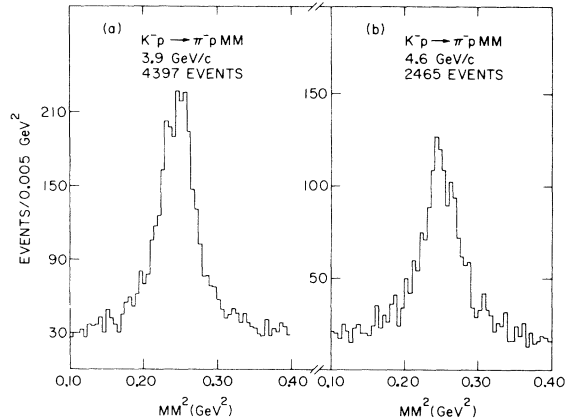


FIG. 2.  $MM^2$  distribution for reaction  $K^-p \rightarrow \pi^-p$  (MM): (a) at 3.9 GeV/c; (b) at 4.6 GeV/c.

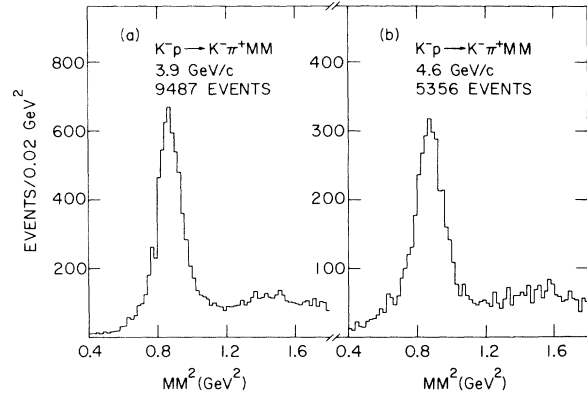


FIG. 3.  $MM^2$  distribution for reaction  $K^-p \rightarrow K^-\pi^+$  (MM): (a) at 3.9 GeV/c; (b) at 4.6 GeV/c.

arose from the inability to distinguish by ionization the identity of the outgoing negative track, which forced contamination from  $\pi^+\pi^-\Lambda^0(\Sigma^0)$  channels. A study of these final states in the two-prong-plus-vee topology revealed that the maximum contamination expected from these reactions was about 10%. We concluded that these channels would not bias results on  $K^*(890)$  [or  $K^0(1420)$ ] production in reaction 4 because the copiously produced  $\rho^0$  ( $f^0$ ) resonances, observed in the  $\pi^+\pi^-$  effective-mass spectrum of these reactions, have relatively small cross sections, and produced broad enhancements centered above (below) the  $K^*(890)$  [ $K^0(1420)$ ] when the outgoing  $\pi^-$  was incorrectly identified as a  $K^-$ .

The  $MM^2$  distribution for the two-prong-plus-vee sample<sup>5</sup> from the final states,

$$K^-p \rightarrow \bar{K}^0\pi^-p \text{ MM},$$

$$K^-p \rightarrow \bar{K}^0\pi^+\pi^- \text{ MM},$$

is shown in Figs. 4 and 5. Small backgrounds with

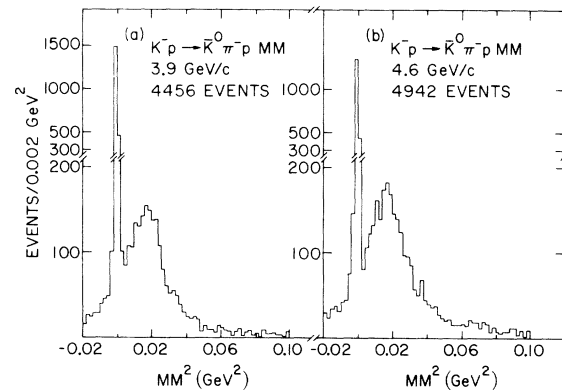


FIG. 4.  $MM^2$  distribution for reaction  $K^-p \rightarrow \bar{K}^0\pi^-p$  (MM): (a) at 3.9 GeV/c; (b) at 4.6 GeV/c.

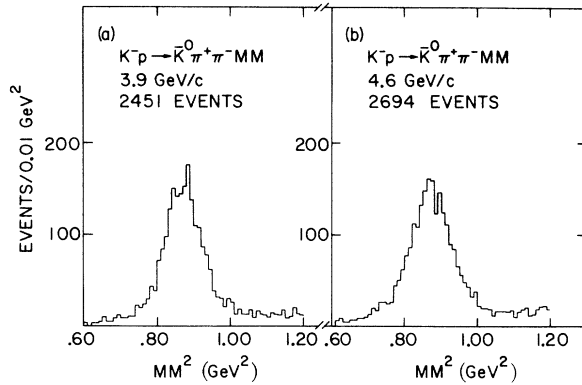


FIG. 5.  $MM^2$  distribution for reaction  $K^-p \rightarrow \bar{K}^0 \pi^+ \pi^- MM$ : (a) at 3.9 GeV/c; (b) at 4.6 GeV/c.

distributions centered at the appropriate mass values are observed. Reactions 6 and 7 were chosen with the  $\chi^2$  indicated in Table II, provided there was no ambiguity with the seven-constraint hypothesis (reaction 5), which was chosen with  $P_{\chi^2} > 1\%$ . The resulting  $\chi^2$ -probability distributions are all consistent with being flat.

The  $MM^2$  distribution from the four-prong sample from the final state

$$K^-p \rightarrow K^- \pi^+ \pi^- p MM$$

is shown in Fig. 6. These distributions include multiple entries from permutations of particles. Again, small backgrounds are observed under the  $\pi^0$  peaks. Note that permutations of four-constraint events distort the  $MM^2$  spectrum by filling the gap between the elastic and  $\pi^0$  peaks. Probability selections are indicated in Table II. Permutation ambiguities were handled by selecting an event into a given hypothesis if its  $\chi^2$  probability was not smaller than one tenth of the maximum  $\chi^2$  probability for any other fit, with the same number of constraints, to the given event.

The missing mass squared for the zero-prong-

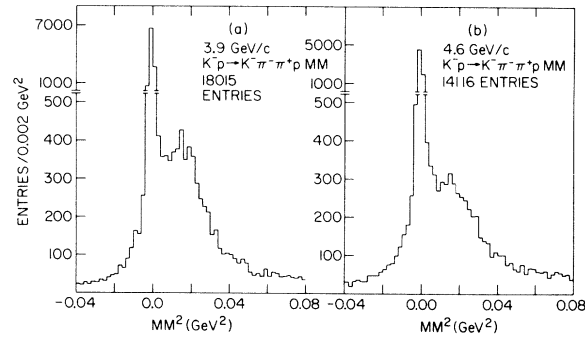


FIG. 6.  $MM^2$  distribution for reaction  $K^-p \rightarrow K^- \pi^+ \pi^- p MM$ : (a) at 3.9 GeV/c; (b) at 4.6 GeV/c.

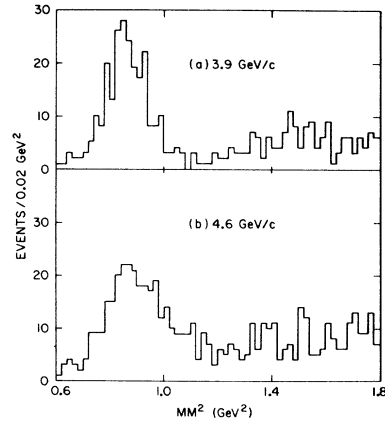


FIG. 7.  $MM^2$  distribution for reaction  $K^-p \rightarrow \bar{K}^0 \pi \pi MM$ : (a) at 3.9 GeV/c; (b) at 4.6 GeV/c.

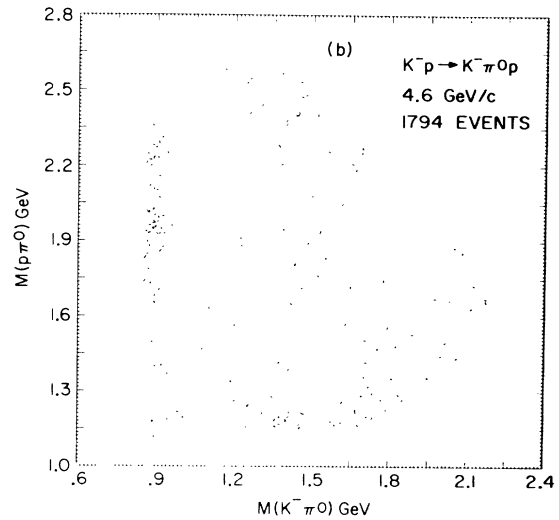
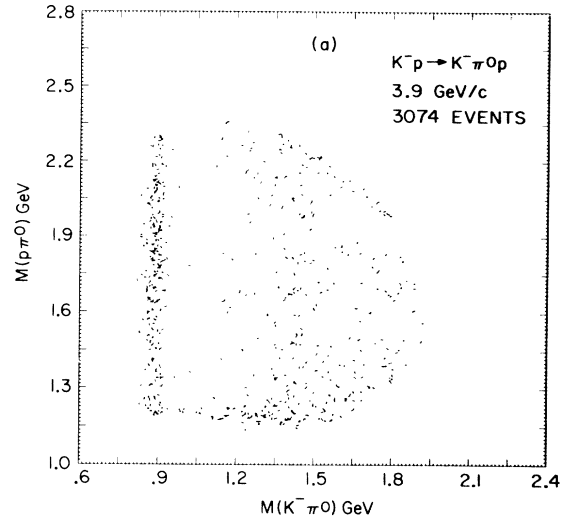


FIG. 8.  $M(K^- \pi^0)$  vs  $M(p \pi^0)$  distribution for reaction  $K^-p \rightarrow K^- \pi^0 p$ : (a) at 3.9 GeV/c; (b) at 4.6 GeV/c.

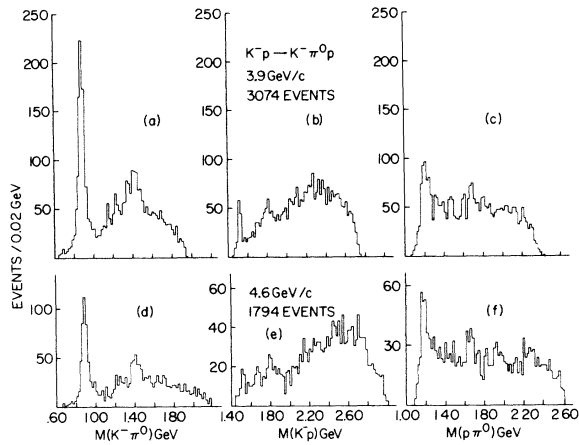


FIG. 9.  $K^-\pi^0$ ,  $K^-p$ , and  $p\pi^0$  effective-mass distributions for reaction  $K^-p \rightarrow K^-\pi^0p$ : (a), (b), and (c) at 3.9 GeV/c; (d), (e), and (f) at 4.6 GeV/c.

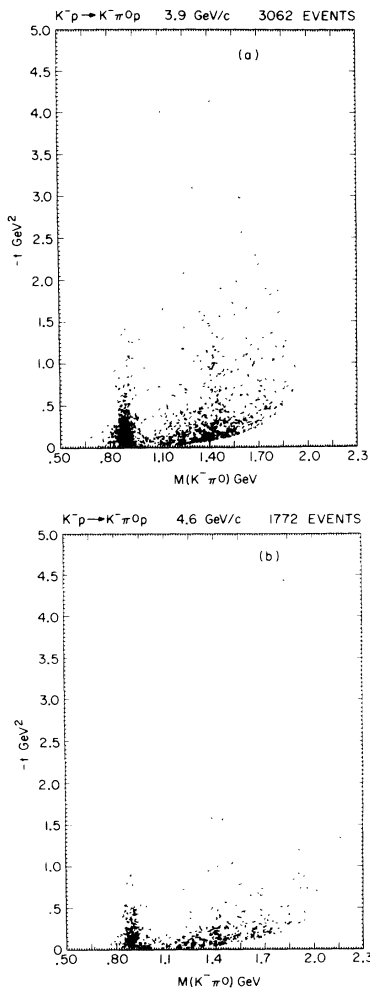


FIG. 10.  $M(K^-\pi^0)$  vs  $-t_{p-p}$  distribution for reaction  $K^-p \rightarrow K^-\pi^0p$ : (a) at 3.9 GeV/c; (b) at 4.6 GeV/c.

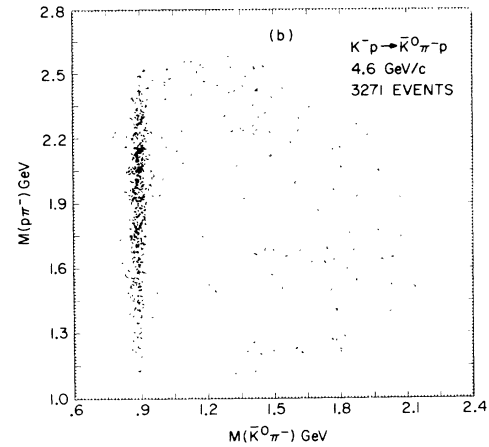
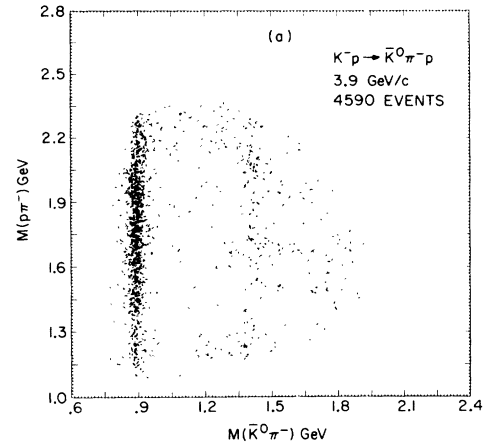


FIG. 11.  $M(\bar{K}^0\pi^-)$  vs  $M(p\pi^-)$  distribution for reaction  $K^-p \rightarrow \bar{K}^0\pi^-p$ : (a) at 3.9 GeV/c; (b) at 4.6 GeV/c.

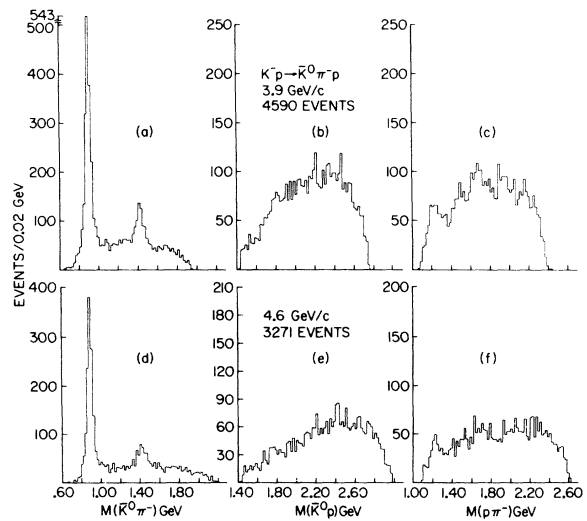


FIG. 12.  $\bar{K}^0\pi^-$ ,  $\bar{K}^0p$ , and  $p\pi^-$  effective-mass distributions for reaction  $K^-p \rightarrow \bar{K}^0\pi^-p$ : (a), (b), and (c) at 3.9 GeV/c; (d), (e), and (f) at 4.6 GeV/c.

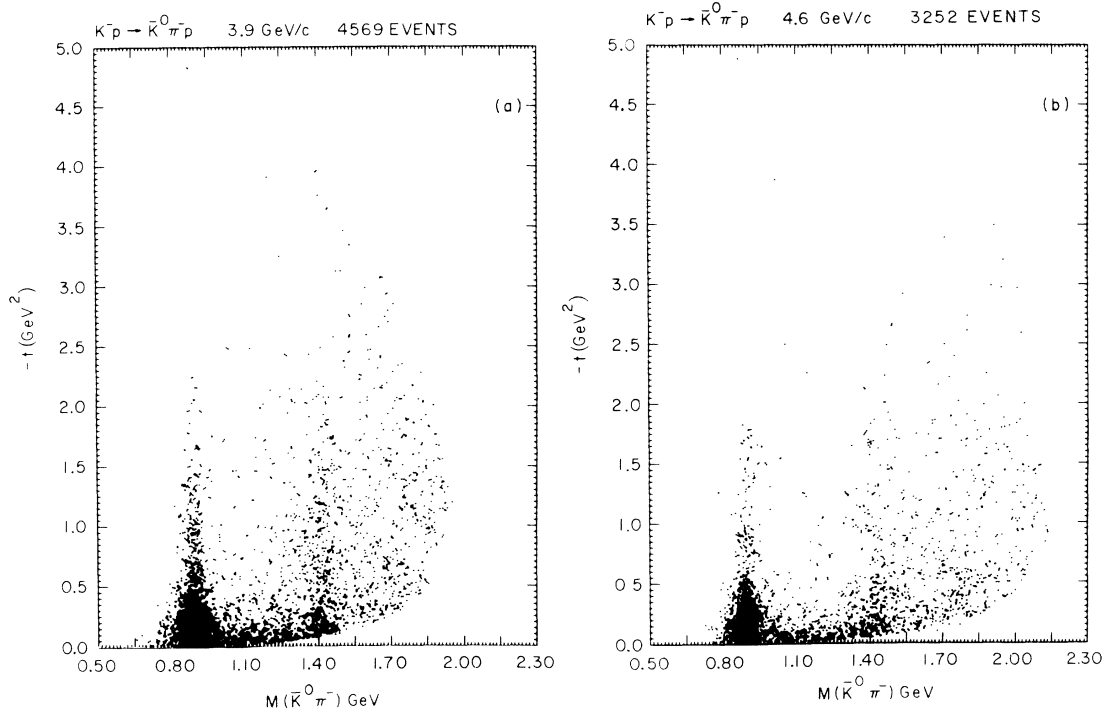
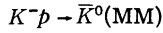


FIG. 13.  $M(\bar{K}^0\pi^-)$  vs  $-t_{p-p}$  distribution for reaction  $K^-p \rightarrow \bar{K}^0\pi^-p$ : (a) at 3.9 GeV/c; (b) at 4.6 GeV/c.

plus-vee sample from the reaction



is shown in Fig. 7. A clear neutron peak is seen which is somewhat broader at 4.6 GeV/c than at the lower momentum. In order to obtain a clean sample of events of reaction 10 ( $K^-p \rightarrow \bar{K}^0n$ ), we have imposed the following selections on the missing mass squared and its error:

$$(a) \quad M_n^2 - 2\Delta(MM^2) \leq MM^2 \leq M_n^2 + 2\Delta(MM^2),$$

$$(b) \quad MM^2 < M_n^2 + \frac{1}{2}[(M_n + M_{\pi^0})^2 - M_n^2],$$

where  $M_n$  ( $M_{\pi^0}$ ) is the mass of the neutron (pion). Selection (b) was imposed so that the probability for reaction 10 ( $\chi^2 \sim (M_n^2 - MM^2)^2 / [\Delta(MM^2)]^2$ ) is larger than the corresponding probability for  $K^-p \rightarrow \bar{K}^0\pi^0n$ .

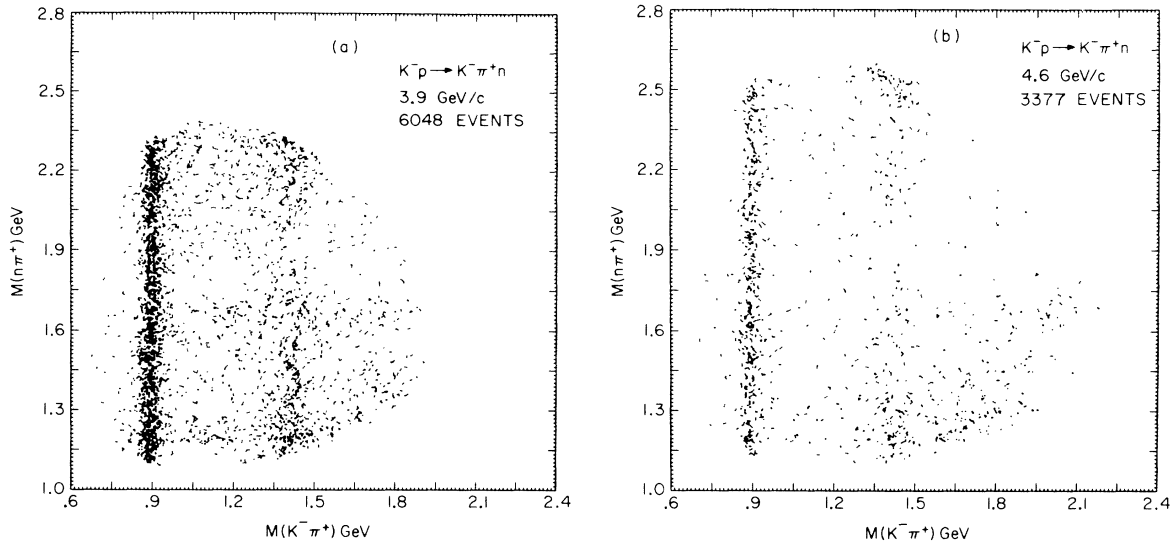


FIG. 14.  $M(K^-\pi^+)$  vs  $M(n\pi^+)$  distribution for reaction  $K^-p \rightarrow K^-\pi^+n$ : (a) at 3.9 GeV/c; (b) at 4.6 GeV/c.

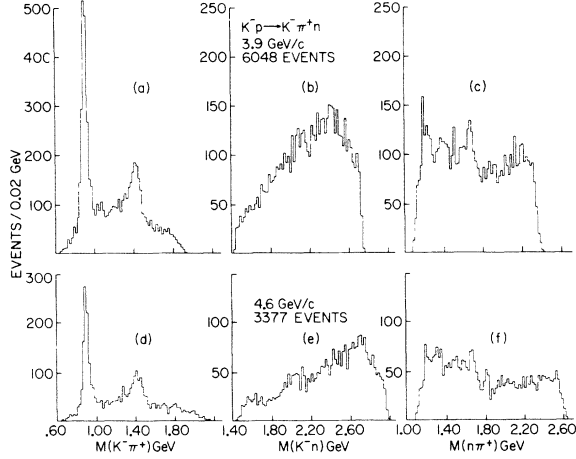


FIG. 15.  $K^-\pi^+$ ,  $K^-n$ , and  $n\pi^+$  effective-mass distributions for reaction  $K^-p \rightarrow K^-\pi^+n$ : (a), (b), and (c) at 3.9 GeV/c; (d), (e), and (f) at 4.6 GeV/c.

## 2. General Description of Final States

The dominant feature of the three-body final states, reactions 2–5, is strong peripheral production of  $K^*(890)$  and  $K^*(1420)$  resonances, as can be seen in the Dalitz plots, mass projections, and Chew-Low plots of Figs. 8–16. Also observed, in their respective invariant-mass plots, are much weaker signals from various  $N^*$  and  $Y^*$  resonances. We note that the production of the neutral  $K\pi$  system (Fig. 16) is more peripheral than its negatively charged partner (Figs. 10 and 13).

As observed in Figs. 17–20, the four-body non-charge-exchange channels (reactions 6 and 8) are dominated by the peripherally produced low-mass

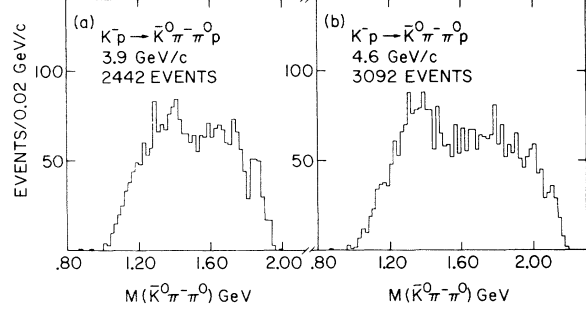


FIG. 17.  $\bar{K}^0\pi^-\pi^0$  effective-mass distribution for reaction  $K^-p \rightarrow \bar{K}^0\pi^-\pi^0p$ : (a) at 3.9 GeV/c; (b) at 4.6 GeV/c.

$K\pi\pi$  enhancement (the  $Q$ ). The absence of this effect and the peripheral production of the  $K(1420)$  (Figs. 21–22) are the relevant features of the neutral  $K\pi\pi$  system of reaction 7.

The five-body final state, reaction 9, was used to obtain  $K(1420)$  branching ratios into  $K^-\eta$  and  $K^-\omega$ . Clear signals for  $\eta$  and  $\omega$  production are observed in the  $\pi^+\pi^-\pi^0$  effective-mass spectra, which are shown in Fig. 23.

## III. ELASTIC AND CHARGE-EXCHANGE REACTIONS

### 1. Elastic Scattering Reaction

In this section we present the experimental data on the elastic scattering reaction

$$K^-p \rightarrow K^-p.$$

We have limited our analysis of reaction 1 to events with momentum transfer  $-t$  larger than 0.1

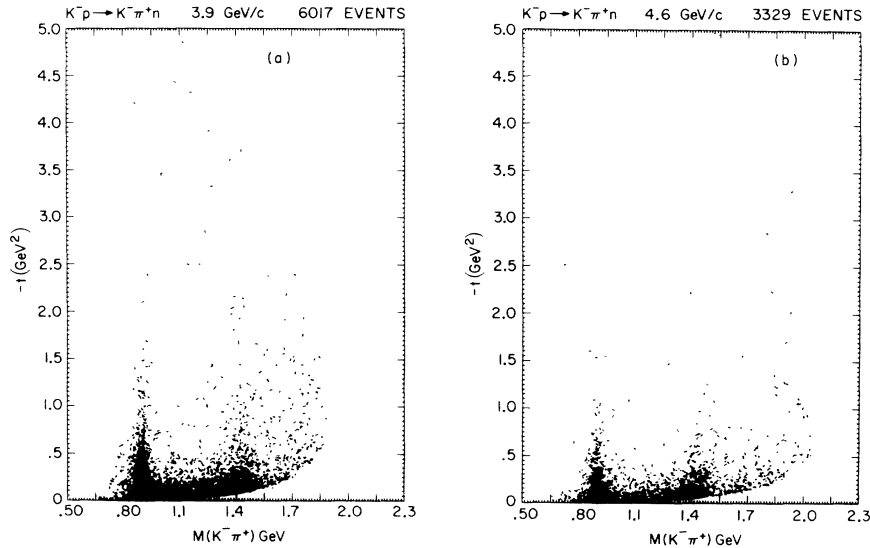


FIG. 16.  $M(K^-\pi^+)$  vs  $-t_{p-n}$  distribution for reaction  $K^-p \rightarrow K^-\pi^+n$ : (a) at 3.9 GeV/c; (b) at 4.6 GeV/c.

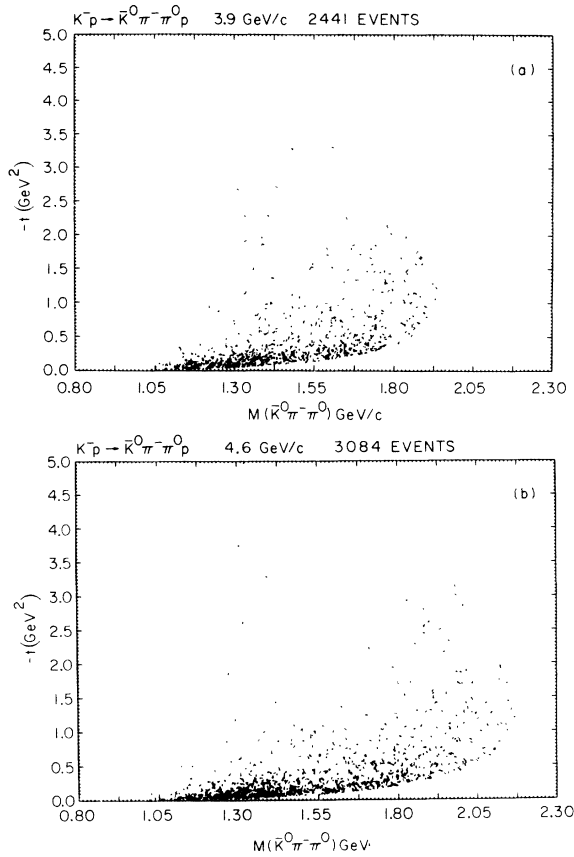


FIG. 18.  $M(\bar{K}^0\pi^-\pi^0)$  vs  $-t_{p-p}$  distribution for reaction  $K^-p \rightarrow \bar{K}^0\pi^-\pi^0p$ : (a) at 3.9 GeV/c; (b) at 4.6 GeV/c.

GeV<sup>2</sup>. This  $-t$  selection corresponds to proton lengths larger than 20 cm, which are clearly visible on the scanning table, so that little or no loss of elastic events is expected either from our aforementioned scanning criterion or from azimuthal biases. In Tables III and IV are given the number of elastic events and the corrected differential

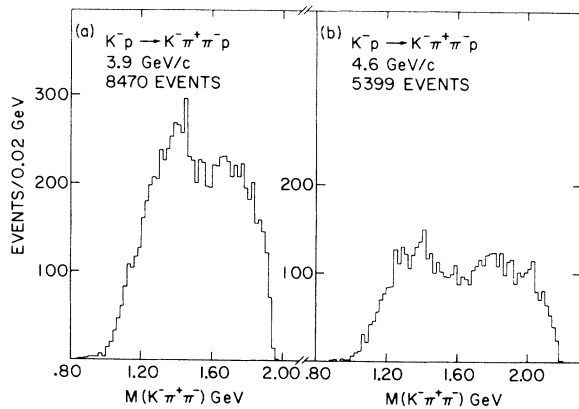


FIG. 19.  $K^-\pi^+\pi^-$  effective-mass distribution for reaction  $K^-p \rightarrow K^-\pi^+\pi^-p$ : (a) at 3.9 GeV/c; (b) at 4.6 GeV/c.

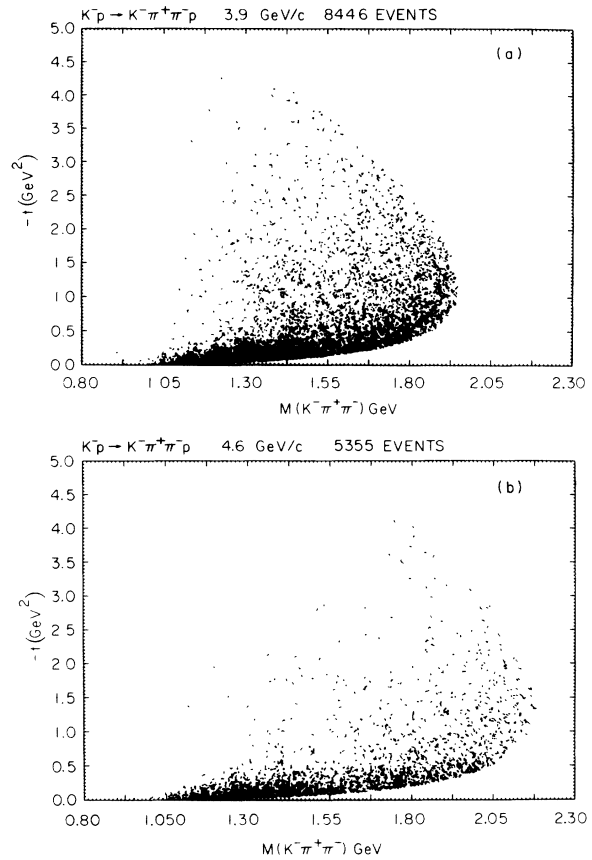


FIG. 20.  $M(K^-\pi^+\pi^-)$  vs  $-t_{p-p}$  distribution for reaction  $K^-p \rightarrow K^-\pi^+\pi^-p$ : (a) at 3.9 GeV/c; (b) at 4.6 GeV/c.

cross section,<sup>4</sup>  $d\sigma/dt$ , as a function of  $-t$ . The number of events in each bin has been corrected for the bias due to the loss of protons with short projected length on the scanning table. As seen in Tables III and IV, the correction in the smallest momentum-transfer bins is small, amounting to  $\leq 7\%$ .

In Figs. 24(a) and 24(b) the elastic scattering differential cross sections at 3.9 and 4.6 GeV/c, respectively, are shown. Both distributions show a

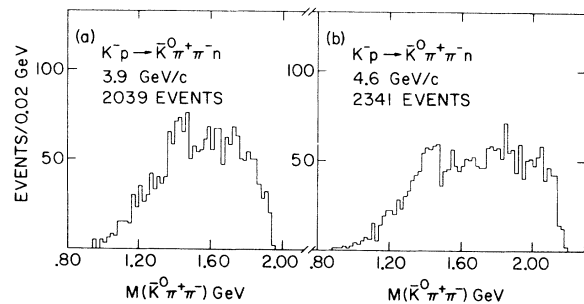


FIG. 21.  $\bar{K}^0\pi^+\pi^-$  effective-mass distribution for reaction  $K^-p \rightarrow \bar{K}^0\pi^+\pi^-n$ : (a) at 3.9 GeV/c; (b) at 4.6 GeV/c.

TABLE III. 3.9-GeV/ $c$  elastic scattering data.

$-t$ range (GeV <sup>2</sup> )	Number of events	Corrected number of events	$d\sigma/dt$ (mb/GeV <sup>2</sup> )
0.10-0.11	622	674 ± 31	15.7 ± 0.72
0.11-0.12	588	613 ± 30	14.3 ± 0.69
0.12-0.13	547	563 ± 28	13.1 ± 0.66
0.13-0.14	511	529 ± 27	12.3 ± 0.63
0.14-0.15	500	504 ± 27	11.7 ± 0.62
0.15-0.16	447	460 ± 26	10.7 ± 0.60
0.16-0.17	424	466 ± 26	10.8 ± 0.60
0.17-0.18	337	361 ± 23	8.41 ± 0.53
0.18-0.19	361	374 ± 23	8.70 ± 0.54
0.19-0.20	361	396 ± 24	9.20 ± 0.55
0.20-0.21	332	347 ± 22	8.10 ± 0.52
0.21-0.22	269	277 ± 20	6.45 ± 0.46
0.22-0.23	274	276 ± 20	6.41 ± 0.46
0.23-0.24	240	250 ± 19	5.81 ± 0.44
0.24-0.25	214	221 ± 18	5.15 ± 0.41
0.25-0.26	220	241 ± 19	5.61 ± 0.43
0.26-0.27	159	173 ± 16	4.02 ± 0.37
0.27-0.28	164	164 ± 13	3.81 ± 0.30
0.28-0.29	169	176 ± 16	4.09 ± 0.37
0.29-0.30	173	173 ± 13	4.02 ± 0.31
0.30-0.31	137	137 ± 12	3.19 ± 0.27
0.31-0.32	147	147 ± 12	3.42 ± 0.28
0.32-0.33	128	139 ± 14	3.22 ± 0.33
0.33-0.34	121	133 ± 14	3.09 ± 0.32
0.34-0.35	80	80 ± 9	1.86 ± 0.21
0.35-0.36	109	121 ± 13	2.82 ± 0.31
0.36-0.37	97	97 ± 10	2.26 ± 0.23
0.37-0.38	90	100 ± 12	2.33 ± 0.28
0.38-0.39	76	80 ± 11	1.86 ± 0.25
0.39-0.40	70	70 ± 9	1.63 ± 0.19
0.40-0.425	157	164 ± 15	1.53 ± 0.14
0.425-0.45	139	139 ± 12	1.29 ± 0.11
0.45-0.475	109	121 ± 13	1.13 ± 0.12
0.475-0.50	102	102 ± 10	0.95 ± 0.09
0.50-0.525	76	77 ± 10	0.72 ± 0.10
0.525-0.55	71	73 ± 10	0.68 ± 0.09
0.55-0.575	57	60 ± 9	0.56 ± 0.09
0.575-0.60	38	43 ± 8	0.40 ± 0.07
0.60-0.625	35	39 ± 7	0.36 ± 0.07
0.625-0.65	26	26 ± 5	0.24 ± 0.05
0.65-0.675	32	34 ± 7	0.32 ± 0.07
0.675-0.70	23	23 ± 5	0.21 ± 0.04
0.70-0.80	75	80 ± 11	0.19 ± 0.02
0.80-0.90	50	54 ± 9	0.13 ± 0.02
0.90-1.00	30	30 ± 6	0.07 ± 0.01
1.00-1.10	44	44 ± 7	0.10 ± 0.01
1.10-1.20	42	47 ± 8	0.11 ± 0.02
1.20-1.30	39	43 ± 8	0.10 ± 0.02
1.30-1.40	28	28 ± 5	0.07 ± 0.01
1.40-1.50	36	36 ± 6	0.08 ± 0.01
1.50-1.60	25	25 ± 5	0.06 ± 0.01
1.60-1.70	32	34 ± 7	0.08 ± 0.02
1.70-1.80	19	20 ± 5	0.05 ± 0.01
1.80-1.90	21	23 ± 6	0.05 ± 0.01
1.90-2.00	19	21 ± 6	0.05 ± 0.01
2.00-2.50	48	48 ± 7	0.022 ± 0.003
2.50-3.00	13	13 ± 4	0.006 ± 0.002
3.00-3.50	7	7 ± 2.6	0.003 ± 0.001
>3.50	3	3 ± 1.7	

TABLE IV. 4.6-GeV/c elastic scattering data.

$-t$ range (GeV <sup>2</sup> )	Number of events	Corrected number of events	$d\sigma/dt$ (mb/GeV <sup>2</sup> )
0.10-0.11	423	440 ± 25	18.3 ± 1.04
0.11-0.12	369	409 ± 24	17.0 ± 1.01
0.12-0.13	331	354 ± 22	14.8 ± 0.94
0.13-0.14	360	391 ± 24	16.3 ± 0.99
0.14-0.15	317	339 ± 22	14.1 ± 0.92
0.15-0.16	279	293 ± 20	12.2 ± 0.85
0.16-0.17	266	279 ± 20	11.6 ± 0.83
0.17-0.18	275	297 ± 21	12.4 ± 0.86
0.18-0.19	243	256 ± 19	10.7 ± 0.80
0.19-0.20	215	215 ± 15	8.96 ± 0.61
0.20-0.21	167	167 ± 13	6.96 ± 0.64
0.21-0.22	199	214 ± 17	8.92 ± 0.73
0.22-0.23	164	174 ± 16	7.26 ± 0.66
0.23-0.24	187	204 ± 17	8.51 ± 0.71
0.24-0.25	139	149 ± 15	6.19 ± 0.61
0.25-0.26	127	130 ± 14	5.42 ± 0.57
0.26-0.27	123	124 ± 13	5.18 ± 0.56
0.27-0.28	127	130 ± 14	5.42 ± 0.57
0.28-0.29	107	107 ± 10	4.46 ± 0.43
0.29-0.30	121	130 ± 14	5.42 ± 0.57
0.30-0.31	105	111 ± 13	4.64 ± 0.53
0.31-0.32	94	101 ± 12	4.23 ± 0.50
0.32-0.33	71	73 ± 10	3.03 ± 0.43
0.33-0.34	60	70 ± 10	2.92 ± 0.42
0.34-0.35	62	66 ± 10	2.74 ± 0.40
0.35-0.36	60	60 ± 8	2.50 ± 0.32
0.36-0.37	60	60 ± 8	2.50 ± 0.32
0.37-0.38	47	49 ± 8	2.02 ± 0.35
0.38-0.39	65	65 ± 8	2.71 ± 0.34
0.39-0.40	56	56 ± 8	2.33 ± 0.31
0.40-0.425	92	100 ± 12	1.67 ± 0.20
0.425-0.45	88	88 ± 9	1.48 ± 0.19
0.45-0.475	70	71 ± 10	1.19 ± 0.17
0.475-0.50	65	69 ± 10	1.14 ± 0.16
0.50-0.525	51	53 ± 9	0.88 ± 0.14
0.525-0.55	63	63 ± 8	1.05 ± 0.13
0.55-0.575	40	41 ± 8	0.69 ± 0.13
0.575-0.60	43	46 ± 8	0.76 ± 0.13
0.60-0.625	37	37 ± 6	0.62 ± 0.10
0.625-0.65	22	26 ± 6	0.43 ± 0.10
0.65-0.675	27	31 ± 7	0.52 ± 0.11
0.675-0.70	21	23 ± 6	0.38 ± 0.10
0.70-0.80	40	41 ± 8	0.17 ± 0.03
0.80-0.90	31	33 ± 7	0.14 ± 0.03
0.90-1.00	31	31 ± 6	0.13 ± 0.02
1.00-1.10	24	29 ± 6	0.12 ± 0.03
1.10-1.20	26	26 ± 5	0.11 ± 0.02
1.20-1.30	17	17 ± 4	0.07 ± 0.02
1.30-1.40	19	19 ± 5	0.08 ± 0.02
1.40-1.50	19	19 ± 5	0.08 ± 0.02
1.50-1.60	14	16 ± 5	0.07 ± 0.02
1.60-1.70	6	6 ± 3	0.03 ± 0.01
1.70-1.80	11	11 ± 3	0.05 ± 0.01
1.80-1.90	3	4 ± 2	0.02 ± 0.01
1.90-2.00	5	7 ± 3	0.03 ± 0.01
2.00-2.50	16	16 ± 4	0.013 ± 0.003
>2.50	5	5 ± 2.2	

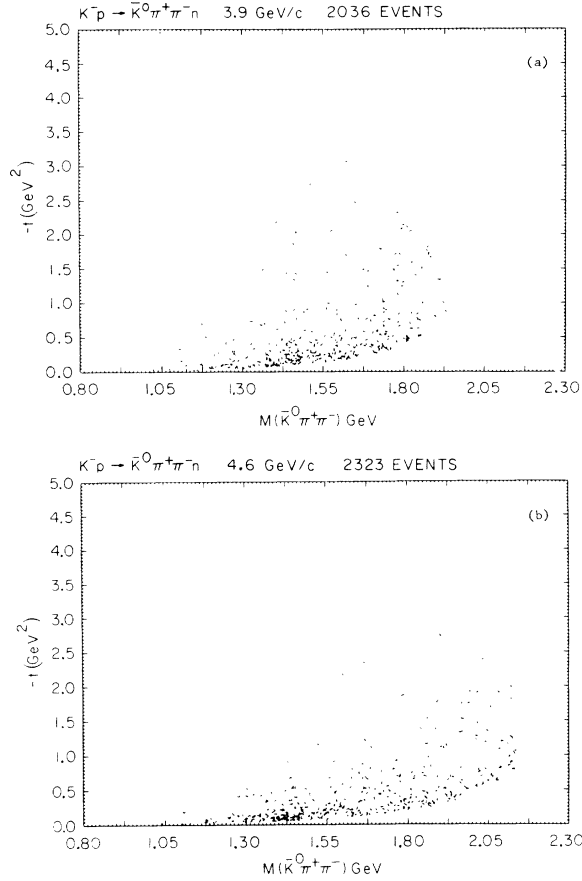


FIG. 22.  $M(\bar{K}^0\pi^+\pi^-)$  vs  $-t_{p-n}$  distribution for reaction  $K^-p \rightarrow \bar{K}^0\pi^+\pi^-n$ : (a) at 3.9 GeV/c; (b) at 4.6 GeV/c.

sharp forward peak for  $0.1 \leq -t \leq 0.8 \text{ GeV}^2$ , with slopes ( $\sim 7.4 \text{ GeV}^{-2}$ ) which are equal within errors. At  $-t \approx 0.8 \text{ GeV}^2$  both distributions exhibit a sharp break and a shallow slope at larger values of  $-t$ . We have parametrized these distributions using the forms  $e^{bt}$  and  $e^{bt+ct^2}$  over different momentum-transfer intervals. Details of the fits are given in Table V.

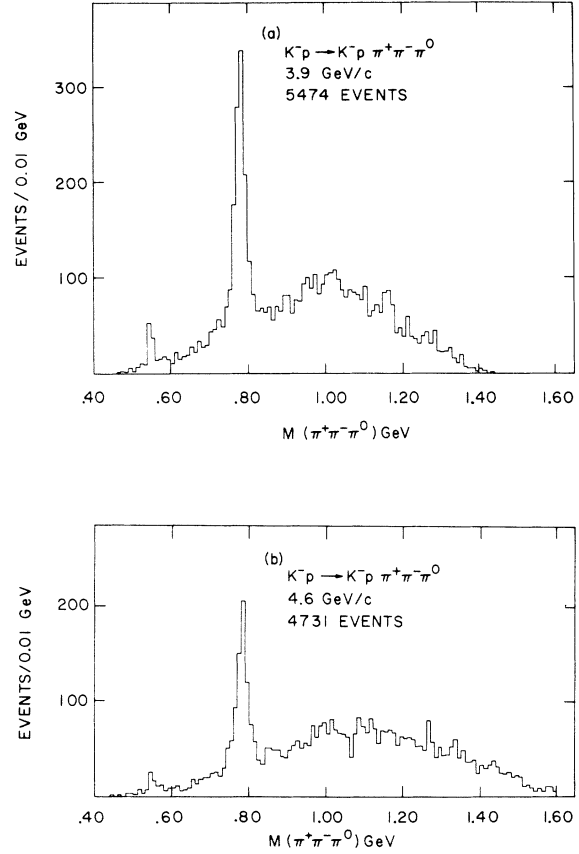


FIG. 23.  $\pi^+\pi^-\pi^0$  effective-mass distribution for reaction  $K^-p \rightarrow K^-p\pi^+\pi^-\pi^0$ : (a) at 3.9 GeV/c; (b) at 4.6 GeV/c.

## 2. Charge-Exchange Reaction

We now turn our discussion to the charge-exchange reaction

$$K^-p \rightarrow \bar{K}^0n,$$

which provides information on the  $I=1$   $t$ -channel exchange in the  $KN \rightarrow KN$  reaction. The differential

TABLE V. Parameters for reaction  $K^-p \rightarrow K^-p$ .

Momentum	$-t$ interval ( $\text{GeV}^2$ )	Corrected number of events	Form fitted	NDF <sup>a</sup>	$\chi^2$	Parameters	
						$b$ ( $\text{GeV}^{-2}$ )	$c$ ( $\text{GeV}^{-4}$ )
3.9 GeV/c	0.1–2.0	9728	$e^{bt+ct^2}$	52	123	$9.41 \pm 0.11$	$3.15 \pm 0.07$
	0.1–0.7	9243	$e^{bt}$	40	46	$7.49 \pm 0.10$	...
	0.8–2.0	405	$e^{bt}$	10	15	$0.66 \pm 0.16$	...
4.6 GeV/c	0.1–2.0	6420	$e^{bt+ct^2}$	52	90	$8.92 \pm 0.15$	$2.72 \pm 0.10$
	0.1–0.7	6161	$e^{bt}$	40	61	$7.27 \pm 0.13$	...
	0.8–2.0	218	$e^{bt}$	10	9	$1.70 \pm 0.22$	...

<sup>a</sup> Number of degrees of freedom.

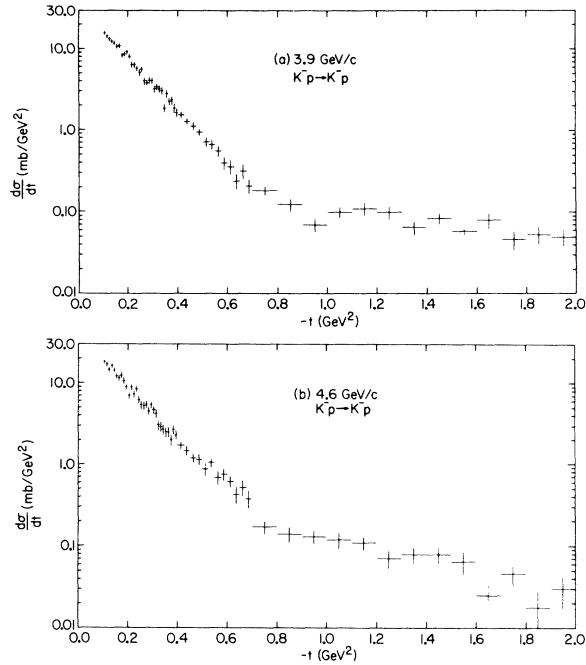


FIG. 24. Differential cross section for reaction  $K^-p \rightarrow K^-n$ : (a) at 3.9 GeV/c; (b) at 4.6 GeV/c.

cross sections, corrected for  $\bar{K}^0$  visibility and losses, for the 3.9- and 4.6-GeV/c samples are displayed in Figs. 25(a) and 25(b) and in Tables VI and VII. The distributions are characterized by a forward peak for  $0.0 \leq -t \leq 0.8$  GeV<sup>2</sup> with a change in slope at  $-t \approx 0.8$  GeV<sup>2</sup> and a significantly smaller slope thereafter. A similar break in slope at approximately the same momentum transfer has been seen for reaction 10 at 3.0 GeV/c<sup>6</sup> and 3.95 GeV/c<sup>7</sup> and for combined data at 5.0, 7.0, 9.5, and 12.0 GeV/c.<sup>8</sup>

Fits similar to the one described for the elastic reaction are presented in Table VIII.

The charge-exchange reaction, 10, has an initial slope approximately half that of the elastic reaction as well as a much smaller cross section, which suggests the dominance of the  $I=0$   $t$ -channel exchange in the  $KN \rightarrow KN$  reaction. Both reactions show breaks in their respective  $-t$  distributions at  $-t \approx 0.8$  GeV<sup>2</sup>. A similar analysis by the SABRE

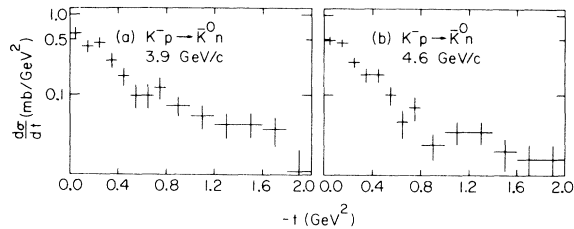


FIG. 25. Differential cross section for reaction  $K^-p \rightarrow \bar{K}^0n$ : (a) at 3.9 GeV/c; (b) at 4.6 GeV/c.

TABLE VI. Differential and total cross sections for reaction  $K^-p \rightarrow \bar{K}^0n$  at 3.9 GeV/c.

$-t$ interval (GeV <sup>2</sup> )	No. of events	Corrected $d\sigma/dt$ ( $\mu\text{b}/\text{GeV}^2$ )
0.00–0.10	48 ± 7	586 ± 84
0.10–0.20	33 ± 6	403 ± 70
0.20–0.30	37 ± 6	452 ± 73
0.30–0.40	22 ± 5	269 ± 57
0.40–0.50	14 ± 4	171 ± 45
0.50–0.60	8 ± 3	98 ± 34
0.60–0.70	8 ± 3	98 ± 34
0.70–0.80	10 ± 3	122 ± 39
0.80–1.0	12 ± 4	73 ± 21
1.0–1.2	9 ± 3	55 ± 18
1.2–1.4	7 ± 3	43 ± 16
1.4–1.6	7 ± 3	43 ± 16
1.6–1.8	6 ± 2	37 ± 15
1.8–2.0	2 ± 1	12 ± 9

$\sigma(K^-p \rightarrow \bar{K}^0n) = 272 \pm 18 \mu\text{b}$

collaboration at 3.0 GeV/c,<sup>6</sup> but which also included  $K^-n$  elastic scattering events, concluded that the break at  $-t \approx 0.8$  GeV<sup>2</sup> was present in both the  $I=0$  and  $I=1$   $t$ -channel exchange contribution to the  $K$ -nucleon differential cross section.

#### IV. PRODUCTION AND DECAY PROPERTIES OF THE $K(890)$

##### 1. $K^{*0}(890) - K^{*+}(890)$ Mass Difference

The  $K^- \pi^+$  effective-mass spectrum for reaction 4 is shown in Fig. 26(a) plotted in 2-MeV bins for the region  $0.8 \leq M(K\pi) \leq 1.0$  GeV. In order to determine the mass and width of the neutral  $K^{*}(890)$ , we have performed a  $\chi^2$  fit on this mass spectrum. We

TABLE VII. Differential and total cross sections for reaction  $K^-p \rightarrow \bar{K}^0n$  at 4.6 GeV/c.

$-t$ interval (GeV <sup>2</sup> )	No. of events	Corrected $d\sigma/dt$ ( $\mu\text{b}/\text{GeV}^2$ )
0.00–0.10	62 ± 8	488 ± 63
0.10–0.20	58 ± 8	457 ± 60
0.20–0.30	33 ± 6	259 ± 45
0.30–0.40	23 ± 5	181 ± 38
0.40–0.50	23 ± 5	181 ± 38
0.50–0.60	13 ± 4	102 ± 28
0.60–0.70	6 ± 2	47 ± 19
0.70–0.80	9 ± 3	71 ± 24
0.80–1.0	6 ± 2	24 ± 9
1.0–1.2	9 ± 3	35 ± 12
1.2–1.4	9 ± 3	35 ± 12
1.4–1.6	5 ± 2	20 ± 9
1.6–1.8	4 ± 2	16 ± 8
1.8–2.0	4 ± 2	16 ± 8
2.0–2.2	2 ± 1	10 ± 4

$\sigma(K^-p \rightarrow \bar{K}^0n) = 212 \pm 13 \mu\text{b}$

TABLE VIII. Parameters for reaction  $K^-p \rightarrow \bar{K}^0 n$ .

Momentum	$-t$ interval (GeV <sup>2</sup> )	Number of events	Form fitted	NDF	$\chi^2$	Parameters	
						$b$ (GeV <sup>-2</sup> )	$c$ (GeV <sup>-4</sup> )
3.9 GeV/c	0.0-2.0	223	$e^{bt+ct^2}$	12	12	$3.1 \pm 0.4$	$0.6 \pm 0.2$
	0.0-0.8	180	$e^{bt}$	6	6	$2.9 \pm 0.4$	...
	0.8-2.0	43	$e^{bt}$	4	2	$1.6 \pm 0.4$	...
4.6 GeV/c	0.0-2.2	269	$e^{bt+ct^2}$	13	13	$4.3 \pm 0.1$	$1.2 \pm 0.10$
	0.0-0.8	227	$e^{bt}$	6	6	$3.3 \pm 0.3$	...
	0.8-2.2	42	$e^{bt}$	5	3	$0.5 \pm 0.4$	...

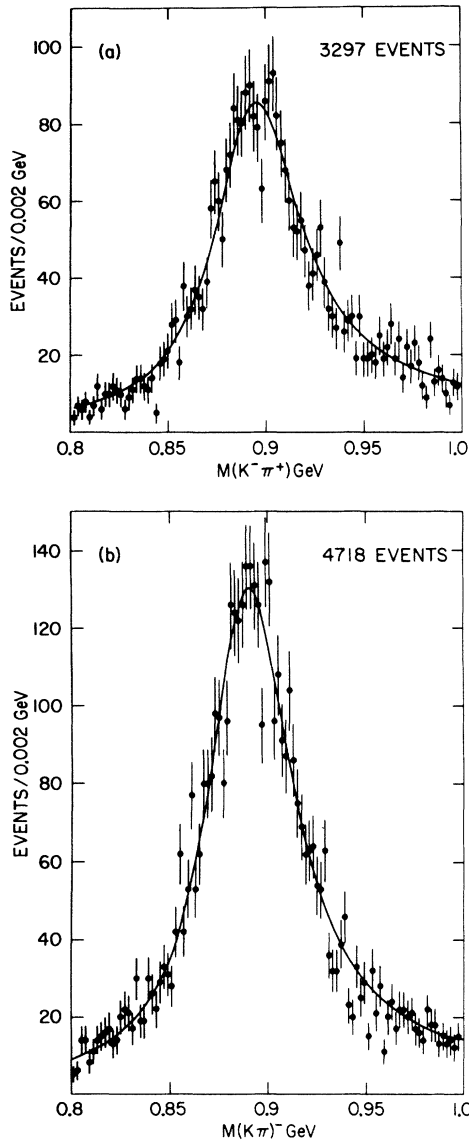


FIG. 26. (a)  $K^- \pi^+$  effective-mass distribution for reaction  $K^- p \rightarrow K^- \pi^+ n$ . The data at 3.9 and 4.6 GeV/c have been combined. (b)  $(K \pi)^-$  effective-mass distribution for reactions  $K^- p \rightarrow K^- \pi^0 p$  and  $K^- p \rightarrow \bar{K}^0 \pi^- p$ . The data at 3.9 and 4.6 GeV/c have been combined.

used a linear form in the mass as background and an energy-dependent Breit-Wigner shape with the form<sup>9</sup>

$$\frac{m}{q} \frac{\Gamma}{(m^2 - m_0^2)^2 + m_0^2 \Gamma^2}, \text{ where } \Gamma = \Gamma_0 \left( \frac{q}{q_0} \right)^{2l+1},$$

multiplying the background. The mass interval was then increased 100 MeV on each side and the fit performed again. The differences in mass and width from the two fits were treated as a systematic error in these quantities and then added to the statistical error. We obtain the following results for  $K^*(890)$ :  $2934 \pm 109$  events;  $M = 897.9 \pm 0.8$  MeV;  $\Gamma = 55.8_{-3.4}^{+4.2}$  MeV. No difference in the values for the mass was detected in the two fits.

Similar fits were then performed on the  $(K \pi)^-$  mass spectrum for reactions 2, 3, and 5 com-

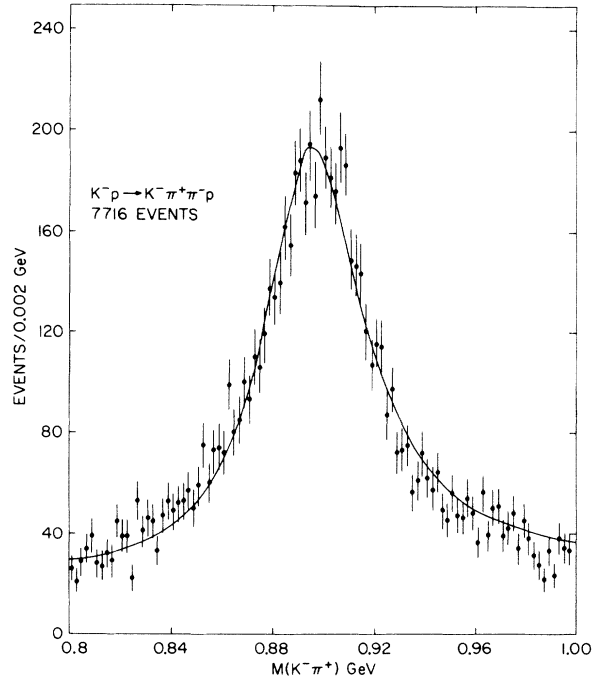


FIG. 27.  $K^- \pi^+$  effective-mass distribution for reaction  $K^- p \rightarrow K^- \pi^+ \pi^- p$ . The data at 3.9 and 4.6 GeV/c have been combined.

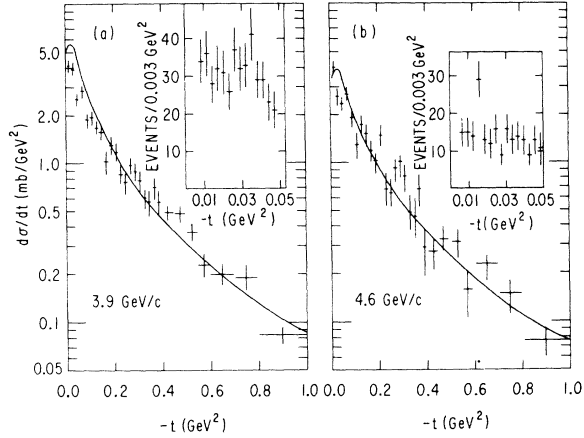


FIG. 28. (a) Differential cross section for reaction  $K^-p \rightarrow K^{*0}(890)n$  at 3.9 GeV/c. The insert shows in detail the distribution in the forward momentum-transfer region. The curve is the result of an OPEA calculation. (b) Same as (a) but at 4.6 GeV/c.

TABLE IX. 3.9 GeV/c:  $K^{*0}(890)$  differential cross section.

$-t$ interval (GeV <sup>2</sup> )	Number of $K^{*0} \rightarrow K^- \pi^+$ events	Corrected $d\sigma/dt$ ( $\mu\text{b}/\text{GeV}^2$ )
0.01-0.02	112 ± 11	4102 ± 403
0.02-0.04	211 ± 15	3864 ± 275
0.04-0.06	138 ± 13	2527 ± 238
0.06-0.08	157 ± 13	2875 ± 238
0.08-0.10	103 ± 10	1886 ± 183
0.10-0.12	106 ± 11	1941 ± 201
0.12-0.14	92 ± 10	1685 ± 183
0.14-0.16	86 ± 9	1575 ± 165
0.16-0.18	56 ± 9	1026 ± 165
0.18-0.20	71 ± 9	1300 ± 165
0.20-0.22	65 ± 8	1190 ± 147
0.22-0.24	47 ± 7	861 ± 128
0.24-0.26	41 ± 7	751 ± 128
0.26-0.28	53 ± 7	971 ± 128
0.28-0.30	49 ± 7	897 ± 128
0.30-0.32	43 ± 7	788 ± 128
0.32-0.34	33 ± 5	604 ± 92
0.34-0.36	31 ± 6	568 ± 110
0.36-0.38	38 ± 6	696 ± 110
0.38-0.40	31 ± 6	568 ± 110
0.40-0.45	67 ± 8	491 ± 59
0.45-0.50	65 ± 8	476 ± 59
0.50-0.55	50 ± 7	366 ± 51
0.55-0.60	32 ± 6	234 ± 44
0.60-0.70	55 ± 8	201 ± 29
0.70-0.80	52 ± 8	190 ± 29
0.80-1.00	46 ± 7	84 ± 13
1.00-1.50	92 ± 10	67 ± 7
1.50-2.00	25 ± 5	18 ± 4

binned,<sup>10</sup> shown in Fig. 26(b), yielding the following values for  $K^{*0}(890)$ :  $4404 \pm 100$  events;  $M = 892.2 \pm 1.5$  MeV;  $\Gamma = 54.3^{+2.6}_{-2.3}$  MeV, where 0.7 MeV of the error on the mass is systematic.

An additional fit was performed on the  $K^- \pi^+$  effective-mass spectrum of reaction 8, which is shown in Fig. 27. The results of this fit give the following values for  $K^{*0}(890)$ :  $5362 \pm 154$  events;  $M = 898.0 \pm 0.5$  MeV;  $\Gamma = 48.5 \pm 2.2$  MeV. These values for mass and width are clearly consistent with the values obtained in reaction 4. Using only the three-body final states, we obtain a difference between the masses of the neutral and charged  $K^*(890)$  of

$$M(K^{*0}) - M(K^{*-}) = 5.7 \pm 1.7 \text{ MeV.}$$

We note that the Breit-Wigner form given above yields a resonance mass value,  $M$ , approximately 3 MeV higher than the nominal position of the peak of the observed mass distribution. Since, in general, different assumed resonant shapes will give somewhat different mass and width values, caution

TABLE X. 4.6 GeV/c:  $K^{*0}(890)$  differential cross section.

$-t$ interval (GeV <sup>2</sup> )	Number of $K^{*0} \rightarrow K^- \pi^+$ events	Corrected $d\sigma/dt$ ( $\mu\text{b}/\text{GeV}^2$ )
0.005-0.02	91 ± 10	3981 ± 438
0.02-0.04	81 ± 9	2658 ± 295
0.04-0.06	72 ± 8	2363 ± 263
0.06-0.08	83 ± 10	2723 ± 328
0.08-0.10	59 ± 8	1936 ± 263
0.10-0.12	40 ± 7	1313 ± 230
0.12-0.14	53 ± 8	1739 ± 263
0.14-0.16	46 ± 7	1509 ± 230
0.16-0.18	37 ± 6	1214 ± 197
0.18-0.20	32 ± 6	1050 ± 197
0.20-0.22	47 ± 7	1542 ± 230
0.22-0.24	21 ± 5	689 ± 164
0.24-0.26	20 ± 4	656 ± 131
0.26-0.28	28 ± 5	919 ± 164
0.28-0.30	31 ± 6	1017 ± 197
0.30-0.32	25 ± 5	820 ± 164
0.32-0.34	15 ± 4	492 ± 131
0.34-0.36	14 ± 4	459 ± 131
0.36-0.38	21 ± 5	689 ± 164
0.38-0.40	9 ± 3	295 ± 98
0.40-0.45	21 ± 5	276 ± 66
0.45-0.50	25 ± 5	328 ± 66
0.50-0.55	24 ± 5	315 ± 66
0.55-0.60	12 ± 4	158 ± 53
0.60-0.70	34 ± 6	223 ± 39
0.70-0.80	23 ± 5	151 ± 33
0.80-1.00	23 ± 5	75 ± 16
1.00-1.50	36 ± 6	47 ± 8
1.50-2.00	12 ± 4	16 ± 5

TABLE XI.  $K^{*0}(890)$  production angular distribution fits.

Momentum	Form fitted		$e^{bt}$				$e^{bt+ct^2}$			
	$-t$ interval (GeV <sup>2</sup> )	Number of resonance events	$\chi^2$	NDF	$b$ (GeV <sup>-2</sup> )	$\chi^2$	NDF	$b$ (GeV <sup>-2</sup> )	$c$ (GeV <sup>-4</sup> )	
3.9 GeV/c	0.02–1.00	1818	59.7	26	$4.2 \pm 0.2$	42	25	$5.7 \pm 0.1$	$1.9 \pm 0.1$	
4.6 GeV/c	0.02–1.00	896	46.6	26	$4.5 \pm 0.2$	35	25	$6.0 \pm 0.5$	$2.2 \pm 0.6$	

must be used when comparing such numbers from different experiments. As an example, we have performed a fit to the above distributions utilizing an energy-independent Breit-Wigner resonant form, and obtained

$$M(K^{*0}) = 896.4 \pm 0.7 \text{ MeV},$$

and

$$M(K^{*-}) = 889.6 \pm 0.7 \text{ MeV},$$

yielding a mass difference of  $6.8 \pm 1.0$  MeV. It is clear that a variety of possible resonant forms can systematically change the absolute resonant mass value without significantly affecting the mass difference. The value of  $5.7 \pm 1.7$  MeV obtained here conclusively shows that the  $K^{*0}(890)$  is heavier than the  $K^{*-}(890)$ , a feature similar to that observed for the ground state  $K(495)$ .

## 2. Analysis of the Reaction $K^-p \rightarrow K^{*0}(890)n$

We have previously presented<sup>1</sup> an investigation of  $K^{*0}(890)$  production in reaction 4,

$$K^-p \rightarrow K^- \pi^+ n.$$

This analysis tested the one-pion exchange model with absorption (OPEA) and presented new data on resonance production in the very forward region of momentum transfer. The aim of the present section is to give more details on  $K^{*0}(890)$  production in reaction 4 while only briefly discussing the aspects of our previous publication.

The numbers of  $K(890)$  events and the cross sections for  $K^{*0}(890)$  production, after correcting for unseen decay modes and probability cuts, are, respectively,

$$3.9 \text{ GeV}/c: 2061 \pm 80 \text{ events}, \quad \sigma = 755 \pm 30 \mu\text{b},$$

$$4.6 \text{ GeV}/c: 905 \pm 54 \text{ events}, \quad \sigma = 590 \pm 35 \mu\text{b}.$$

Figures 28(a) and 28(b) and Tables IX and X show the  $K^{*0}(890)$  momentum-transfer distribution between target proton and outgoing neutron. The differential cross sections were obtained by fitting each individual  $K^- \pi^+$  effective-mass spectrum with the matrix element described previously, with mass and width fixed at the values given above. The distributions are characterized by sharp for-

ward slopes which round off in the very forward region of momentum transfer,<sup>11</sup>  $-t < 0.04$  GeV<sup>2</sup>, at both momenta [see inserts in Figs. 28(a) and 28(b)]. The predictions of the simple one-pion exchange model with absorption are represented by the solid curves in Figs. 28(a) and 28(b). An excellent description of the differential cross sections is observed. We have fitted the distributions over the intervals and with the forms given in Table XI, in which are given the parameters obtained from these fits, as well as the corresponding  $\chi^2$  and number of degrees of freedom.

As can be seen in Fig. 26(a), the background under the  $K^{*0}(890)$  is very small. The  $\chi^2$  fits to the mass spectra at 3.9 and 4.6 GeV/c indicated that the background is  $\leq 7\%$ . While the absolute magnitude of the background is small, the effects of the interference of the background with the  $K^{*0}(890)$  are not. This can be seen by examining the forward-backward asymmetry  $\alpha = (F - B)/(F + B)$  of the Jackson  $\cos\theta$  distribution<sup>12</sup> in the  $K^- \pi^+$  rest frame as a function of  $K^- \pi^+$  effective mass and  $-t$  as shown in Figs. 29(a)–29(c). In these figures, and

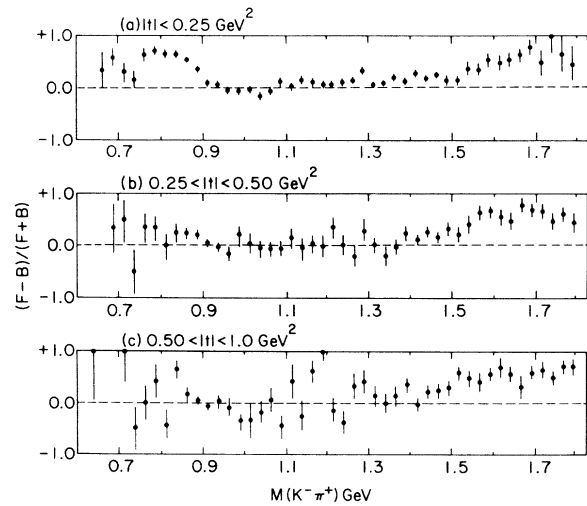


FIG. 29. (a) Forward-backward asymmetry as a function of the  $K^- \pi^+$  effective mass in the momentum-transfer region  $|t| < 0.25$  GeV<sup>2</sup>. The data at 3.9 and 4.6 GeV/c have been combined. (b) Same as (a) but for  $0.25 \leq |t| \leq 0.50$  GeV<sup>2</sup>. (c) Same as (a) but for  $0.50 \leq |t| \leq 1.00$  GeV<sup>2</sup>.

for the remainder of this section, the data at 3.9 and 4.6 GeV/c have been combined, since no statistically significant differences pertinent to the following discussion were found. In the low-momentum-transfer region,  $|t| \leq 0.25 \text{ GeV}^2$ , where the  $K^{*0}(890)$  signal is very strong (see Chew-Low plots, Fig. 16 in Sec. II), there is a rapid variation of  $\alpha$  across the resonance-mass band. One sees that the low side of the  $K^{*0}(890)$  interval [ $M(K^-\pi^+) < 0.9 \text{ GeV}$ ] shows a large positive asymmetry, while in the high side [ $M(K^-\pi^+) > 0.9 \text{ GeV}$ ] the asymmetry is small, going to zero at about  $M(K^-\pi^+) = 0.95 \text{ GeV}$ . For  $|t| > 0.25 \text{ GeV}^2$  [Figs. 29(b) and 29(c)] there remains some residual but small variation of  $\alpha$  across the resonance. Moments analysis across the  $K^{*0}(890)$  region showed only  $l=1$  and  $l=2$  waves to be significant, so that the observed asymmetry is understood in terms of an  $S$ -wave background interfering with the  $P$ -wave resonance. We note that this effect cannot be interpreted as due to a  $\Delta^+(1238)$ - $K^{*0}(890)$  interference since the  $\pi^+n$  effective-mass spectrum shows negligible resonant  $\Delta^+(1238)$  signal when the  $K^-\pi^+$  mass is required to be in the  $K^{*0}(890)$  region (see also Dalitz plots, Fig. 14 in Sec. II).

Having commented on the nature of the nonresonant  $K\pi$  background, we now proceed to investigate its effect on the  $K^{*0}(890)$  in more detail. To do so we first define the following regions:

$$K^{*0}(890): 0.84 \leq M(K^-\pi^+) \leq 0.94 \text{ GeV},$$

$$\text{Low: } 0.84 \leq M(K^-\pi^+) \leq 0.90 \text{ GeV},$$

$$\text{High: } 0.90 \leq M(K^-\pi^+) \leq 0.94 \text{ GeV}.$$

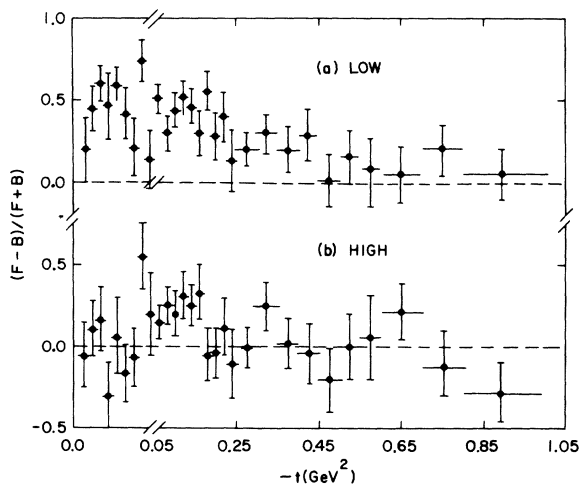


FIG. 30. (a) Forward-backward asymmetry as a function of momentum transfer for the  $K^{*0}(890)$  Low [ $0.84 \leq M(K^-\pi^+) \leq 0.90 \text{ GeV}$ ]. The data at 3.9 and 4.6 GeV/c have been combined. (b) Same as (a) but for the  $K^{*0}(890)$  High [ $0.90 \leq M(K^-\pi^+) \leq 0.94 \text{ GeV}$ ].

In Figs. 30(a) and 30(b) we show  $\alpha$  as a function of momentum transfer for the low and high sides of the  $K^{*0}(890)$  region. In the low side,  $\alpha$  grows as the momentum transfer gets small; it is very large for  $|t| \leq 0.25 \text{ GeV}^2$  and tends to round off in the very forward direction. In the high side,  $\alpha$  is consistent with zero for  $|t| < 0.05 \text{ GeV}^2$ , grows to  $\sim 0.2$  between 0.05 and 0.20  $\text{GeV}^2$ , then is again consistent with zero for  $|t| \geq 0.20 \text{ GeV}^2$ . From this apparent structure in the interference it would appear unlikely that any meaningful result on the  $S$ -wave  $K\pi$  phase shifts in the  $K^{*0}(890)$  region, which are extracted from extrapolation of  $\alpha$  to the pion pole, could be obtained. The large value of the  $S$ - $P$ -wave interference at small  $-t$  does, however, imply a large pseudoscalar- (presumably pion-) exchange contribution in the  $K^{*0}(890)$  region because a  $0^-(\pi)$  exchange is the only possible coupling to the  $0^-(K^-)0^+$  ( $S$ -wave) vertex. Additional information of the production characteristics of the  $0^+$  background under the  $K^{*0}(890)$  can be obtained if we make the assumption that the background under the resonance is due to the  $S$ -wave  $K^-\pi^+$  system. It is difficult to test this assumption strictly because of the small background present; however, we have found that the reflections of  $\Delta^+$  and  $Y^*$  resonances give a negligible contribution to the background, and as will be discussed below, we have found excellent fits to the  $K^-\pi^+$  decay angular distributions assuming only  $S$

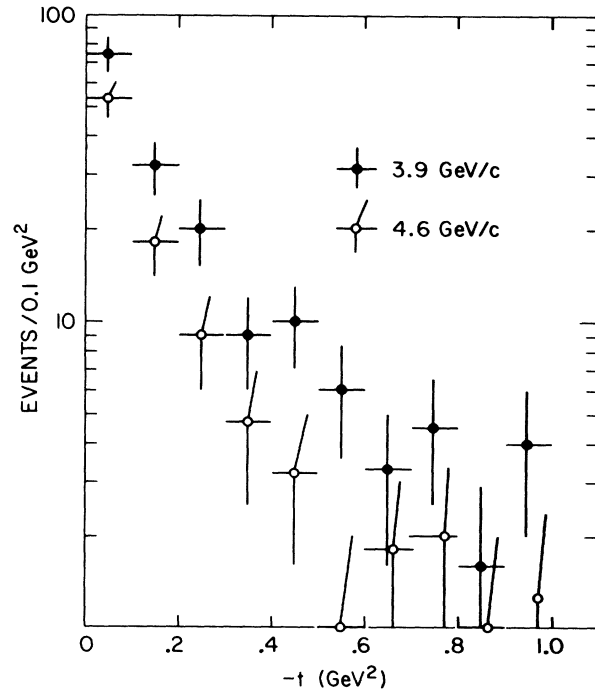


FIG. 31. Distribution of background events [in the region  $0.84 \leq M(K^-\pi^+) \leq 0.94 \text{ GeV}$ ] as a function of momentum transfer for the 3.9- and 4.6-GeV/c samples.

and  $P$  waves to be present. For each momentum separately, we show in Fig. 31 the distribution of the number of background events in the  $K^{*0}(890)$  region as a function of momentum transfer. As a measure of the peripherality of this  $K^-\pi^+$  system we have fitted each distribution to a form  $\sim e^{At}$  for  $|t| < 0.4 \text{ GeV}^2$  and obtained

$$3.9 \text{ GeV}/c = A = 7.0 \pm 1.0 \text{ GeV}^{-2},$$

$$4.6 \text{ GeV}/c = A = 9.0 \pm 1.5 \text{ GeV}^{-2},$$

$$W(\cos\theta, \phi) = \frac{1}{4\pi} + \frac{3}{4\pi} [(\rho_{00} - \rho_{11})(\cos^2\theta - \frac{1}{3}) - \sqrt{2} \text{Re}\rho_{10} \sin 2\theta \cos\phi - \rho_{1-1} \sin^2\theta \cos 2\phi] \\ + \frac{\sqrt{3}}{4\pi} [-2\sqrt{2} \text{Re}\rho_{10}^{\text{int}} \sin\theta \cos\phi + 2 \text{Re}\rho_{00}^{\text{int}} \cos\theta].$$

To test whether this parametrization can, in fact, be used to extract the resonance density-matrix elements ( $\rho_{00}$ ,  $\rho_{11}$ ,  $\rho_{1-1}$ , and  $\text{Re}\rho_{10}$ ), we have performed a maximum-likelihood fit to both the low and high sides of the  $K^{*0}(890)$  as a function of momentum transfer, and we have extracted the  $\rho_{ij}$ 's

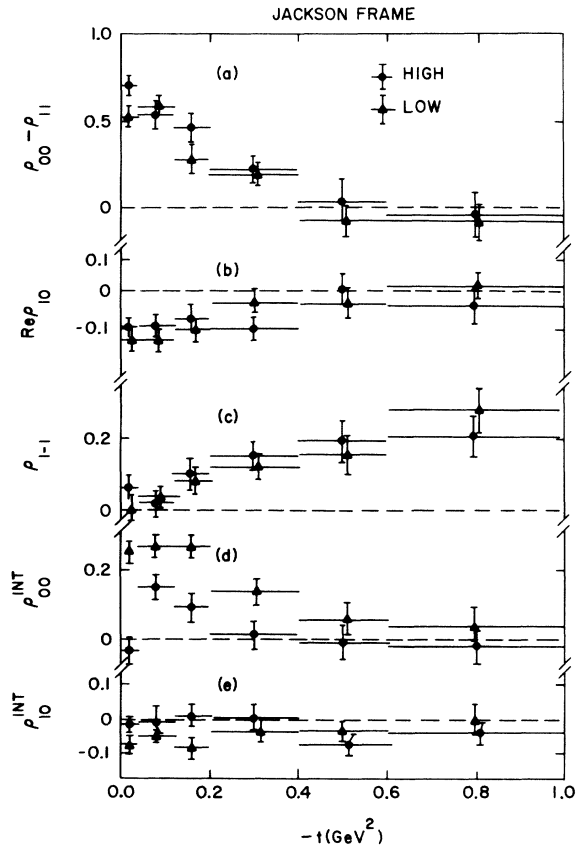


FIG. 32. Density-matrix elements in the Gottfried-Jackson frame as a function of momentum transfer for the  $K^{*0}(890)$  Low (black triangles) and High (black dots). The data at 3.9 and 4.6 GeV/c have been combined.

which shows that the  $S$ -wave production distribution is more peripheral at each momentum than the corresponding  $K^{*0}(890)$  distribution.

Thus, in order to extract the density-matrix elements of the  $K^{*0}(890)$  we must include in the form of the  $1^-$  decay angular distribution the contribution of the  $S$ -wave background. The decay angular distribution (applicable in both the helicity and Jackson frames) for a  $K^-\pi^+$  system with interfering  $S$ - $P$  waves is then written<sup>13</sup>

in the Jackson frame. The values of the  $\rho_{ij}$ 's so obtained are shown in Figs. 32(a)–32(e) with the dots (triangles) corresponding to the high (low) side. Within statistics, the values of  $\rho_{00} - \rho_{11}$ ,  $\text{Re}\rho_{10}$ , and  $\rho_{1-1}$  for each region are equal in each bin of momentum transfer, as they must be if they describe the resonance  $K^{*0}(890)$  spin populations. However, the  $\text{Re}\rho_{00}^{\text{int}}$  and  $\text{Re}\rho_{10}^{\text{int}}$  [Figs. 32(d)–32(e)] which describe the  $S$ - $P$ -wave interference are very different for the two regions, indicative of the difference in the amount of the asymmetry shown above.

Assured that the above expression of the angular distribution adequately represented a good para-

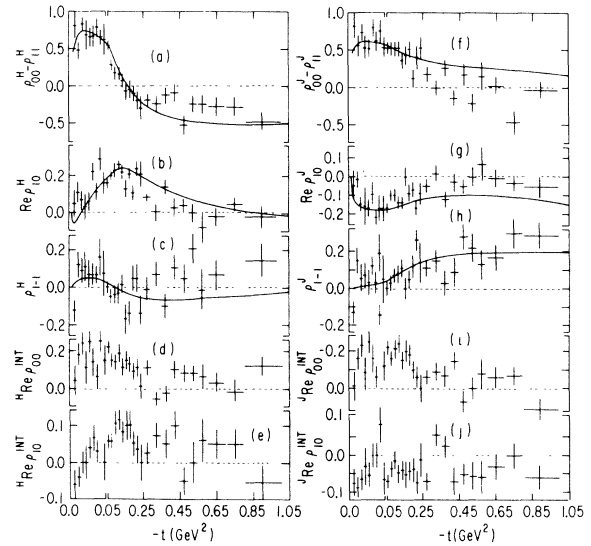


FIG. 33. (a)–(e) Density-matrix elements of the  $K^{*0}(890)$  in the helicity frame as a function of momentum transfer. The curves are the result of an OPEA calculation. The data at 3.9 and 4.6 GeV/c have been combined. (f)–(j) Same as (a)–(e) but the density-matrix elements are evaluated in the Gottfried-Jackson frame.

TABLE XII.  $K^{*0}(890)$  density matrices.

$-t$ interval (GeV <sup>2</sup> )	No. of events	Jackson frame					Helicity frame				
		$\rho_{00} - \rho_{11}$	$\text{Re}\rho_{10}$	$\rho_{1-1}$	$\text{Re}\rho_{10}^{\text{int}}$	$\text{Re}\rho_{00}^{\text{int}}$	$\rho_{00} - \rho_{11}$	$\text{Re}\rho_{10}$	$\rho_{1-1}$	$\text{Re}\rho_{10}^{\text{int}}$	$\text{Re}\rho_{00}^{\text{int}}$
0.005-0.01	46	0.83±0.17	-0.05±0.09	-0.13±0.06	-0.08±0.04	0.01±0.08	0.82±0.18	0.05±0.08	-0.13±0.06	-0.06±0.05	0.04±0.08
0.01-0.015	69	0.56±0.14	-0.01±0.05	0.15±0.07	-0.09±0.03	0.16±0.06	0.48±0.12	0.11±0.06	0.12±0.07	-0.04±0.03	0.18±0.07
0.015-0.02	68	0.74±0.11	-0.15±0.04	0.06±0.08	-0.07±0.03	0.23±0.06	0.83±0.10	0.07±0.05	0.09±0.07	0.00±0.03	0.24±0.06
0.02-0.025	42	0.54±0.16	-0.16±0.10	0.07±0.08	-0.03±0.05	0.09±0.10	0.69±0.22	0.03±0.07	0.11±0.08	0.01±0.05	0.11±0.10
0.025-0.03	66	0.53±0.12	-0.17±0.05	0.03±0.07	-0.05±0.03	0.25±0.06	0.66±0.13	0.06±0.05	0.07±0.08	0.04±0.03	0.25±0.06
0.03-0.035	62	0.80±0.12	-0.10±0.06	0.12±0.05	0.00±0.03	0.16±0.08	0.67±0.15	0.22±0.05	0.07±0.06	0.07±0.04	0.13±0.08
0.035-0.04	63	0.63±0.14	-0.22±0.04	0.03±0.06	0.00±0.04	0.06±0.06	0.78±0.13	0.11±0.05	0.07±0.05	0.03±0.03	0.06±0.07
0.04-0.045	49	0.76±0.17	-0.17±0.07	0.19±0.10	0.08±0.05	0.40±0.06	0.67±0.10	0.29±0.07	0.16±0.10	0.23±0.08	0.26±0.06
0.045-0.05	43	0.54±0.14	-0.17±0.07	0.05±0.13	-0.06±0.04	0.12±0.08	0.63±0.20	0.16±0.07	0.08±0.13	0.01±0.05	0.15±0.08
0.05-0.07	185	0.53±0.08	-0.17±0.03	0.01±0.04	-0.07±0.02	0.22±0.04	0.56±0.07	0.16±0.03	0.00±0.03	0.06±0.02	0.23±0.04
0.07-0.09	153	0.53±0.09	-0.10±0.03	0.03±0.04	-0.04±0.02	0.16±0.04	0.29±0.08	0.20±0.03	-0.05±0.04	0.06±0.03	0.15±0.04
0.09-0.11	116	0.53±0.09	-0.10±0.04	0.07±0.04	-0.01±0.03	0.22±0.05	0.18±0.09	0.23±0.04	-0.04±0.05	0.11±0.03	0.14±0.04
0.11-0.13	104	0.53±0.10	-0.14±0.04	0.08±0.05	-0.05±0.03	0.24±0.05	0.17±0.09	0.26±0.03	-0.04±0.06	0.12±0.03	0.19±0.05
0.13-0.15	118	0.37±0.10	-0.14±0.04	0.11±0.05	-0.04±0.03	0.15±0.05	0.08±0.09	0.22±0.04	0.02±0.05	0.08±0.03	0.12±0.04
0.15-0.17	76	0.44±0.13	0.00±0.05	0.00±0.06	-0.05±0.04	0.20±0.06	-0.07±0.11	0.13±0.05	-0.17±0.08	0.10±0.04	0.16±0.05
0.17-0.19	82	0.52±0.11	-0.09±0.05	0.05±0.06	-0.04±0.03	0.18±0.06	-0.05±0.12	0.21±0.03	-0.14±0.07	0.10±0.04	0.13±0.05
0.19-0.21	91	0.13±0.12	-0.07±0.04	0.12±0.06	-0.04±0.03	0.10±0.05	-0.09±0.11	0.11±0.04	0.05±0.07	0.05±0.04	0.09±0.05
0.21-0.23	71	0.41±0.16	-0.17±0.04	0.26±0.06	-0.07±0.03	0.06±0.06	-0.20±0.12	0.24±0.04	0.05±0.08	0.04±0.04	0.11±0.05
0.23-0.25	50	0.54±0.15	-0.09±0.06	0.14±0.11	-0.01±0.05	0.00±0.08	-0.29±0.16	0.21±0.07	-0.14±0.10	0.00±0.05	0.01±0.07
0.25-0.30	152	0.19±0.10	-0.05±0.04	0.11±0.05	-0.07±0.03	0.06±0.04	-0.19±0.08	0.08±0.04	-0.01±0.06	0.03±0.03	0.11±0.04
0.30-0.35	111	0.01±0.11	0.02±0.04	0.15±0.06	0.06±0.03	0.09±0.05	-0.23±0.09	0.00±0.05	0.07±0.07	0.07±0.03	-0.06±0.04
0.35-0.40	92	0.27±0.12	-0.12±0.05	0.03±0.07	0.02±0.03	0.07±0.06	-0.13±0.11	0.14±0.04	-0.10±0.07	0.06±0.04	-0.03±0.05
0.40-0.45	71	-0.12±0.11	-0.03±0.05	0.09±0.08	-0.07±0.04	0.15±0.05	-0.05±0.13	0.03±0.05	0.11±0.07	0.10±0.04	0.10±0.06
0.45-0.50	71	0.19±0.15	-0.05±0.04	0.28±0.07	-0.05±0.03	0.07±0.06	-0.52±0.13	0.04±0.04	0.05±0.08	-0.05±0.04	0.08±0.05
0.50-0.55	60	-0.21±0.14	0.01±0.05	0.22±0.08	-0.06±0.04	-0.01±0.06	-0.23±0.12	0.00±0.05	0.21±0.08	0.00±0.04	0.08±0.05
0.55-0.60	41	0.17±0.09	0.07±0.09	0.13±0.08	-0.06±0.05	0.08±0.08	-0.24±0.12	-0.08±0.09	-0.01±0.11	0.06±0.06	0.06±0.07
0.60-0.70	70	0.04±0.13	0.00±0.05	0.17±0.07	-0.03±0.04	0.06±0.06	-0.26±0.13	-0.02±0.05	0.07±0.09	0.05±0.04	0.04±0.05
0.70-0.80	60	-0.45±0.16	-0.03±0.04	0.30±0.08	0.00±0.04	0.07±0.05	-0.26±0.13	0.05±0.04	0.36±0.09	0.05±0.04	-0.02±0.05
0.80-1.00	60	-0.03±0.14	-0.05±0.06	0.29±0.07	-0.06±0.03	-0.11±0.06	-0.46±0.12	-0.02±0.06	0.15±0.09	-0.06±0.05	0.12±0.05

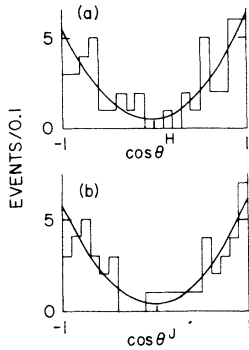


FIG. 34. (a)  $\cos\theta$  distribution in the helicity frame for the  $K^*(890)$  in the momentum-transfer region  $0.005 \leq -t \leq 0.01 \text{ GeV}^2$ . (b) Same as (a) but in the Gottfried-Jackson frame.

metrization of the  $K^*(890)$ , since the resonance  $\rho_{ij}$ 's agreed between the low and high sides and excellent representations of the experimental angular distributions were obtained, we proceeded to extract the  $K^*(890)$  density-matrix elements. The  $\rho_{ij}$ 's were obtained in both the Jackson frame ( $\rho_{ij}^J$ ) and the helicity frame ( $\rho_{ij}^H$ ) in the  $K^*(890)$  region by performing a maximum-likelihood fit on the events in fine bins of momentum transfer, using the interfering  $S$ - $P$ -wave's angular distribution. The  $\rho_{ij}$ 's so obtained are given in Figs. 33(a)–33(j) and in Table XII. The quoted resonance density-matrix elements do not include a small renormalization effect (averaging  $\sim 7\%$ ) due to the presence of the  $K\pi$   $S$ -wave background (i.e., the average value of  $\rho_{00} + 2\rho_{11} = 0.93$ ).

The following observations can be made.

(1) In the region  $-t < 0.04 \text{ GeV}^2$  there is no significant change in either frame in the value for  $\rho_{00} - \rho_{11}$ . This rules against any strong variation of  $\rho_{00}$  or  $\rho_{11}$  down to our kinematic threshold. The

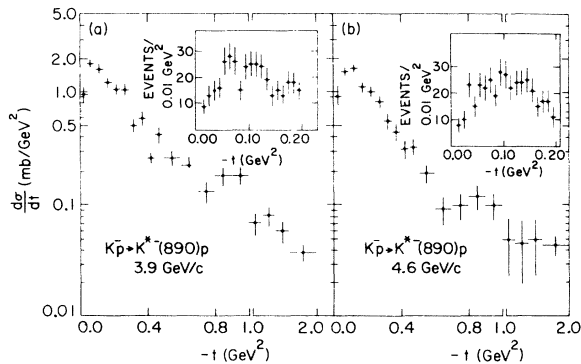


FIG. 35. (a) Differential cross section for reaction  $K^-p \rightarrow K^{*-}(890)p$  (from reaction 5) at  $3.9 \text{ GeV}/c$ . The insert shows the distribution in the forward momentum-transfer region in more detail. (b) Same as (a) but at  $4.6 \text{ GeV}/c$ .

large value of  $\rho_{00} - \rho_{11}$  suggests a large  $\pi$ -exchange contribution which is expected to dominate in this momentum-transfer region because of the nearness of the pion pole. As an aid in making it absolutely clear that  $\rho_{11}$  has not begun to rise significantly in the forward direction (which is a prediction of some models<sup>14</sup>), leading to a  $\sin^2\theta$  decay angular distribution, we show in Fig. 34 the  $\cos\theta$  distribution in the Jackson and helicity frames in our smallest bin of momentum transfer,  $0.005 \leq -t \leq 0.01 \text{ GeV}^2$  (i.e.,  $\frac{1}{4}m_\pi^2 \leq -t \leq \frac{1}{2}m_\pi^2$ ). As indicated by the value of  $\rho_{00} - \rho_{11}$ , we observe a strong  $\cos^2\theta$  angular distribution in both frames with no semblance of a  $\sin^2\theta$  component. In addition, note that, as suggested by the small asymmetry observed in the forward direction, the  $S$ -wave cross section which is proportional to the isotropic term in the Jackson angular distribution is extremely small in the forward momentum-transfer region.

(2)  $\text{Re}\rho_{10}$  exhibits strong structure in both frames.  $\rho_{1,-1}^J$  is small in the forward direction and rises to  $\sim 0.2$  for  $-t > 0.25 \text{ GeV}^2$ .

(3) The solid curves in the figure represent the predictions of the OPEA model, which give a good description of the  $\rho_{ij}$  distributions for  $-t \leq 0.3 \text{ GeV}^2$  and were described in a previous publication.<sup>1</sup>

In summary,  $K^*(890)$  production is characterized by a sharply rising production distribution which becomes flat for  $-t < 0.04 \text{ GeV}^2$ . The  $0^+$  background underneath the  $P$ -wave resonance interferes strongly, producing an asymmetry which varies rapidly across the resonance region. The large value of  $\rho_{00} - \rho_{11}$ , the production of the  $S$  wave, and the sharp rise of  $d\sigma/dt$  all suggest the dominance of  $\pi$  exchange in the forward direction of momentum transfer in the resonance region.

### 3. Analysis of the Reaction $K^-p \rightarrow K^{*-}(890)p$

The final states of interest for this study are reactions 2, 3, and 5. The Dalitz plots, Chew-Low plots, and corresponding mass projections for these reactions have already been exhibited in Sec. II. As mentioned above, a bias against very short proton tracks exists in reactions 2 and 3 so that differential cross-section information in the low  $-t$  region ( $-t \leq 0.1 \text{ GeV}^2$ ) was provided by reaction 5.

The total cross sections for  $K^{*-}(890)$  production, obtained from the fits to the  $\bar{K}^0\pi^-$  mass spectrum of reaction 5, are

$$3.9 \text{ GeV}/c: \sigma = 575 \pm 19 \mu\text{b},$$

$$4.6 \text{ GeV}/c: \sigma = 509 \pm 23 \mu\text{b}.$$

The cross sections quoted have been corrected for probability cuts,  $\bar{K}^0$  visibility, and losses, as well as for unseen resonance decay modes.

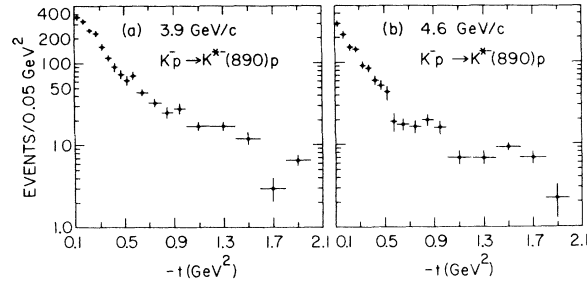


FIG. 36. (a) Production distribution for reaction  $K^-p \rightarrow K^{*-}(890)p$  at 3.9 GeV/c for the combined sample from reactions 2, 3, and 5. (b) Same as (a) but at 4.6 GeV/c.

The momentum-transfer distributions, obtained by fitting the  $K\pi$  effective-mass distributions in each interval of  $-t$ , are shown in Fig. 35(a) [reaction 5; 3.9 GeV/c], Fig. 35(b) [reaction 5; 4.6 GeV/c], Fig. 36(a) [reactions 2, 3, 5; 3.9 GeV/c], and Fig. 36(b) [reactions 2, 3, 5; 4.6 GeV/c]. The differential cross sections obtained by normalizing the distributions of Figs. 35(a) and 35(b) to the total  $K^{*-}(890)$  cross sections quoted above are given in Table XIII [for  $-t < 0.1$  GeV<sup>2</sup> only reaction 5 was used.] The combined data at both momenta and for all three final states consist of a sample of  $\sim 4400$   $K^{*-}(890)$  events. The following are the main features of the resonance production distributions.

(a) A rounding off and a subsequent dip in the forward direction for  $-t < 0.10$  GeV<sup>2</sup> [for fine details

TABLE XIII.  $K^{*-}(890)$  differential cross section.

$-t$ interval (GeV <sup>2</sup> )	3.9 GeV/c Corrected $d\sigma/dt$ ( $\mu\text{b}/\text{GeV}^2$ )	4.6 GeV/c Corrected $d\sigma/dt$ ( $\mu\text{b}/\text{GeV}^2$ )
0.00–0.05	953 ± 144	901 ± 127
0.05–0.10	1771 ± 166	1509 ± 142
0.10–0.15	1482 ± 97	1578 ± 112
0.15–0.20	1316 ± 93	1162 ± 117
0.20–0.25	1009 ± 65	805 ± 80
0.25–0.30	932 ± 61	768 ± 64
0.30–0.35	627 ± 53	490 ± 53
0.35–0.40	474 ± 45	458 ± 48
0.40–0.45	324 ± 37	325 ± 43
0.45–0.50	292 ± 34	282 ± 37
0.50–0.55	251 ± 32	240 ± 37
0.55–0.60	288 ± 32	101 ± 27
0.60–0.70	178 ± 18	93 ± 16
0.70–0.80	132 ± 16	88 ± 16
0.80–0.90	99 ± 14	107 ± 17
0.90–1.0	111 ± 16	85 ± 16
1.0–1.2	69 ± 8	37 ± 7
1.2–1.4	69 ± 8	36 ± 7
1.4–1.6	47 ± 8	49 ± 8
1.6–1.8	13 ± 4	36 ± 7
1.8–2.0	26 ± 5	12 ± 4

TABLE XIV.  $K^{*-}(890)$  production angular distribution fits.

Momentum	Form fitted $-t$ interval (GeV <sup>2</sup> )	Number of resonance events	$e^{b*}$		
			$\chi^2$	NDF	$b$ (GeV <sup>-2</sup> )
3.9 GeV/c	0.1–0.8	1890	18	10	4.2 ± 0.2
	0.8–1.6	288	4	3	1.1 ± 0.3
4.6 GeV/c	0.1–0.8 <sup>a</sup>	1233	13	10	5.1 ± 0.2

<sup>a</sup> No reasonable  $\chi^2$  probability was obtained in the large  $-t$  region.

see inserts<sup>15</sup> in Figs. 35(a) and 35(b)].

(b) A sharp slope for  $0.1 \leq -t \leq 0.8$  GeV<sup>2</sup> (see Table XIV for fitted forms and parameters).

(c) A change in slope at  $-t \approx 0.8$  GeV<sup>2</sup>, which occurs at about the same location as that observed in the elastic and charge-exchange  $K$ -nucleon reactions, which were previously discussed.

The forward dip and the relatively large cross sections in the region  $-t \geq 0.8$  GeV<sup>2</sup> for the  $K^{*-}(890)$  are in contradistinction to the corresponding  $K^{*0}(890)$  distribution. This implies that the dominant exchange mechanism responsible for the production of  $K^{*-}(890)$  is not the same as that for the neutral  $K^{*}(890)$  (i.e.,  $I=1$  exchange). Additionally, the  $K^{*-}(890)$  total cross section is three to four times larger than would be expected from charge independence, which for an  $I=1$  exchange predicts  $\sigma(K^{*-}(890))/\sigma(K^{*0}(890)) = \frac{1}{4}$ .

We now proceed to examine the asymmetry of the Jackson angle in the  $(K\pi)^-$  rest frame; such an investigation was essential to our understanding of the  $K^{*0}(890)$  region. Figure 37 shows  $\alpha$  as a function of the  $(K\pi)^-$  effective mass and momentum transfer for reactions 3 and 5 (black dots) and reaction 2 (open dots). As before, the data at 3.9 and 4.6 GeV/c have been combined. For  $|t| < 0.25$  GeV<sup>2</sup>, both reactions exhibit a variation in asymmetry across the  $K^{*-}(890)$  region; however, the maximum value of  $\alpha$  is about a factor of three less than that in the  $K^{*0}(890)$  channel for the corresponding momentum-transfer interval. The asymmetry in the  $K^0\pi^-$  system (black dots) crosses from positive to negative through the  $K^*$  region, and then remains large and negative in the region between the  $K^{*}(890)$  and  $K(1420)$ . The asymmetry in the  $K^-\pi^0$  system shows a different behavior above the  $K^{*}(890)$  region, becoming large and positive; however, an investigation of the  $p\pi^0$  effective-mass spectrum for  $K\pi$  events in this region shows a  $\Delta^+(1238)$  enhancement which, when removed and repopulated with the appropriate background events, reduces the large positive asymmetry. Even after  $\Delta^+$  removal, how-

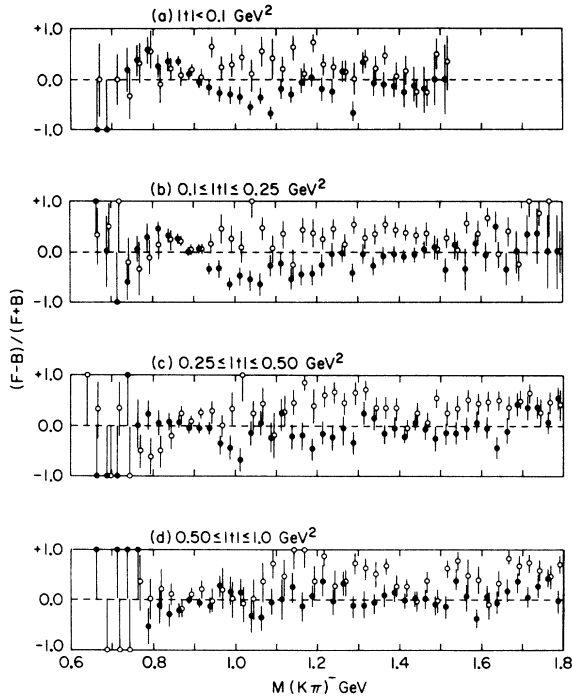


FIG. 37. (a) Forward-backward asymmetry as a function of the  $(K\pi)^-$  effective mass in the momentum-transfer region  $|t| < 0.1 \text{ GeV}^2$ , for reaction 2 (open dots) and reactions 3 and 5 combined (black dots). The data at 3.9 and 4.6 GeV/c have been combined. (b) Same as (a) but for  $0.1 \leq |t| \leq 0.25 \text{ GeV}^2$ . (c) Same as (a) but for  $0.25 \leq |t| \leq 0.50 \text{ GeV}^2$ . (d) Same as (a) but for  $0.50 \leq |t| \leq 1.00 \text{ GeV}^2$ .

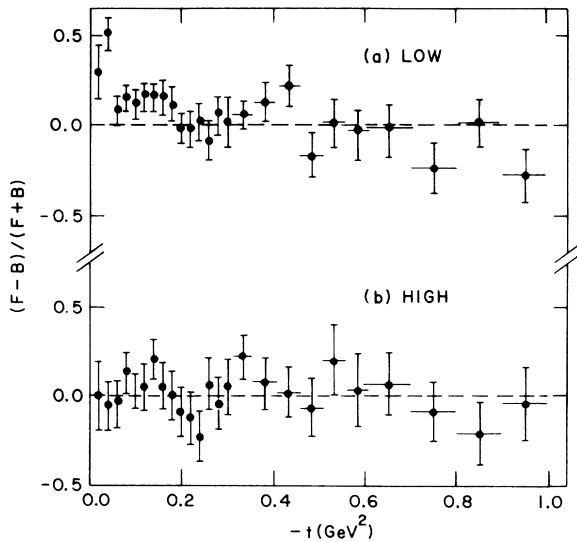


FIG. 38. (a) Forward-backward asymmetry as a function of momentum transfer for the  $K^{*-}(890)$  Low [ $0.84 \leq M(K\pi)^- \leq 0.90 \text{ GeV}$ ]. The data at 3.9 and 4.6 GeV/c have been combined. (b) Same as (a) but for the  $K^{*-}(890)$  High [ $0.90 \leq M(K\pi)^- \leq 0.94 \text{ GeV}$ ].

ever,  $\alpha(K^-\pi^0)$  remains positive and significantly different from  $\alpha(\bar{K}^0\pi^-)$  in the region between the two  $K^*$  resonances.

We now proceed to investigate, in more detail, the structure of the asymmetry parameter in the low and high sides of the  $K^{*-}(890)$ . The distribution of  $\alpha$  as a function of  $-t$  for both regions is shown in Fig. 38 for reactions 2, 3, and 5 combined. We note that  $\alpha$  is consistent with zero in the high side. In the low side,  $\alpha$  is large and  $\sim 6$  standard deviations from zero for  $|t| < 0.05 \text{ GeV}^2$ , small and positive for  $0.05 \leq -t \leq 0.2 \text{ GeV}^2$ , and zero for  $-t > 0.2 \text{ GeV}^2$ . The distributions for reactions 2, 3, and 5, when examined separately, are within the statistical errors consistent with the total sample. To be sure that the observed rise in  $\alpha$  is a property of the  $K\pi$  system and is not caused by reflections of  $N\pi$  or  $KN$  resonances, we have examined the latter two mass spectra (not shown) for both the low and high sides of the  $K^{*-}(890)$  with no evidence found for production of  $N^*$  or  $Y^*$  enhancements. In fact, as can be seen in Figs. 39(a)–39(c), in which the  $(K\pi)^-$  effective-mass spectra for the first three regions of momentum transfer of Fig. 38 are shown, the background level in the  $K^{*-}(890)$  region is very small; the result of the fits indicated that the background is  $\sim 10\%$  of the total number of events in the resonance-mass band for all three regions of momentum transfer. We conclude that the observed rise of the asymmetry, as in the production of  $K^{*0}(890)$ , is a relevant feature of the  $(K\pi)^-$  system and is not caused by an increase or change in the

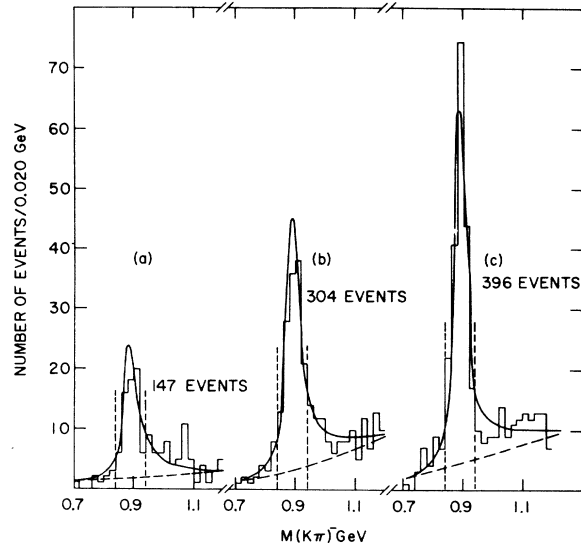


FIG. 39. (a)  $(K\pi)^-$  effective-mass distribution in the momentum-transfer region  $0.01 \leq |t| \leq 0.03 \text{ GeV}^2$ . The data at 3.9 and 4.6 GeV/c have been combined. (b) Same as (a) but for  $0.03 \leq |t| \leq 0.05 \text{ GeV}^2$ . (c) Same as (a) but for  $0.05 \leq |t| \leq 0.07 \text{ GeV}^2$ .

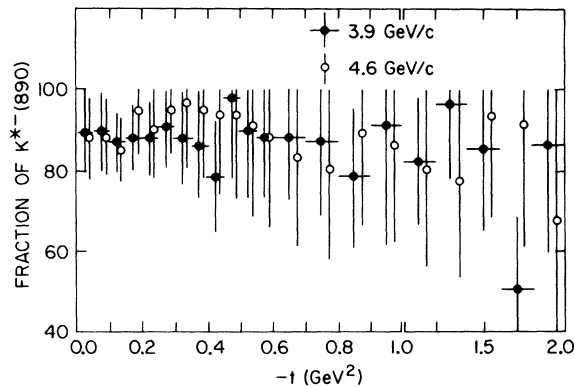


FIG. 40. Distribution of the fraction of  $K^{*-}(890)$  events [in the region  $0.84 \leq M(K\pi)^- \leq 0.94$  GeV] as a function of the momentum transfer.

structure of the non- $(K\pi)$  background. In summary:

(a) The structure of the asymmetry for the high and low sides at low momentum transfer is similar for  $K^{*-}(890)$  and  $K^{*0}(890)$  production.

(b) The strength and the range of momentum transfer of the asymmetry are larger in the  $K^{*0}(890)$  than in the  $K^{*-}(890)$  reaction.

We now proceed to discuss the significance of the  $K^{*-}(890)$  density-matrix elements. The decay angular distribution in the Jackson (or helicity) frame for a  $1^-$  particle decaying into two  $0^-$  particles is written

$$W(\cos\theta, \phi) = \frac{3}{4\pi} [\rho_{00} \cos^2\theta + \rho_{11} \sin^2\theta - \rho_{1-1} \sin^2\theta \cos 2\phi - \sqrt{2} \operatorname{Re}\rho_{10} \sin 2\theta \cos\phi].$$

The  $\rho_{ij}$ 's were determined by performing a maximum-likelihood fit with this form<sup>16</sup> as a function of momentum transfer for events in the  $K^{*-}(890)$  band defined as

$$0.84 \leq M(K\pi)^- \leq 0.94 \text{ GeV}.$$

Figure 40 shows the fraction of  $K^{*-}(890)$  events in this region as a function of momentum transfer as determined from the fits to the  $(K\pi)^-$  effective-mass spectra. The ratio is nearly constant as a function of momentum transfer for the two energies, and averages  $\sim 90\%$ . The large-resonance signal-to-noise ratio, constant over momentum transfer, implies that the  $\rho_{ij}$ 's obtained from fitting without a background subtraction will only have a small systematic error from the nonresonance events. In addition, excellent fits to the decay distributions were obtained. The values of the  $\rho_{ij}$ 's, evaluated in the Jackson frame, are given in Table XV and displayed in Fig. 41. The following structure of the density-matrix elements is observed:

(a)  $\rho_{00}^J$  is  $\sim 0.4$  in the forward region of momentum transfer, and then falls and becomes small and fairly constant for large values of  $-t$ .

(b)  $\operatorname{Re}\rho_{10}^J$  is constant at a value of  $\sim -0.1$  in the

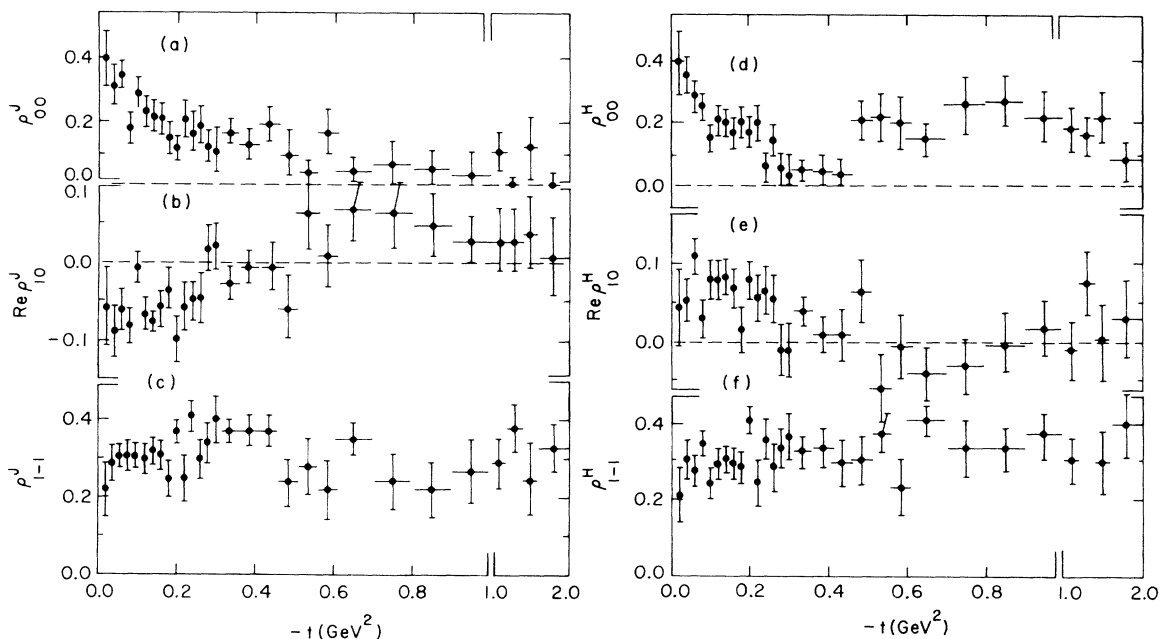


FIG. 41. (a)–(c) Density-matrix elements of the  $K^{*-}(890)$  in the Gottfried-Jackson frame as a function of momentum transfer. The data at 3.9 and 4.6 GeV/c have been combined. (d)–(f) Same as (a)–(c) but the density-matrix elements are evaluated in the helicity frame.

TABLE XV.  $K^{*-}(890)$  density matrices.

$-t$ interval (GeV <sup>2</sup> )	No. of events	Jackson frame			Helicity frame		
		$\rho_{00}$	$\text{Re}\rho_{10}$	$\rho_{1-1}$	$\rho_{00}$	$\text{Re}\rho_{10}$	$\rho_{1-1}$
0.01-0.03	66	0.40 ± 0.09	-0.06 ± 0.05	0.22 ± 0.07	0.39 ± 0.10	0.04 ± 0.05	0.21 ± 0.07
0.03-0.05	137	0.32 ± 0.06	-0.09 ± 0.03	0.29 ± 0.05	0.35 ± 0.07	0.05 ± 0.03	0.03 ± 0.05
0.05-0.07	199	0.35 ± 0.05	-0.06 ± 0.03	0.31 ± 0.03	0.28 ± 0.05	0.11 ± 0.02	0.27 ± 0.04
0.07-0.09	213	0.18 ± 0.05	-0.08 ± 0.02	0.31 ± 0.04	0.25 ± 0.05	0.03 ± 0.03	0.34 ± 0.04
0.09-0.11	224	0.29 ± 0.05	-0.01 ± 0.02	0.31 ± 0.04	0.15 ± 0.04	0.08 ± 0.03	0.24 ± 0.04
0.11-0.13	212	0.23 ± 0.05	-0.07 ± 0.02	0.30 ± 0.04	0.21 ± 0.05	0.08 ± 0.03	0.29 ± 0.04
0.13-0.15	206	0.22 ± 0.05	-0.07 ± 0.02	0.32 ± 0.04	0.20 ± 0.04	0.08 ± 0.03	0.30 ± 0.04
0.15-0.17	176	0.21 ± 0.05	-0.06 ± 0.03	0.31 ± 0.04	0.17 ± 0.05	0.07 ± 0.03	0.29 ± 0.04
0.17-0.19	170	0.15 ± 0.05	-0.03 ± 0.03	0.25 ± 0.05	0.20 ± 0.05	0.02 ± 0.03	0.28 ± 0.04
0.19-0.21	154	0.12 ± 0.04	-0.10 ± 0.03	0.37 ± 0.03	0.17 ± 0.04	0.08 ± 0.02	0.40 ± 0.04
0.21-0.23	138	0.21 ± 0.06	-0.06 ± 0.03	0.25 ± 0.06	0.20 ± 0.06	0.06 ± 0.03	0.24 ± 0.06
0.23-0.25	133	0.17 ± 0.06	-0.05 ± 0.03	0.41 ± 0.04	0.06 ± 0.05	0.07 ± 0.03	0.35 ± 0.05
0.25-0.27	121	0.19 ± 0.06	-0.04 ± 0.03	0.30 ± 0.05	0.14 ± 0.05	0.06 ± 0.03	0.28 ± 0.06
0.27-0.29	124	0.13 ± 0.05	0.02 ± 0.03	0.36 ± 0.05	0.06 ± 0.05	-0.01 ± 0.03	0.33 ± 0.05
0.29-0.31	89	0.11 ± 0.07	0.02 ± 0.03	0.40 ± 0.06	0.03 ± 0.07	-0.01 ± 0.03	0.36 ± 0.06
0.31-0.36	207	0.17 ± 0.04	-0.03 ± 0.02	0.37 ± 0.03	0.05 ± 0.03	0.04 ± 0.02	0.32 ± 0.04
0.36-0.41	143	0.13 ± 0.06	0.00 ± 0.02	0.37 ± 0.04	0.05 ± 0.05	0.01 ± 0.02	0.33 ± 0.05
0.41-0.46	126	0.20 ± 0.06	0.00 ± 0.03	0.37 ± 0.04	0.04 ± 0.04	0.01 ± 0.03	0.29 ± 0.06
0.46-0.51	98	0.10 ± 0.07	-0.06 ± 0.04	0.24 ± 0.07	0.21 ± 0.06	0.07 ± 0.04	0.30 ± 0.06
0.51-0.56	78	0.04 ± 0.04	0.06 ± 0.04	0.28 ± 0.07	0.22 ± 0.08	-0.06 ± 0.05	0.37 ± 0.05
0.56-0.61	79	0.17 ± 0.08	0.01 ± 0.04	0.22 ± 0.08	0.20 ± 0.08	-0.01 ± 0.04	0.23 ± 0.07
0.60-0.70	104	0.05 ± 0.04	0.07 ± 0.04	0.35 ± 0.04	0.15 ± 0.05	-0.04 ± 0.04	0.40 ± 0.04
0.70-0.80	82	0.07 ± 0.07	0.07 ± 0.04	0.24 ± 0.07	0.26 ± 0.08	-0.03 ± 0.04	0.33 ± 0.07
0.80-0.90	85	0.06 ± 0.05	0.05 ± 0.04	0.22 ± 0.07	0.27 ± 0.08	0.00 ± 0.04	0.33 ± 0.05
0.90-1.00	72	0.04 ± 0.07	0.03 ± 0.03	0.27 ± 0.08	0.22 ± 0.08	0.02 ± 0.04	0.37 ± 0.06
1.00-1.20	85	0.11 ± 0.06	0.03 ± 0.04	0.29 ± 0.06	0.18 ± 0.07	-0.01 ± 0.04	0.32 ± 0.06
1.20-1.40	79	0.00 ± 0.02	0.03 ± 0.04	0.38 ± 0.06	0.16 ± 0.06	0.08 ± 0.04	0.57 ± 0.08
1.40-1.60	66	0.13 ± 0.09	0.04 ± 0.05	0.25 ± 0.09	0.22 ± 0.08	0.00 ± 0.05	0.30 ± 0.08
1.60-2.00	76	0.00 ± 0.05	0.01 ± 0.05	0.33 ± 0.07	0.08 ± 0.06	0.03 ± 0.05	0.39 ± 0.08

forward direction, passes through zero at  $-t \approx 0.45$  GeV<sup>2</sup>, changes sign, and stays positive for  $-t \gtrsim 0.45$  GeV<sup>2</sup>.

(c)  $\rho_{1-1}^J$  is large for all  $-t$ , shows a maximum of 0.4 at  $-t \approx 0.25$  GeV<sup>2</sup>, then dips to a value  $\sim 0.3$  for  $-t > 0.45$  GeV<sup>2</sup>.

The small value of  $\rho_{00}^J$  coupled with the large value of  $\rho_{1-1}^J$  is indicative of a strong contribution from vector-meson exchange. The  $\omega$ , and not the  $\rho$ , is the most likely candidate, since charge independence implies that if  $\rho$  exchange is present in the reaction  $K^-p \rightarrow K^{*-}(890)p$ , it must be four times larger in the reaction  $K^-p \rightarrow K^{*0}(890)n$ , in which, as we have seen, the dominant mechanism seems to be  $\pi$  exchange. The rise of  $\rho_{00}^J$  in the region of large forward-backward asymmetry suggests the presence of a  $\pi$ -exchange component in the production mechanism of the reaction  $K^-p \rightarrow K^{*-}(890)p$ .

The  $\rho_{ij}^H$ 's evaluated in the helicity frame, shown in Fig. 41 and listed in Table XV, exhibit a very interesting structure, which, as far as we can determine, has never been reported in any other resonance production. In particular, we see that  $\rho_{00}^H$  de-

creases as a function of momentum transfer, has a minimum at  $-t \approx 0.4$  GeV<sup>2</sup>, and then rises again to a value of  $\sim 0.2$  for  $-t > 0.5$  GeV<sup>2</sup>. Also,  $\text{Re}\rho_{10}^H$  becomes zero at  $-t \approx 0.45$  GeV<sup>2</sup>.

#### 4. Further Comparison of $K^{*-}(890)$ and $K^{*0}(890)$

As previously mentioned, charge independence and Clebsch-Gordan-coefficient considerations indicate that the  $I=1$  cross section should be four times larger in the reaction

$$K^-p \rightarrow K^{*0}(890)n \quad (a)$$

than in

$$K^-p \rightarrow K^{*-}(890)p. \quad (b)$$

In Figs. 42(a) and 42(b) we compare the differential cross section of reaction (b) with  $\frac{1}{4}$  the cross section of reaction (a) at 3.9 and 4.6 GeV/c, respectively. The difference between these two distributions, as shown in Figs. 43(a) and 43(b), then represents the  $I=0$  (plus any  $I=0$  and  $I=1$  interference) contribution to the differential cross section of reaction (b). The features of the latter dis-

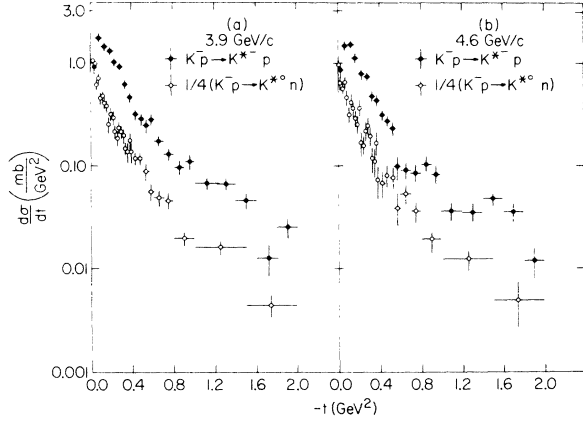


FIG. 42. Differential cross sections for reactions  $K^-p \rightarrow K^{*0}(890)n$ , divided by 4 (open dots) and  $K^-p \rightarrow K^{*0}(890)p$  (black dots). (a) at 3.9 GeV/c; (b) at 4.6 GeV/c.

tributions closely resemble the total distribution for reaction (b) (we recall that the  $I=1$  contribution to this final state is  $\sim 30\%$  of the total cross section). What is especially striking in Figs. 43(a) and 43(b) is the large forward dip. In a previous publication<sup>1</sup> we have noted this observed turning over of the differential cross section and a corresponding lack of a significant dip in the reaction

$$K^-n \rightarrow K^{*0}(890)n. \quad (c)$$

These observations suggested that the  $I=0$  and  $I=1$  exchange amplitudes interfere in the forward momentum-transfer region [the  $I=1$  exchange amplitude couples with a relative change of sign in reactions (b) and (c)].

In order to extract more information on the influence of the exchanged particles and to understand the nature of the dip in  $\rho_{00}^H$ , we proceed to look at the structure of the combination  $\rho_{00} d\sigma/dt$ . It has been demonstrated<sup>17</sup> that  $\rho_{00}^J d\sigma/dt$  (i.e., evaluated in the Jackson frame) projects out the unnatural-parity exchange contribution to the population of the  $t$ -channel helicity-zero states. Under the assumption that absorption corrections are diagonal in the helicities, the corresponding quantity in the helicity frame (i.e.,  $\rho_{00}^H d\sigma/dt$ ) should, at high energies, project out the unnatural-parity contribution to the  $s$ -channel helicity-zero states. However, to order  $1/s$  ( $s$  = square of total energy) in the amplitudes, natural-parity contributions may also be present.<sup>18</sup> We again use charge independence and show<sup>19</sup> in Fig. 44 the distribution of  $\rho_{00}^J d\sigma/dt$  and  $\frac{1}{4} \rho_{00}^J d\sigma/dt$  for reactions (b) (black dots) and (a) (open dots), respectively. We see, except at very low  $-t$ , that these two quantities are equal within their errors as a function of momentum transfer. This is a non-trivial result in that the  $\rho_{00}$  and  $d\sigma/dt$  distributions

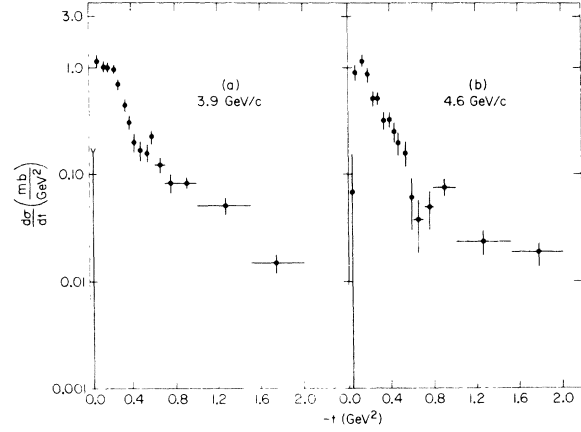


FIG. 43. Subtracted differential cross section,  $d\sigma/dt(K^-p \rightarrow K^{*-}(890)p) - \frac{1}{4} d\sigma/dt(K^-p \rightarrow K^{*0}(890)n)$ . (a) at 3.9 GeV/c; (b) at 4.6 GeV/c.

are very different for reactions (a) and (b). This equality suggests that  $I=0$  unnatural-parity exchange to the  $t$ -channel helicity-zero states gives little, if any, contribution to reaction (b).

The  $\rho_{00}^H d\sigma/dt$  distributions are shown in Fig. 44(b). The reaction (a) distribution (open dots) shows a sharp forward slope which breaks at  $-t \approx 0.2$  GeV<sup>2</sup>, with a shallower slope for  $-t > 0.2$

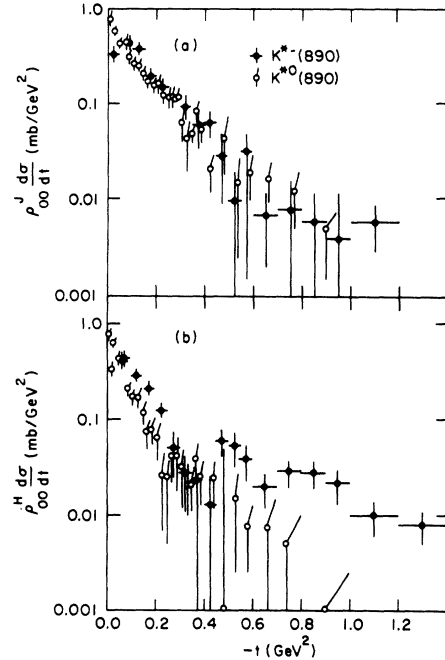


FIG. 44. (a)  $\rho_{00}^J(d\sigma/dt) [\frac{1}{4} \rho_{00}^J(d\sigma/dt)]$  distribution shown as black (open) dots for reaction  $K^-p \rightarrow K^{*-}(890)p$  [ $K^-p \rightarrow K^{*0}(890)n$ ]. (b) Same as (a) but evaluated in the helicity frame.

$\text{GeV}^2$ . The value of  $\rho_{00}^H d\sigma/dt$  for reaction (b) (excluding the first  $-t$  bin) is always larger than one quarter of the corresponding value for reaction (a) except in the region of the dip in  $\rho_{00}^H$  (see above), where  $\rho_{00}^H d\sigma/dt$  [reaction (b)]  $\approx \frac{1}{4} \rho_{00}^H d\sigma/dt$  [reaction (a)]. The simplest interpretation of these trends is that an  $I=0$  unnatural- or natural-parity exchange contributes to  $\rho_{00}^H d\sigma/dt$  in reaction (b). This then requires that the dip in  $\rho_{00}^H d\sigma/dt$  be caused by a zero in this  $I=0$  contribution to the amplitude for production of helicity-zero  $K^*$ 's in the  $s$  channel. The similarity of the  $\rho_{00}^H$  dip structure in reactions (b) and (c) would rule out its being caused by an interference between the  $I=0$  and  $I=1$  exchange amplitudes. It should be noted that, if this dip is due to the structure of the natural-parity-exchange  $s$ -channel amplitudes and if the assumptions<sup>18</sup> of the cut models are correct, then as the energy increases the dip structure should disappear.

## V. PRODUCTION AND DECAY PROPERTIES OF THE $K(1420)$ MESON

### 1. Mass and Width of the $K(1420)$ Meson

In order to extract the mass and width of the  $K(1420)$  meson, as well as to investigate the possible presence of fine structure similar to that reported in some analyses of  $A_2(1300)$ , we have studied reactions 2-5 and 7. A peripheral cut,  $t'(p \rightarrow n) < 0.5 \text{ GeV}^2$  ( $t' = t - t_{\min}$ ), was imposed on the events of reaction 7 in order to reduce the less peripherally produced background. Figure 45 shows the pertinent  $K\pi$  (and  $K\pi\pi$ ) mass distributions from these final states in which strong  $K(1420)$  signals are observed.

The copiously produced reactions 6 and 8 will not be considered in the present analysis since the  $Q$  effect (see Figs. 17-20 of Sec. II) dominated these reactions, and selections (e.g.,  $t'$  cuts) that reduced its presence at the same time considerably diminished the  $K(1420)$  signal.

The widths of the resolution functions (obtained from ideograms of  $\delta$  functions, using mass errors from the kinematic full-error matrix) for events in the  $K(1420)$  region for each of the final states varied from 4.5 to 7.5 MeV (i.e.,  $\sigma$ ) which was adequate to observe any fine structure similar to that observed in some  $A_2(1300)$  experiments. From an investigation of the width of the  $\bar{K}^0$  effective-mass distribution, determined from measurements of the decay  $\pi^+$  tracks and the measured width of the neutron peak in the  $K^-p \rightarrow K^- \pi^+$  MM channel compared to the corresponding resolution functions [see Figs. 46(a) and 46(b)], and the study of the pertinent stretch functions in the  $K(1420)$  region, we feel confident in the reliability of our quoted values for the resolutions.

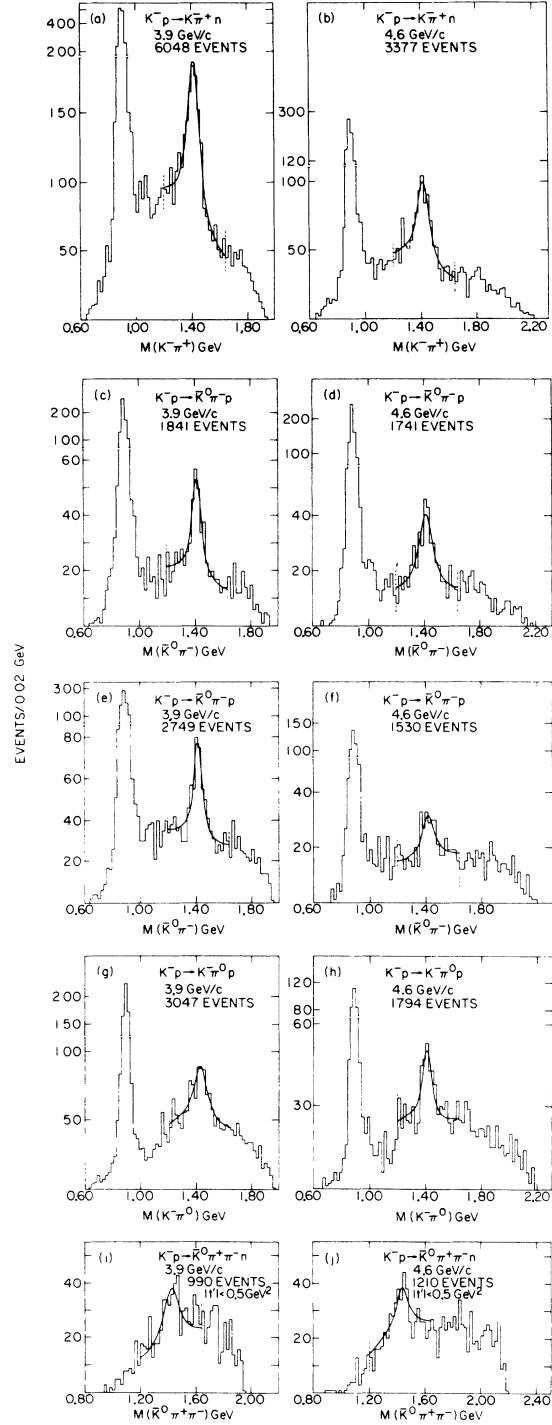


FIG. 45. (a), (c), (e), (g), (i)  $K^- \pi^+$ ,  $\bar{K}^0 \pi^-$ ,  $K^- \pi^0$ , and  $\bar{K}^0 \pi^+ \pi^-$  effective-mass distributions for reactions  $K^- p \rightarrow K^- \pi^+ n$ ,  $K^- p \rightarrow \bar{K}^0 \pi^- p$  (seen  $\bar{K}^0$ ),  $K^- p \rightarrow \bar{K}^0 \pi^+ p$  (unseen  $\bar{K}^0$ ),  $K^- p \rightarrow K^- \pi^0 p$ , and  $K^- p \rightarrow \bar{K}^0 \pi^+ \pi^- n$  at 3.9 GeV/c. The curves are the results of fits using a Breit-Wigner amplitude for the resonance and smooth form for the background. (b), (d), (f), (h), (j) same as (a), (c), (e), (g), (i) but at 4.6 GeV/c.

In Fig. 47 the same distributions shown in Fig. 45 are displayed, but using a finer bin size of 10 MeV and in which only the  $K(1420)$  region [ $1.20 \leq M(K\pi)$  or  $M(K\pi\pi) \leq 1.64$  GeV] is shown. Using a least-squares technique, each of these spectra was fitted to an expression of the form

$$F = \left[ a_R \frac{A}{N_1} + (1 - a_R) \frac{1}{N_2} \right] B,$$

where  $B$  is a linear or quadratic polynomial in the mass,  $N_1$  and  $N_2$  are normalization factors which make  $a_R$  the percentage of resonance events in the fitted region, and  $A$  is the shape of the  $K(1420)$ . Two different parametrizations for  $A$  were used.

(a) Breit-Wigner hypothesis:

$$A = \frac{M^2 \Gamma^2}{(m^2 - M^2)^2 + M^2 \Gamma^2},$$

(b) Dipole hypothesis:

$$A = \left( \frac{\Gamma(m - M)}{(m - M)^2 + \frac{1}{4} \Gamma^2} \right)^2.$$

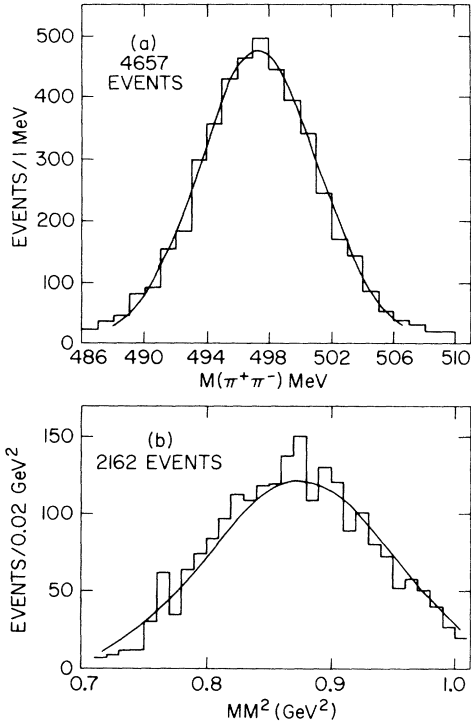


FIG. 46. (a)  $\pi^+\pi^-$  effective-mass distribution calculated using the measured quantities for a subsample of two-prong-plus-vee events. The curve represents the calculated resolution ( $\sigma = 3.9$  MeV) centered at the  $\bar{K}^0$  mass. (b) Missing mass squared for a sample of events [ $K(1420)$  region] of reaction  $K^-p \rightarrow K^-\pi^+n$  at 3.9 GeV/c. The curve represents the obtained resolution ( $\sigma = 38.3$  MeV) centered at the neutron mass.

In both cases, energy-independent widths were used, and the experimentally determined resolution was folded into the theoretical forms. Details of the results of the fits are presented in Table XVI.

The over-all quality of the fits with these parametrizations is given by the  $\chi^2$  probability ( $P_1$  in the table) calculated over the entire region of the fit. A more appropriate estimate of the difference be-

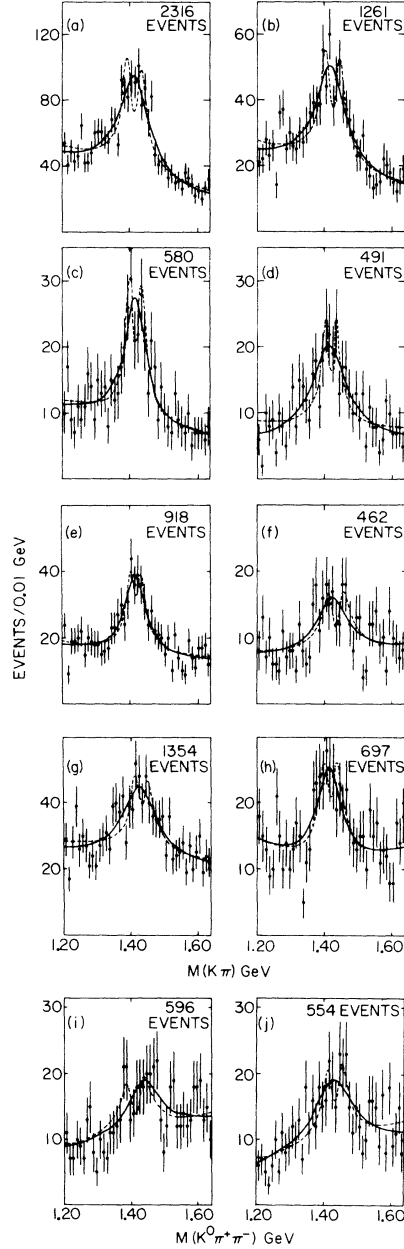


FIG. 47. Same mass distributions as shown in Fig. 45 but using a 10-MeV bin size. The curves are the results of  $\chi^2$  fits using a Breit-Wigner (solid line) and a dipole (dotted line) form for the resonance region.

tween the two hypotheses is obtained by comparison of the  $\chi^2$  probability evaluated in the restricted mass region:  $1.37 \text{ GeV} \leq M(K\pi)$  or  $M(K\pi\pi) \leq 1.47 \text{ GeV}$  ( $P_2$  in the table). This probability corresponds to seven degrees of freedom with the amount, mass, and width of the resonance considered as free parameters. The results quoted in Table XVI show that both the Breit-Wigner and dipole hypotheses give excellent confidence levels for all the channels under investigation, with the exception of the  $K^-\pi^+n$  channel in the 3.9-GeV/c sample. This particular distribution gives a reasonable (5.5%) probability for the Breit-Wigner hypothesis as compared to a 0.006% probability for the dipole parametrization (i.e., the  $P_{\chi^2}$  for the Breit-Wigner is  $\sim 1000$  larger than that for the dipole hypothesis).<sup>20</sup>

The statistical validity of this channel is substantially larger [ $\sim 900$   $K(1420)$  events in the fitted region with  $\sim 500$  resonance events in the region 1.37–1.47 GeV with a signal-to-noise ratio of  $\sim 1.4$ ] than in any of the other reactions studied. The very low probability for the dipole fit in this channel argues strongly against a two-peak interpretation and confirms the observation of Davis *et al.*<sup>21</sup> for the traditional resonance shape of the  $K(1420)$  meson.

In order to stress the previous conclusion, we address ourselves to the following related question. Given the statistical significance of a sample of resonance and background events, and with the assumption that the shape of the resonance is that of a dipole (or Breit-Wigner), we ask how often does the wrong hypothesis [i.e., Breit-Wigner (or dipole)] give a fit with a higher probability than the one corresponding to the parametrization from which the sample was obtained. We have investigated this problem through a Monte Carlo simulation of experiments.<sup>22</sup> Figure 48(a) shows a sample of 2316 events, theoretically distributed according to the parameters of the dipole hypothesis (amount of resonance, mass, width, and shape of the background) obtained from the fit to the experimental distribution of Fig. 47(a). Using these parameters, we have generated 50 "experimental" distributions with the same statistical validity as our experiments, and have then performed fits on the resultant distributions using both dipole and Breit-Wigner forms. The relevant parameters were allowed to vary in these fits. From Fig. 48(b), in which the resulting  $\chi^2$  probability for the Breit-Wigner ( $P_{\text{BW}}$ ) fit is plotted versus the corresponding dipole-fit probability ( $P_{\text{dipole}}$ ), we see that experiments generated according to a two-peak hypothesis do not give fits to the Breit-Wigner hypothesis ( $P_{\chi^2}$  obtained in the 1.37–1.47-GeV region) in which the ratio  $P_{\text{BW}}/P_{\text{dipole}}$  is larger than  $\sim 1$ . Moreover, 86% of these experiments yield Breit-Wigner probabilities,  $P_{\text{BW}} < 0.05$ . We then proceeded from the alter-

TABLE XVI. Parameters of the  $K(1420)$ . (The quoted errors are statistical.)

Momentum (GeV/c)	Channel	Form fitted			Breit-Wigner					Dipole						
		Width R.F. <sup>a</sup> (MeV)	No. of events <sup>b</sup>	No. of events <sup>b</sup>	$M$ (MeV)	$\Gamma$ (MeV)	$P_1^c$ (%)	$P_2^d$ (%)	$M$ (MeV)	$\Gamma$ (MeV)	$P_1^c$ (%)	$P_2^d$ (%)	$M$ (MeV)	$\Gamma$ (MeV)	$P_1^c$ (%)	$P_2^d$ (%)
3.9	$K^-\bar{p} \rightarrow K^-\pi^+n$	7.0	2316	889 ± 102	1416.6 ± 4.0	104.0 ± 15.3	20.2	5.5	1413.9 ± 4.1	29.1 ± 2.6	0.8	0.006				
	$K^-\bar{p} \rightarrow \bar{K}^0(\text{seen})\pi^-\bar{p}$	4.5	580	210 ± 25	1418.7 ± 5.3	76.7 ± 13.2	82.6	15.7	1419.6 ± 2.2	25.0 ± 3.7	95.4	59.9				
	$K^-\bar{p} \rightarrow \bar{K}^0\pi^-\bar{p}$	7.0	918	242 ± 44	1418.6 ± 5.0	67.8 ± 18.1	83.4	73.3	1419.1 ± 3.7	21.5 ± 3.8	78.3	63.6				
	$K^-\bar{p} \rightarrow K^-\pi^-\bar{p}$	7.5	1354	384 ± 60	1426.9 ± 5.7	123.4 ± 15.0	64.0	41.8	1432.7 ± 5.8	26.9 ± 5.3	41.4	42.9				
	$K^-\bar{p} \rightarrow \bar{K}^0\pi^+\pi^-\bar{p}$ <sup>e</sup>	7.5	596	125 ± 40	1435.7 ± 14.2	113.4 ± 58.9	59.5	35.1	1412.2 ± 11.8	43.4 ± 13.2	59.7	58.7				
4.6	$K^-\bar{p} \rightarrow K^-\pi^+n$	7.0	1261	473 ± 30	1420.0 ± 5.3	105.9 ± 18.4	55.7	26.7	1426.1 ± 2.6	30.9 ± 3.6	49.4	41.9				
	$K^-\bar{p} \rightarrow \bar{K}^0(\text{seen})\pi^-\bar{p}$	4.5	491	234 ± 64	1414.9 ± 9.1	124.7 ± 24.1	72.5	46.1	1421.0 ± 3.1	25.2 ± 4.8	39.5	30.7				
	$K^-\bar{p} \rightarrow \bar{K}^0\pi^-\bar{p}$	7.0	462	116 ± 42	1421.5 ± 14.9	104.2 ± 40.0	41.9	30.7	1434.6 ± 7.1	38.3 ± 8.7	50.6	52.8				
	$K^-\bar{p} \rightarrow K^-\pi^0\bar{p}$	7.5	697	190 ± 56	1413.8 ± 8.0	87.7 ± 31.5	55.4	82.4	1419.0 ± 6.6	28.1 ± 8.7	49.7	56.3				
	$K^-\bar{p} \rightarrow \bar{K}^0\pi^+\pi^-\bar{p}$ <sup>e</sup>	7.5	554	213 ± 45	1422.4 ± 9.6	149.7 ± 44.5	55.4	52.8	1431.3 ± 4.3	32.6 ± 6.9	50.0	85.6				

<sup>a</sup> R.F. = resolution function.

<sup>b</sup> Events in the region 1.20–1.64 GeV.

<sup>c</sup> Confidence level corresponding to the region 1.20–1.64 GeV.

<sup>d</sup> Confidence level corresponding to the region 1.37–1.47 GeV.

<sup>e</sup> The cut  $|\mathbf{p}'| < 0.5 \text{ GeV}^2$  has been imposed.

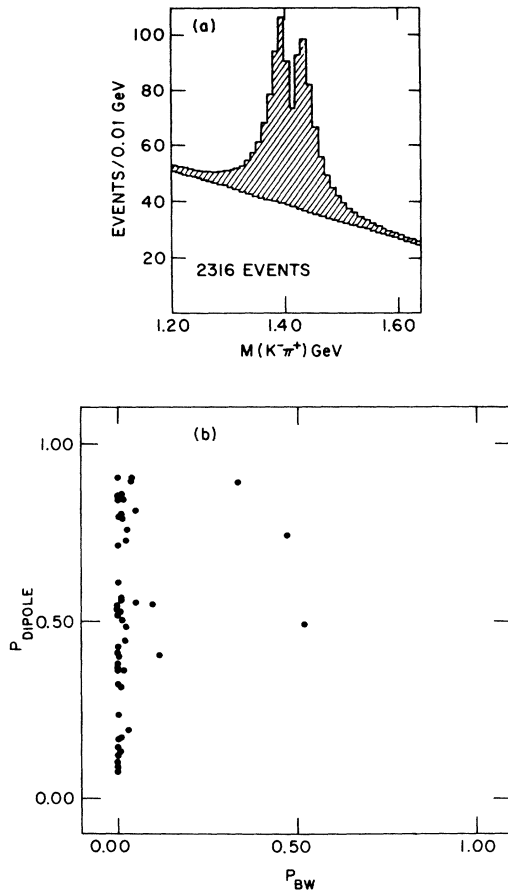


FIG. 48. (a) Histogram of the best dipole-fit curve to the distribution of Fig. 47(a) (reaction  $K^-p \rightarrow K^-\pi^+n$  at 3.9 GeV/c). The shaded area represents the amount of resonance events obtained from the fit. (b)  $P_{\text{BW}}$  vs  $P_{\text{dipole}}$  distribution for the 50 Monte Carlo experiments generated according to the form shown in (a). The  $\chi^2$  probabilities have been calculated in the 1.37–1.47-GeV mass region.

nate point of view and generated events according to the best fit of the Breit-Wigner form to Fig. 47(a). We see in Fig. 49 that experiments generated according to this one-peak hypothesis often give equivalent probabilities for the dipole fit. The results of these Monte Carlo simulations imply that one should not be surprised to find reasonable fits to a dipole hypothesis. This means that one cannot conclude from similar  $\chi^2$  probabilities for both interpretations evidence for a two-peak structure.

The fits on our largest statistics experiment have shown that the single-peak form gives a substantially larger  $\chi^2$  probability than does the dipole form (i.e.,  $P_{\text{BW}}/P_{\text{dipole}} \sim 1000$ ). Our data, therefore, strongly favor an unsplit  $K(1420)$ .

The previous considerations and analysis, together with the smaller statistics of the other

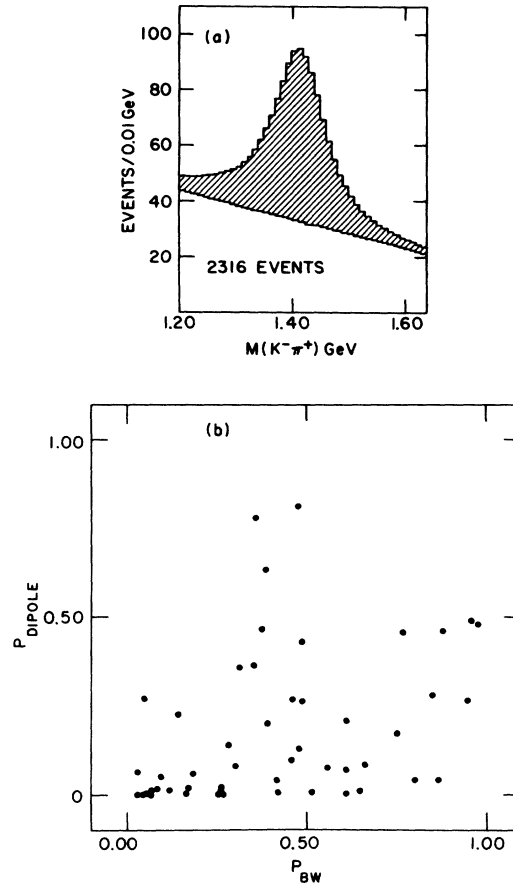


FIG. 49. Same as Fig. 48 but using the best Breit-Wigner-fit curve to the distribution of Fig. 47(a) (reaction  $K^-p \rightarrow K^-\pi^+n$  at 3.9 GeV/c).

samples under investigation (along with the quoted experimental resolution), mean that we must interpret the similarity in goodness of fit of the two hypotheses to these mass spectra as likely to occur from events originating from a singly peaked  $K(1420)$  meson. Figures 50 and 51, which show a similar Monte Carlo study for reaction  $K^-p \rightarrow \bar{K}^0(\text{seen})\pi^-p$  at 3.9 GeV/c [experimental mass spectrum of Fig. 47(c)], containing a sample of only 210  $K(1420)$  events, clearly justify the above remarks.

Since no statistically significant differences appear in the Breit-Wigner fits to the individual distribution,<sup>23</sup> we have combined the samples shown in Fig. 45 in order to extract the masses and widths of the neutral and charged states of the  $K(1420)$ . Figure 52 shows the compiled data for the neutral and charged modes, respectively. Performing fits similar to the ones previously discussed (we used 5-MeV bin intervals and a least-squares method), we obtained the following.

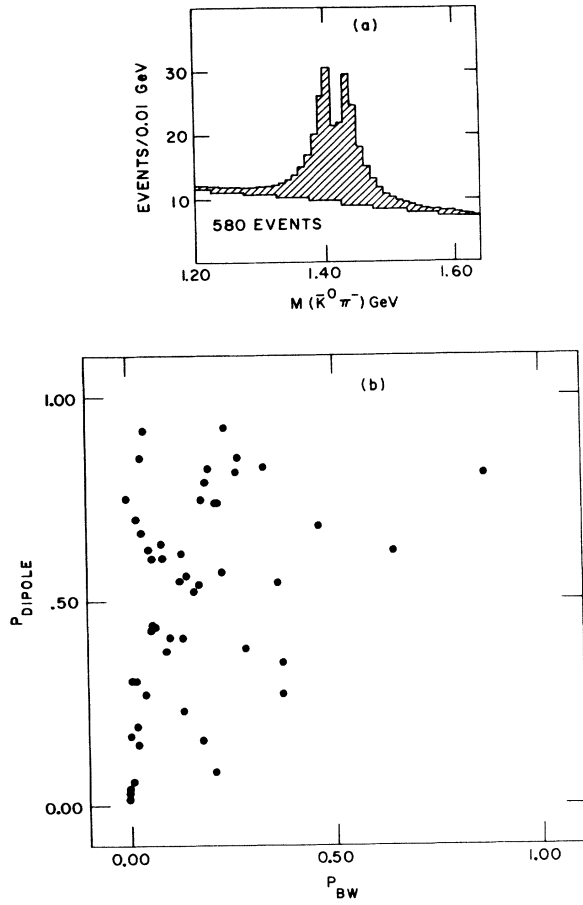


FIG. 50. Same as Fig. 48 but for reaction  $K^-p \rightarrow \bar{K}^0(\text{seen})\pi^+p$  [distribution of Fig. 47(c)] at 3.9 GeV/c.

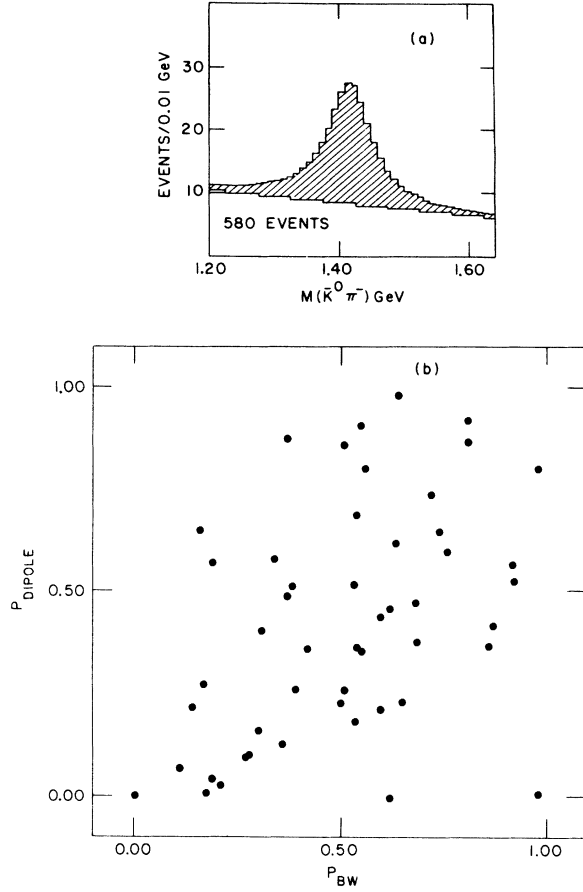


FIG. 51. Same as Fig. 49 but for reaction  $K^-p \rightarrow \bar{K}^0(\text{seen})\pi^-p$  [distribution of Fig. 47(c)] at 3.9 GeV/c.

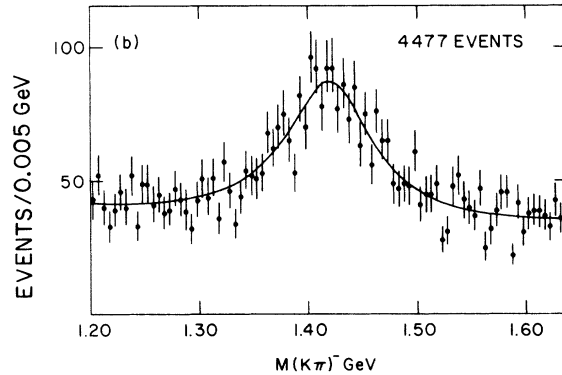
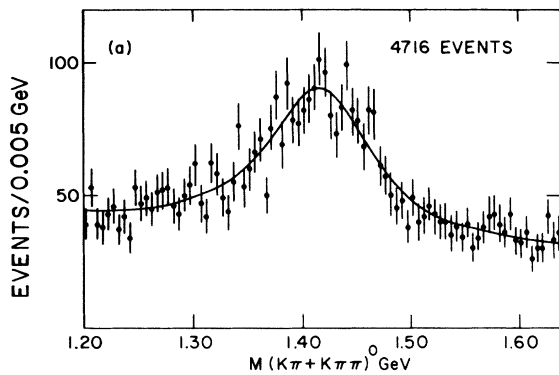


FIG. 52. (a)  $K^-p \rightarrow K^- \pi^+ n$  and  $K^-p \rightarrow \bar{K}^0 \pi^+ \pi^- n$  combined effective-mass distribution from reactions  $K^-p \rightarrow K^- \pi^+ n$  and  $K^-p \rightarrow \bar{K}^0 \pi^+ \pi^- n$ . The data at 3.9 and 4.6 GeV/c have been combined. (b)  $(K\pi)^-$  effective-mass distribution from reactions  $K^-p \rightarrow \bar{K}^0 \pi^- p$  and  $K^-p \rightarrow K^- \pi^0 p$  combined. The data at 3.9 and 4.6 GeV/c have been combined.

(a) Neutral mode:

$$1800 K^0(1420) \text{ events, } M = 1419.1 \pm 3.7 \text{ MeV,}$$

$$\Gamma = 116.6^{+10.3}_{-15.5} \text{ MeV, } P_{\chi^2} = 60.6\%;$$

(b) Charged mode:

$$1400 K^-(1420) \text{ events, } M = 1420.0 \pm 3.1 \text{ MeV,}$$

$$\Gamma = 94.7^{+15.1}_{-12.5} \text{ MeV, } P_{\chi^2} = 12.2\%,$$

where the quoted number of events and  $\chi^2$  probabilities refers to the region shown in the figures (1.20–1.64 GeV).<sup>24</sup> The quoted errors on the masses and widths have been increased to take into account uncertainties due to the different background forms and different mass regions used in the fitting procedure.

Since the form of the  $K(1420)$  decay angular distributions (see Sec. IV 4) suggests the presence of interference effects, which are momentum-transfer-dependent, we have also investigated the resonance parameters for both the neutral and charged modes as a function of momentum transfer. Using two  $|t'|$  regions for each mode ( $|t'| \leq 0.5 \text{ GeV}^2$  and  $|t'| \geq 0.5 \text{ GeV}^2$  for the neutral mode and  $|t'| \leq 0.3 \text{ GeV}^2$  and  $|t'| \geq 0.3 \text{ GeV}^2$  for the charged mode) and performing fits in the manner described previously, we obtained values for the mass and width which

were in agreement with the ones quoted above and consistent among themselves. In conclusion, our experiment shows no significant evidence for a complex structure of the  $K(1420)$  meson.

## 2. Branching Ratios

We now proceed to discuss the measurement of the  $K(1420)$  decay rates into two-body and quasi-two-body modes. In a previous publication,<sup>1</sup> we stressed the advantage in using the charge-exchange reactions to measure these branching ratios, pointing out that previous determinations were not completely reliable because the number of resonance events in the  $K\pi\pi$  final state suffered either from small statistics or from confusion due to the presence of the  $Q$  enhancement in the non-charge-exchange channels. This work follows our previous approach, with the addition of new data, and also presents an alternative parametrization of the three-body-decay Dalitz plot which includes interference effects. Both methods lead to similar results and conclusions.

The  $K(1420)$  decay rates into  $K(890)\pi$  and  $K\rho$  were obtained by investigation of the reaction

$$K^- p \rightarrow \bar{K}^0 \pi^+ \pi^- n$$

for the combined samples at 3.9 and 4.6 GeV/ $c$  (some 5.0-GeV/ $c$  data were also included). In Fig. 53 the  $\bar{K}^0 \pi^+ \pi^-$  effective-mass spectrum is shown after a peripheral selection was imposed,  $\cos\theta^* > 0.6$  for the 3.9-GeV/ $c$  data and  $\cos\theta^* > 0.8$  for the 4.6- and 5.0-GeV/ $c$  data ( $\theta^*$  is the scattering angle between the target proton and the outgoing neutron in the over-all center-of-mass system). A large  $K(1420)$  signal ( $325 \pm 45$  events) is seen with no evidence for a broad low-mass enhancement. Using a matrix element containing a Breit-Wigner shape for the  $K(1420)$  and a polynomial in the mass variable for the background, we have performed a fit to this mass spectrum. The results of the fit are shown as the solid curve in Fig. 53.

Figure 54 shows the  $M(\bar{K}^0 \pi^-)$  vs  $M(\pi^- \pi^+)$  scatter plot for the  $K(1420)$  region defined as  $1.34 \leq M(\bar{K}^0 \pi^- \pi^+) \leq 1.50 \text{ GeV}$ . A feature of this plot is the accumulation of events in the  $K(890)\text{-}\rho$  overlap region which is caused by the  $\sin^2\theta$  helicity angular distribution of the vector mesons decaying from a resonance with  $J^P$  in the  $1^-, 2^-, 3^-$  series. This configuration causes a systematic uncertainty when traditional methods of determining the branching fractions are used (taking  $K\pi$  and  $\pi\pi$  cuts and examining with background-subtraction techniques the resultant  $K\pi\pi$  effective-mass spectrum). To avoid this difficulty, we fitted the Dalitz plot for the  $K(1420)$  region by a maximum-likelihood method with a probability density of the form

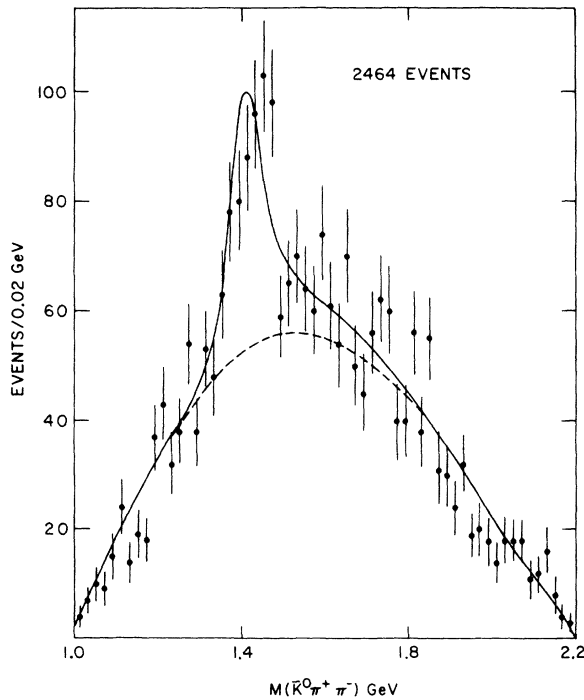


FIG. 53.  $\bar{K}^0 \pi^+ \pi^-$  effective-mass spectrum from reaction  $K^- p \rightarrow \bar{K}^0 \pi^+ \pi^- n$  at 3.9, 4.6, and 5.0 GeV/ $c$ . Events with  $\cos\theta^* > 0.6$  for the 3.9-GeV/ $c$  data, and  $\cos\theta^* > 0.8$  for the 4.6- and 5.0-GeV/ $c$  samples were selected.

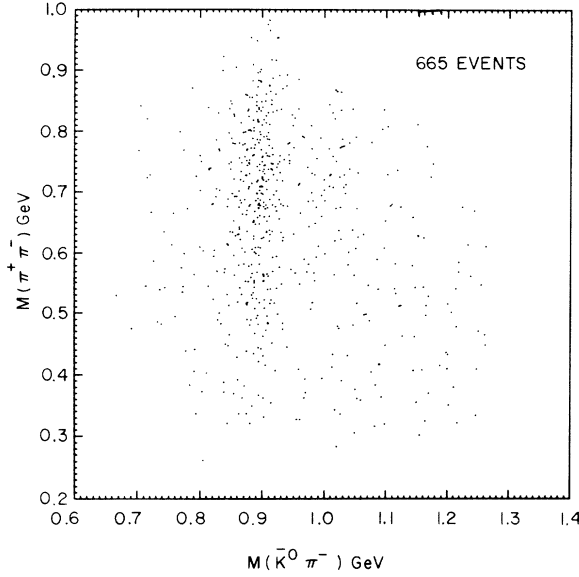


FIG. 54.  $M(\bar{K}^0\pi^-)$  vs  $M(\pi^+\pi^-)$  distribution for events in the  $K^0(1420)$  region [ $1.34 \leq M(\bar{K}^0\pi^+\pi^-) \leq 1.50$  GeV].

$$|M|^2 = \epsilon |M_{1420}|^2 + (1 - \epsilon) |M_{\text{BKG}}|^2.$$

This form does not include possible interference effects between resonance and a background component with the same  $J^P$  as the resonance.

The parameter  $\epsilon$  is the fraction of resonance events in the  $K(1420)$  region (the fit to Fig. 53 gave  $\epsilon = 0.34$ ). For the background we assume flat distributions along the  $K(890)$  and  $\rho$  bands and express

$$|M_{\text{BKG}}|^2 = \beta_1 \frac{|\text{BW}_{890}|^2}{\sum \int |\text{BW}_{890}|^2 d\phi} + \beta_2 \frac{|\text{BW}_{\rho}|^2}{\sum \int |\text{BW}_{\rho}|^2 d\phi} + \frac{1 - \beta_1 - \beta_2}{\sum \int d\phi},$$

where  $\sum \int d\phi$  implies integration over the  $\bar{K}^0\pi^+\pi^-$  Dalitz plot plus sum over events,  $\text{BW}_{890}$  and  $\text{BW}_{\rho}$  are the usual Breit-Wigner amplitudes for the  $K(890)$  and  $\rho(760)$ , and  $\beta_1$  ( $\beta_2$ ) represents the fraction of  $K(890)$  ( $\rho$ ) in the background under the  $K(1420)$  determined from the mass regions adjacent to the  $K(1420)$  ( $1.18 \leq M_{\bar{K}^0\pi^+\pi^-} \leq 1.34$  GeV and  $1.50 \leq M_{\bar{K}^0\pi^+\pi^-} \leq 1.66$  GeV).

Two different parametrizations were used to describe the resonance term  $|M_{1420}|^2$ . First, we followed the simple approach and neglected interference effects between the  $K(890)\pi$  and  $K\rho$  decay modes so that

$$|M_{1420}|^2 = \alpha_1 \frac{|\text{BW}_{890}|^2 \sin^2\theta_{890}}{\sum \int |\text{BW}_{890}|^2 \sin^2\theta_{890} d\phi} + \alpha_2 \frac{|\text{BW}_{\rho}|^2 \sin^2\theta_{\rho}}{\sum \int |\text{BW}_{\rho}|^2 \sin^2\theta_{\rho} d\phi},$$

where  $\alpha_1$  ( $\alpha_2$ ) is the  $K(1420)$  branching fraction into  $K(890)\pi$  ( $K\rho$ ) with  $\alpha_1 + \alpha_2 = 1$ ,<sup>25</sup> and  $\sin^2\theta_{890}$  ( $\sin^2\theta_{\rho}$ ) is the helicity angular distribution of the  $\bar{K}^0$  ( $\pi^+$ ) in the rest frame of the  $\bar{K}^0\pi^-$  ( $\pi^+\pi^-$ ). The results of the maximum-likelihood fit gave<sup>26</sup>

$$\alpha_1 [K^0(1420) \rightarrow K_{890}^- (-\bar{K}^0\pi^-)\pi^-] = 0.80 \pm 0.08,$$

$$\alpha_2 [K^0(1420) \rightarrow \bar{K}^0\rho^0] = 0.20 \pm 0.08.$$

Figures 55(a) and 55(c) show the  $\pi^+\pi^-$  ( $\bar{K}^0\pi^-$ ) effective-mass projections of the  $K(1420)$  Dalitz plot. The helicity angular distributions in the  $\rho$  [ $0.63 \leq M(\pi^+\pi^-) \leq 0.89$  GeV] and  $K(890)$  [ $0.84 \leq M(\bar{K}^0\pi^-) \leq 0.94$  GeV] bands are shown in Figs. 55(b) and 55(d). The accompanying curves are the Monte Carlo-generated predictions obtained by using the simple noninterference model with the values of the parameters  $\alpha_1$  and  $\alpha_2$  given above. Excellent agreement between theoretical predictions and experimental distributions is obtained.<sup>27</sup>

In the second approach the possibility of interference effects between the quasi-two-body decay modes of the  $K(1420)$  was taken into account. The following parametrization of the  $K(1420)$  decay amplitude was used:

$$M_{1420} = \sqrt{\alpha_1} \frac{\text{BW}_{890} \sin\theta_{890}}{(\sum \int |\text{BW}_{890}|^2 \sin^2\theta_{890} d\phi)^{1/2}} + \sqrt{\alpha_2} e^{i\phi} \frac{\text{BW}_{\rho} \sin\theta_{\rho}}{(\sum \int |\text{BW}_{\rho}|^2 \sin^2\theta_{\rho} d\phi)^{1/2}},$$

with  $\alpha_1 + \alpha_2 = 1$ .

With this matrix element, we performed a maximum-likelihood fit and obtained

$$\sqrt{\alpha_1} = 0.91 \pm 0.06,$$

$$\sqrt{\alpha_2} = 0.41 \pm 0.12,$$

$$\Phi = 17^\circ \pm 14^\circ,$$

which correspond to the decay rates

$$\alpha_1 [K^0(1420) \rightarrow K_{890}^- (-\bar{K}^0\pi^-)\pi^+] = 0.83 \pm 0.10,$$

$$\alpha_2 [K^0(1420) \rightarrow \bar{K}^0\rho^0] = 0.17 \pm 0.10.$$

We see that both parametrizations led to the same decay parameters. The interference model also provided a good representation of the decay Dalitz plot. The predictions for the relevant distributions are similar to the ones obtained with the simple noninterference hypothesis described above.

The  $K\pi\pi/K\pi$  branching fractions were obtained by comparison of reactions 4 and 7 at 3.9 and 4.6 GeV/c, separately. Figures 56(a) and 56(b) show the  $K^-\pi^+$  effective-mass spectra at 3.9 and 4.6 GeV/c, respectively, after a peripheral selection ( $\cos\theta^* > 0.6$  at 3.9 GeV/c and  $\cos\theta^* > 0.8$  at 4.6 GeV/c) was imposed. Figures 56(c) and 56(d) contain the corresponding  $\bar{K}^0\pi^+\pi^-$  effective-mass dis-

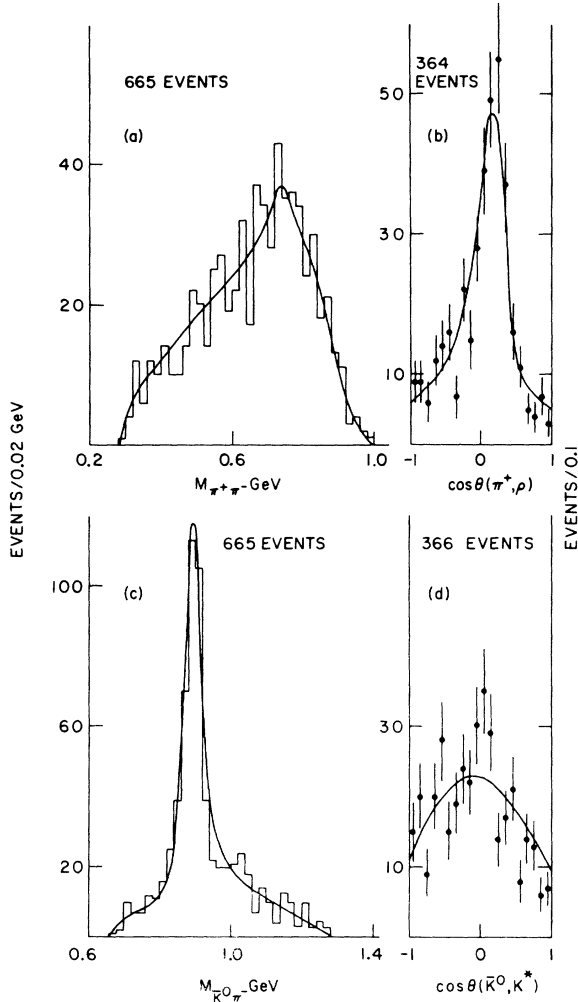


FIG. 55. (a)  $M(\pi^+\pi^-)$  projection of the  $K(1420)$  Dalitz plot. (b) Helicity angular distribution in the  $\rho$  rest frame for events in the  $K(1420)$  region. (c)  $M(\bar{K}^0\pi^-)$  projection of the  $K(1420)$  Dalitz plot. (d) Helicity angular distribution in the  $K(890)$  rest frame for events in the  $K(1420)$  region.

tributions. The number of  $K(1420)$  resonant events was obtained by fitting these experimental distributions with an incoherent superposition of a Breit-Wigner form and a polynomial in the mass variable for the background. The  $K(1420)$  mass and width were kept fixed during the fitting procedure. In Table XVII the number of resonance events and the corresponding cross sections are displayed. Corrections were included for undetected decay modes, probability cuts, and  $\bar{K}^0$  detection efficiencies, as well as for the fact that different portions of the film were analyzed for different final states.<sup>28</sup> Using these cross sections and the pertinent Clebsch-Gordan coefficients, the  $K(890)\pi/K\pi$  and  $K\rho/K\pi$  branching ratios were obtained and are given in

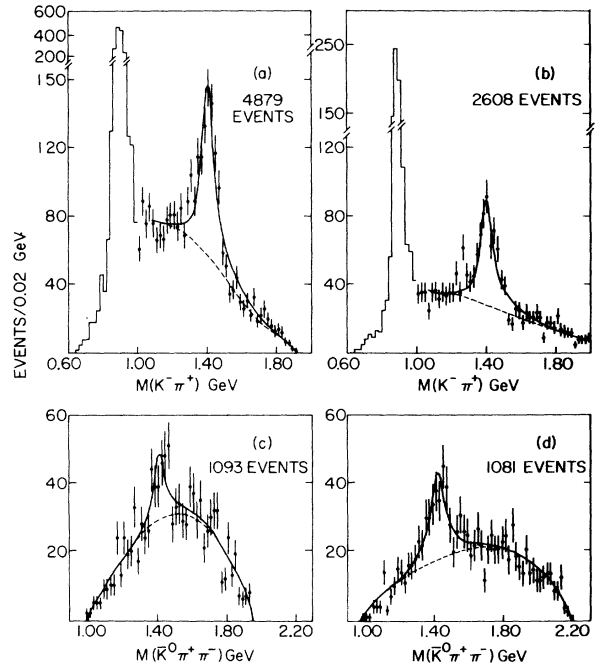


FIG. 56. (a)  $K^-\pi^+$  effective-mass spectrum from reaction  $K^-p \rightarrow K^-\pi^+n$  at 3.9 GeV/c for events with  $\cos\theta^* > 0.6$ . (b) Same as (a) but at 4.6 GeV/c and for events with  $\cos\theta^* > 0.8$ . (c)  $\bar{K}^0\pi^+\pi^-$  effective-mass spectrum from reaction  $K^-p \rightarrow \bar{K}^0\pi^+\pi^-n$  at 3.9 GeV/c for events with  $\cos\theta^* > 0.6$ . (d) Same as (c) but at 4.6 GeV/c and for events with  $\cos\theta^* > 0.8$ .

Table XVII. As previously noted,<sup>1</sup> our value for the  $K(890)\pi/K\pi$  branching ratio ( $0.47 \pm 0.08$ ) significantly disagrees with the compiled world average ( $0.722 \pm 0.087$ ).<sup>29</sup> Since previous experiments have limited statistics and/or derive this ratio from reactions involving  $Q$  production, and since in some cases the quoted errors are unrealistically small, we attach more reliability to our measured value. It should also be noted that our measurement of the branching ratios is in excellent agreement with the predictions from an unbroken SU(3) analysis of the  $2^+$  nonet, as can be seen in Table XVIII.<sup>30</sup>

Other decay modes were sought by investigating  $K(1420)$ 's produced recoiling against a proton. These involve reactions 5, 6, 8, and 9. As previously discussed, reactions 6 and 8 are ill-suited for the determination of the  $K(1420) \rightarrow K\pi\pi$  decay mode. This is illustrated in Fig. 57(a) where the  $(K\pi\pi)^-$  effective mass is plotted for 13 837 events of reaction 8 and 5526 events of reaction 6 for the combined sample at 3.9 and 4.6 GeV/c. It is clearly very difficult to estimate the number of  $K(1420)$  events. Even when the peripherally produced events ( $\cos\theta^* > 0.9$ ) are removed, the  $K(1420)$  signal-to-noise ratio is only marginally improved [shaded area in Fig. 57(a)]. The  $\bar{K}^0\pi^-$  effective-

TABLE XVII.  $K(1420)$  decay modes.

Final state	Selection	Number of observed events		Corrected cross section ( $\mu\text{b}$ ) <sup>a</sup>	
		3.9 GeV/c	4.6 GeV/c	3.9 GeV/c	4.6 GeV/c
$\bar{K}^0\pi^+\pi^-/n$	$\cos\theta^* > 0.6$ at 3.9 GeV/c and	119 ± 29	149 ± 29	59 ± 14	67 ± 13
$K^-\pi^+/n$	$\cos\theta^* > 0.8$ at 4.6 GeV/c	606 ± 41	397 ± 38	148 ± 10	147 ± 17
$\bar{K}^0\pi^-/p$		474 ± 46		107 ± 10 <sup>b</sup>	
$K^-\omega/p$		67 ± 50		8 ± 6	
$K^-\eta/p$		0 ± 6		≤ 6 <sup>c,d</sup>	
Branching ratios					
$K^*\pi/K\pi$	$K\rho/K\pi$	$K\omega/K\pi$	$K\eta/K\pi$		
0.47 ± 0.08	0.16 ± 0.05	0.05 ± 0.04	≤ 0.04		

<sup>a</sup> Corrected for probability cuts.<sup>b</sup> Corrected for unseen  $K^0$  decay.<sup>c</sup> Corrected for unseen resonance decays.<sup>d</sup> 2-standard-deviation upper limit.

mass spectrum for reaction 5 is shown in Fig. 57(b), again for the combined data, and the shaded histogram shows the result of removing peripheral events ( $\cos\theta^* > 0.9$ ). Using the number of  $K(1420)$  events obtained from a fit to this mass spectrum and the  $K\pi/K\pi\pi$  branching fraction derived from reactions 4 and 7, the number of  $K(1420)$  events in the corresponding  $K\pi\pi$  spectrum of reactions 6 and 8 has been estimated. The curve shown in Fig. 57(a) is the result of a fit which includes this number of  $K(1420)$  events. The predicted number of events is consistent with the observed signal, but

it is apparent that a branching-ratio determination based on this channel would be subject to large uncertainties. The  $K^-\eta$  and  $K^-\omega$  effective-mass spectra for reaction 9 at 3.9 and 4.6 GeV/c are shown in Figs. 57(c) and 57(d). Again, the numbers of  $K(1420)$  events were extracted in the manner indicated above. The corrected cross sections for these two channels are quoted in Table XVII. The  $K\eta/K\pi$  and  $K\omega/K\pi$  branching ratios derived from these numbers, given in Table XVII, are consistent with the world averages and agree with the SU(3) predictions.

TABLE XVIII.  $J^P = 2^+$  SU(3) comparison.

$2^+ \rightarrow 1^-0^-$	Decay amplitude <sup>a</sup>	$\Gamma_{\text{exp}}$ (MeV)	$\Gamma_{\text{SU(3)}}$ (MeV)
$A_2(1307) \rightarrow \rho\pi$	$\frac{1}{3}\sqrt{6} A_a^8$	67.0 ± 7.9	71
$K(1420) \rightarrow K(890)\pi$	$\frac{1}{2} A_a^8$	29.4 ± 6.1	24
$K(1420) \rightarrow K\rho$	$\frac{1}{2} A_a^8$	10.0 ± 3.3	7
$K(1420) \rightarrow K\omega$	$\frac{1}{2} A_a^8 \sin\theta_3$	3.1 ± 2.5	5
$f(1500) \rightarrow K(890)K$	$1 A_a^8 \cos\theta_2$	9.0 ± 9.0	9
$\chi^2 = 2.3, \text{NC} = 4$			
$2^+ \rightarrow 0^-0^-$			
$A_2(1307) \rightarrow K\bar{K}$	$\frac{1}{5}\sqrt{15} A_s^8$	6.5 ± 1.3	7.3
$A_2(1307) \rightarrow \pi\eta$	$\frac{1}{5}\sqrt{10} A_s^8 \cos\theta_0 - 1 A_1 \sin\theta_0$	16.5 ± 3.0	14.0
$A_2(1307) \rightarrow \pi\eta'$	$\frac{1}{5}\sqrt{10} A_s^8 \sin\theta_0 + A_1 \cos\theta_0$	0.0 ± 2.7	0.0
$K(1420) \rightarrow K\pi$	$(3/\sqrt{10}) A_s^8$	62.5 ± 7.5	64.0
$K(1420) \rightarrow K\eta$	$(\frac{1}{10})^{1/2} A_s^8 \cos\theta_0$	0.0 ± 1.3	2.0
$f(1250) \rightarrow \pi\pi$	$\sqrt{3} [(\frac{1}{8})^{1/2} A_1 \cos\theta_2 - (\frac{1}{5})^{1/2} A_s^8 \sin\theta_2]$	150.0 ± 15.0	152.0
$f(1250) \rightarrow K\bar{K}$	$1[(\frac{1}{2})^{1/2} A_1 \cos\theta_2 + (\frac{1}{5})^{1/2} A_s^8 \sin\theta_2]$	...	7.0
$f(1250) \rightarrow \eta\eta$	$-1[(\frac{1}{8})^{1/2} A_1 \cos\theta_2 + (\frac{1}{5})^{1/2} A_s^8 \sin\theta_2] \cos^2\theta_0$	...	0.0
$f(1500) \rightarrow \pi\pi$	$-\sqrt{3} [(\frac{1}{8})^{1/2} A_1 \sin\theta_2 + (\frac{1}{5})^{1/2} A_s^8 \cos\theta_2]$	0.1 ± 7.0	2.5
$f(1500) \rightarrow K\bar{K}$	$1[-(\frac{1}{2})^{1/2} A_1 \sin\theta_2 + (\frac{1}{5})^{1/2} A_s^8 \cos\theta_2]$	69.0 ± 25.0	45.0
$f(1500) \rightarrow \eta\eta$	$1[(\frac{1}{8})^{1/2} A_1 \sin\theta_2 - (\frac{1}{5})^{1/2} A_s^8 \cos\theta_2] \cos^2\theta_0$	0.1 ± 7.0	12.0
$\chi^2 = 7.4, \text{NC} = 6$			

<sup>a</sup> The mixing angles used were  $\theta_0 = 10^\circ$ ,  $\theta_2 = 30^\circ$ , and  $\theta_3 = 40^\circ$ .

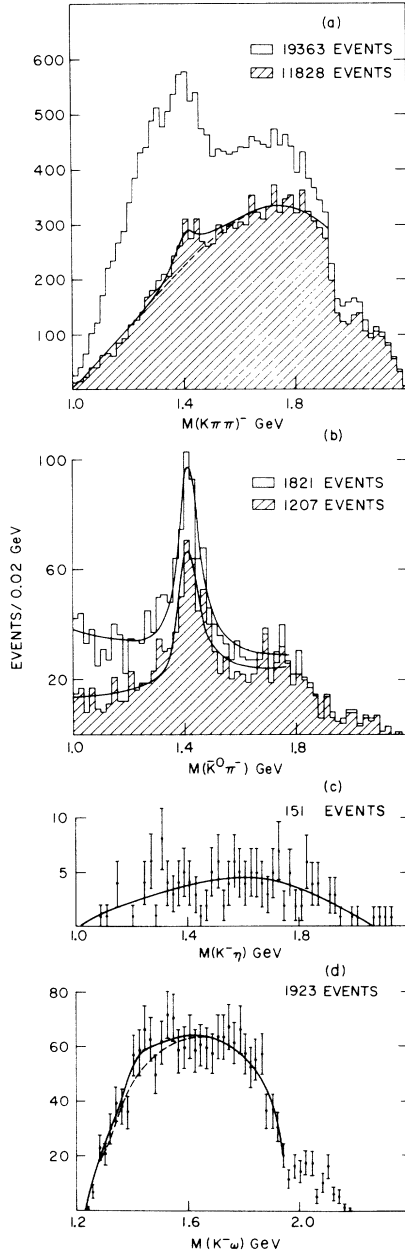


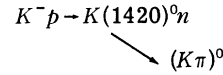
FIG. 57. (a)  $(K\pi\pi)^-$  effective-mass spectrum from reactions  $K^-p \rightarrow K^-\pi^+\pi^-p$  and  $K^-p \rightarrow \bar{K}^0\pi^-\pi^0p$ . The shaded area is the same mass spectrum, but for events with  $\cos\theta^* < 0.9$ . The curve represents the result of a fit in which the number of  $K(1420)$  events is fixed at the value predicted from the branching ratio derived in the text and in which a polynomial background is used. (b)  $\bar{K}^0\pi^-$  effective-mass spectrum from reaction  $K^-p \rightarrow \bar{K}^0\pi^-\pi^0p$ . The shaded area is the same mass spectrum, but for events with  $\cos\theta^* < 0.9$ . The curves are the result of the fits described in the text. (c)  $K^-\eta$  effective-mass spectrum. (d)  $K^-\omega$  effective-mass spectrum. The data at 3.9 and 4.6 GeV/c have been combined in this figure.

### 3. Differential and Total Cross Sections

In this section the differential and total  $K(1420)$  cross sections at 3.9 and 4.6 GeV/c are presented. The differential production cross sections,  $d\sigma/dt'$ , were obtained in each interval of  $-t'$  from maximum-likelihood fits on the appropriate  $K\pi$  effective-mass spectra [in the region  $1.10 \leq M(K\pi) \leq 1.80$  GeV]. The form utilized in the fits consisted of a simple Breit-Wigner shape (with mass and width fixed at the values determined in Sec. V 1) and a polynomial in the mass for the background.

#### 3.1. Neutral $K(1420)$

The number of events obtained in the manner described above from the fits to the reaction  $K^-p \rightarrow K^-\pi^+n$  is given in Table XIX. Also indicated are the  $K(1420)^0$  two-body cross sections, which have been corrected for the undetected  $\bar{K}^0\pi^0$  decay mode as well as for probability cuts imposed on reaction 4. The differential cross sections shown in Fig. 58 have been fitted to simple forms of the type  $e^{bt'}$  and  $e^{bt'+ct'^2}$  over several  $-t'$  intervals. The parameters so obtained and the corresponding  $\chi^2$  are given in Table XX. The total cross sections for the reaction

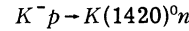


at the two momenta were measured to be

$$3.9 \text{ GeV}/c: \sigma = 340 \pm 40 \mu\text{b},$$

$$4.6 \text{ GeV}/c: \sigma = 321 \pm 24 \mu\text{b}.$$

Finally, after folding in the  $K^*(890)\pi$ ,  $K\rho$ , and  $K\omega$  decay rates, the total cross sections for the reaction



were obtained and are given in Table XXI.

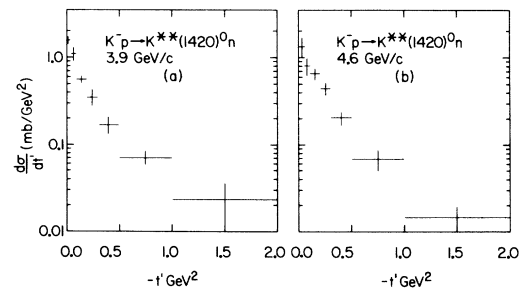


FIG. 58. Differential cross section for reaction  $K^-p \rightarrow K(1420)^0n$ : (a) at 3.9 GeV/c; (b) at 4.6 GeV/c.

TABLE XIX. Differential cross sections for reaction  $K^-p \rightarrow K(1420)^0n \rightarrow (K\pi)^0n$  at 3.9 and 4.6 GeV/c.

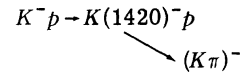
$ t' $ interval (GeV <sup>2</sup> )	3.9 GeV/c		4.6 GeV/c	
	No. $K(1420)$ events	Corrected $d\sigma/dt'$ ( $\mu\text{b}/\text{GeV}^2$ )	No. $K(1420)$ events	Corrected $d\sigma/dt'$ ( $\mu\text{b}/\text{GeV}^2$ )
0.00–0.05	224 ± 23	1641 ± 168	102 ± 27	1339 ± 354
0.05–0.10	157 ± 27	1150 ± 198	62 ± 14	814 ± 184
0.10–0.20	160 ± 17	586 ± 62	101 ± 16	663 ± 105
0.20–0.30	100 ± 22	366 ± 81	68 ± 12	446 ± 79
0.30–0.50	95 ± 21	174 ± 38	63 ± 12	207 ± 39
0.50–1.00	99 ± 19	73 ± 14	53 ± 13	70 ± 17
1.00–2.00	65 ± 18	24 ± 7	23 ± 6	15 ± 4

3.2. Charged  $K(1420)$ 

For cross-section estimates we again consider only the  $(K\pi)^-$  decay mode. The three final states (reactions 2, 3, 5) were combined in all subsequent analyses so as to improve the statistical quality of the data. As previously mentioned, a scanning selection was imposed on the proton length in the two-prong topology; however,  $t'_{\min}$  considerations indicated that this cut barely affects the  $K(1420)$  region. Furthermore, several checks including  $\chi^2$  compatibility tests on  $|t'|$  distributions and investigation of relevant decay correlations showed there to be no significant difference between resonance features in the two-prong and two-prong-plus-vee topologies. After correction for probability cuts and  $\bar{K}^0$  visibility (where needed), total  $K(1420)$  cross sections for each of the three reactions were obtained.<sup>31</sup> Good agreement was found for the three cross sections, and an average microbarn equivalent was calculated which was used for the remainder of this study.

The  $K^-p \rightarrow K(1420)^-p$  differential cross sections were obtained in the manner indicated above and are shown in Fig. 59. Pertinent details, including the relevant parameters obtained from fits to these distributions, are given in Tables XXII and XXIII.

The total cross sections for the reaction



for the two momenta were measured to be

$$3.9 \text{ GeV}/c: \sigma = 186 \pm 14 \mu\text{b},$$

$$4.6 \text{ GeV}/c: \sigma = 140 \pm 15 \mu\text{b}.$$

Table XXIV presents a summary of the results of the measurement of the cross sections for the negatively charged  $K(1420)$ .

In conclusion, the  $K(1420)^0$  is produced with a cross section  $\sim 2$  times larger than its negatively charged partner at 3.9 and 4.6 GeV/c. In addition, as was found in our study of  $K(890)$  production, the differential cross section of the neutral mode has a larger slope than that of the negatively charged resonance. These differences indicate different production mechanisms for the two final states. A more detailed analysis would require the knowledge of the corresponding density-matrix elements; however, because of interference effects in the decay angular distribution in a large fraction of the data, these quantities are difficult to obtain. We discuss this more fully in the next section.

TABLE XX. Slope parameters for  $K(1420)^0$  production.

Momentum (GeV/c)	Form fitted $ t' $ interval (GeV <sup>2</sup> )	$e^{bt'}$		$e^{bt'+ct'^2}$		
		$b$	$P_{\chi^2}$ (%)	$b$	$c$	$P_{\chi^2}$ (%)
3.9	0.00–0.50	6.5 ± 0.8	24			
	0.00–1.00	4.9 ± 0.5	0.007	8.5 ± 0.3	5.4 ± 0.4	75
	0.00–2.00	4.5 ± 0.5	0.004	6.6 ± 0.2	2.4 ± 0.1	21
4.6	0.00–0.50	4.6 ± 0.8	84			
	0.00–1.00	4.2 ± 0.6	81	5.2 ± 1.4	1.4 ± 1.8	80
	0.00–2.00	3.6 ± 0.4	19	5.2 ± 0.8	1.4 ± 0.5	91

TABLE XXI. Cross sections for  $K(1420)^0$  production.

Reaction	Momentum	3.9 GeV/c		4.6 GeV/c	
		No. $K(1420)$ events	Corrected $\sigma$ ( $\mu\text{b}$ )	No. $K(1420)$ events	Corrected $\sigma$ ( $\mu\text{b}$ )
$K^-p \rightarrow K(1420)^0 n$ $\swarrow$ $(K\pi)^0$		926 $\pm$ 108	340 $\pm$ 40	489 $\pm$ 37	321 $\pm$ 24
$K^-p \rightarrow K(1420)^0 n$			570 $\pm$ 108		540 $\pm$ 90

#### 4. Spin Parity

In this section we present a spin-parity analysis of the  $K(1420)$ . Based on SU(3) analyses, it has always seemed natural to assign this meson to the  $2^+$  nonet; unfortunately, experiments have provided only weak support for this assignment, with  $3^-$  (and, in some sense,  $1^-$ ) not being ruled out. The large statistics of the present experiment would seem sufficient to establish finally the spin-parity of this meson; however, a large fraction of the  $K(1420)$  events cannot be used for a spin-parity test because of observed negative and therefore unphysical values for some diagonal elements of the resonance density matrix. A careful search revealed, however, that a selected sample of non-peripheral events in the charged mode, in which this problem was not present, provided sufficient data to favor strongly  $2^+$  over  $1^-$ . In addition, if simple assumptions are made on the  $K(1420)$  production mechanism, the  $3^-$  hypothesis is also ruled out.

##### 4.1. Method

Our approach made use of the connection between the production mechanism and the decay correlations of a resonance.<sup>32</sup> For a resonance  $\bar{d}$  (with spin  $J$ ) decaying into two particles  $\bar{a}$ ,  $\bar{b}$  (with spins  $j_a$ ,  $j_b$ ) the angular distribution of the decay is of the form

$$W^J(\theta, \phi) = N'' \sum_{\lambda_a \lambda_b m m'} |M_d(\lambda_a, \lambda_b)|^2 \times \exp[i(m - m')\phi] d_{m\Lambda}^J(\theta) d_{m'\Lambda}^J(\theta) \rho_{mm'},$$

where  $\lambda_a$ ,  $\lambda_b$ , and  $\Lambda$  are the helicities of particles  $\bar{a}$  and  $\bar{b}$  and their difference, respectively;  $\theta$ ,  $\phi$  are the polar and azimuthal angles of  $\bar{a}$  in the Gottfried-Jackson frame, and  $\rho_{mm'}$  are the density-matrix elements in this frame. For the case of  $\bar{a}$  and  $\bar{b}$  spinless (or  $j_a = 1$  and  $j_b = 0$  if  $J^P = 1^-, 2^+, 3^-$ ), reflection invariance reduces to one the number of  $M_d$  constants, so that  $W(\theta, \phi)$  can be expressed directly in terms of  $\rho_{mm'}$ . Detailed forms of  $W(\theta, \phi)$  for different  $J^P$  can be found elsewhere.<sup>33</sup> This formulation of the decay correlations assumes free production of resonances (i.e., no interference effects with other different processes) and leads to positive values for all diagonal elements of the density matrix. Nonphysical values of these parameters reflect the inadequacy of the free decay hypothesis and make this simple approach for the  $J^P$  determination meaningless.

Our method consisted of determining the density-matrix elements by fitting  $W(\theta, \phi)$  [for each particular  $K(1420)$  spin-parity hypothesis  $1^-, 2^+, 3^-$ ] to the two-body experimental decay distributions.<sup>34</sup> The quality (as measured by a  $\chi^2$ -probability test) of the fits from different theoretical predictions, corresponding to different  $J^P$ , was used to decide among the possible spin-parity assignments.

We now proceed to outline the maximum-likelihood technique employed in the analysis of the two-body decay samples. For the  $K(1420)$  region, as defined by  $1.32 \leq m_{K\pi} \leq 1.52$  GeV, we write the following likelihood function:

$$\mathcal{L} = \prod_{i=1, N} W(\theta, \phi),$$

where  $N$  is the number of events in this region and  $W(\theta, \phi)$  is the expression for the decay angular distribution, which we write as

$$W(\theta, \phi) = \epsilon W_R^J(\theta, \phi) + (1 - \epsilon) W_B(\theta, \phi),$$

where  $\epsilon$  is the fraction of resonance events in the  $K(1420)$  region, which was obtained from fits to the  $K\pi$  effective-mass spectrum utilizing an incoherent superposition of a Breit-Wigner form and a poly-

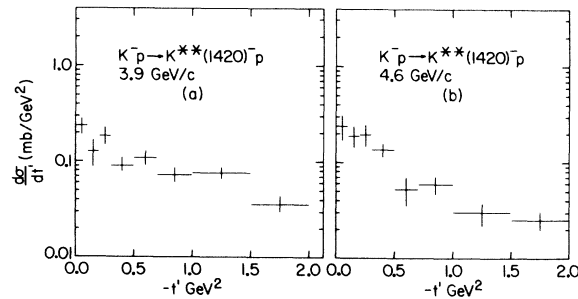


FIG. 59. Differential cross section for reaction  $K^-p \rightarrow K(1420)^0 p$ : (a) at 3.9 GeV/c; (b) at 4.6 GeV/c.

TABLE XXII. Differential cross sections for reaction  $K^-p \rightarrow K(1420)^-p \rightarrow (K\pi)^-p$  at 3.9 and 4.6 GeV/c.

$ t' $ interval (GeV <sup>2</sup> )	3.9 GeV/c		4.6 GeV/c	
	No. $K(1420)$ events	Corrected $d\sigma/dt'$ ( $\mu\text{b}/\text{GeV}^2$ )	No. $K(1420)$ events	Corrected $d\sigma/dt'$ ( $\mu\text{b}/\text{GeV}^2$ )
0.00–0.10	107 ± 21	238 ± 47	82 ± 24	238 ± 70
0.10–0.20	57 ± 18	127 ± 40	65 ± 16	188 ± 46
0.20–0.30	84 ± 18	187 ± 40	67 ± 17	194 ± 49
0.30–0.50	81 ± 19	90 ± 21	93 ± 16	135 ± 23
0.50–0.70	98 ± 16	109 ± 18	36 ± 12	52 ± 17
0.70–1.00	98 ± 17	73 ± 13	61 ± 13	59 ± 13
1.00–1.50	171 ± 22	76 ± 10	52 ± 13	30 ± 8
1.50–2.00	80 ± 14	36 ± 6	43 ± 10	25 ± 6

nomial background.  $W_R^J(\theta, \phi)$  is the theoretical expression for the decay distribution of a resonance with spin parity  $J^P$ , and  $W_B(\theta, \phi)$  represents the analogous form for the background events. A suitable (but by no means unique) parametrization of  $W_B(\theta, \phi)$  was obtained by considering a linear combination of spherical harmonics:

$$W_B(\theta, \phi) = a_i^m \text{Re} Y_i^m(\theta, \phi).$$

The coefficients  $a_i^m$  in this expansion were obtained by calculating the pertinent  $\text{Re} Y_i^m(\theta, \phi)$  moments using the events in the adjacent regions  $1.22 \leq m_{K\pi} \leq 1.32$  GeV and  $1.52 \leq m_{K\pi} \leq 1.62$  GeV. All moments found to have greater than 3-standard-deviation significance were included (moments up to order eight were calculated) in this expansion.

For the study of the momentum-transfer behavior of the density-matrix elements where these lesser statistical samples did not warrant a more complete treatment (i.e., including correlations), the  $\cos\theta$  and  $\phi$  distributions were fitted separately. A similar maximum-likelihood technique was used, as described above. A suitable parametrization for the background angular distributions was obtained with a Legendre polynomial expansion in which the coefficients were obtained by fits to the  $\cos\theta$  and  $\phi$  distributions for events in the control regions.

Again the order of the series was determined by observing the goodness of the pertinent fits.

We note that, since the errors on the coefficients in the expansion of the background angular distribution have not yet been propagated in our likelihood technique, the corresponding errors on the resonance density-matrix elements (in particular, the values of the nondiagonal elements determined as a function of  $-t'$ ) are underestimated.

#### 4.2. Results

We now present the detailed results of the analysis on the neutral and charged modes of the  $K(1420)$ . The data at 3.9 and 4.6 GeV/c have been combined for the remainder of the discussion.

*4.2.1. Neutral  $K(1420)$ .* The complete momentum-transfer region ( $0.0 \leq |t'| \leq 2.0$  GeV<sup>2</sup>) for  $K(1420)$  production, which includes  $\sim 1000$  resonance events in the region of interest, was used in a first attempt to obtain information on the  $J^P$  assignment. The values of the density-matrix elements (for each particular hypothesis) are presented in Table XXV. In Fig. 60 are displayed the Jackson and Treiman-Yang distributions for the events in the  $K(1420)$  region together with the best-fit predictions for each  $J^P$  hypothesis.

TABLE XXIII. Slope parameters for  $K(1420)^-$  production.

Momentum (GeV/c)	Form fitted $ t' $ interval (GeV <sup>2</sup> )	$e^{bt'}$		$e^{bt'+ct'^2}$		
		$b$	$P_{\chi^2}$	$b$	$c$	$P_{\chi^2}$
3.9	0.00–0.50	2.4 ± 0.9	20			
	0.00–1.00	1.2 ± 0.3	20	2.3 ± 1.3	1.1 ± 1.3	17
	0.00–2.00	0.9 ± 0.1	9	1.0 ± 0.5	0.1 ± 0.2	5
4.6	0.00–0.50	1.6 ± 0.8	87			
	0.00–1.00	2.1 ± 0.4	41	2.8 ± 1.4	0.8 ± 1.6	27
	0.00–2.00	1.5 ± 0.2	17	2.7 ± 0.6	0.7 ± 0.3	55

TABLE XXIV. Cross sections for  $K(1420)^-$  production.

Reaction	Momentum	3.9 GeV/c		4.6 GeV/c	
		No. $K(1420)$ events	Corrected $\sigma$ ( $\mu\text{b}$ )	No. $K(1420)$ events	Corrected $\sigma$ ( $\mu\text{b}$ )
$K^- p \rightarrow K(1420)^- \bar{p}$ $\swarrow$ $(K\pi)^-$		837 $\pm$ 65	186 $\pm$ 14	483 $\pm$ 53	140 $\pm$ 15
$K^- p \rightarrow K(1420)^- \bar{p}$			312 $\pm$ 13		235 $\pm$ 29

We observe that the  $J^P = 1^-$  assignment gives a very poor description of the experimental  $\cos\theta$  distribution ( $P_{\chi^2} \approx 10^{-4}\%$ ). The hypotheses  $2^+$  and  $3^-$  lead to comparably good representations of the data, but give significantly large and negative values of  $\rho_{22}$  and  $\rho_{33}$ , respectively.<sup>35</sup>

As previously pointed out, unphysical values of the diagonal density-matrix elements reflect the presence of other processes interfering with  $K(1420)$  production. In Sec. IV we observed a very striking forward-backward asymmetry in the  $K(890)^0$  Jackson decay angular distribution which we interpreted as being caused by an  $S$ -wave  $K\pi$  interaction interfering with the  $K(890)$   $P$  wave. Our results, here, suggest that some  $0^+$   $K\pi$  component is still present in the region of the  $K(1420)$  meson. Since it is difficult to estimate the amount of  $S$  wave in this region and, moreover, a simple pa-

rametrization of the decay distributions of an interfering system composed of  $S$  and  $D$  (or  $F$ ) waves does not provide information on the density-matrix elements of the  $K(1420)$ , we are forced to investigate more favorable situations in which interference effects of this type are not present. The natural procedure is to study the behavior of the density-matrix elements as a function of the momentum transfer  $|t'|$ . Utilizing the Jackson and Treiman-Yang angular distributions independently, the  $|t'|$  dependence of some density-matrix elements was obtained for a  $2^+$  hypothesis. Figure 61 and Table XXVI display these results. We observe that, in the region  $|t'| < 0.5 \text{ GeV}^2$ ,  $\rho_{22}$  is negative and large, while for  $|t'| > 0.5 \text{ GeV}^2$ , values consistent with the physical range of  $\rho_{22}$  were found. This result should be expected if, as we suggest, the special behavior of  $\rho_{22}$  is due to the presence of an

TABLE XXV. Density-matrix elements of the  $K(1420)^0$  produced in the reaction  $K^- p \rightarrow K^- \pi^+ n$ .

$ t' $ interval	0.00–2.00 $\text{GeV}^2$	
Mass region	1.32–1.52 $\text{GeV}$	
Events	1961	
Resonance events	973	
$J^P = 1^-$	$\rho_{00} = 0.96 \pm 0.03$ $\rho_{11} = 0.02 \pm 0.03$	$\rho_{1-1} = -0.01 \pm 0.02$ $\text{Re}\rho_{10} = -0.07 \pm 0.02$
$J^P = 2^+$	$\rho_{00} = 0.86 \pm 0.03$ $\rho_{11} = 0.30 \pm 0.02$ $\rho_{22} = -0.23 \pm 0.02$	$\rho_{1-1} = 0.02 \pm 0.03$ $\rho_{2-2} = 0.00 \pm 0.02$ $\text{Re}\rho_{21} = -0.06 \pm 0.02$ $\text{Re}\rho_{10} = -0.05 \pm 0.02$ $\text{Re}\rho_{20} = -0.01 \pm 0.01$ $\text{Re}\rho_{2-1} = 0.02 \pm 0.01$
$J^P = 3^-$	$\rho_{00} = 0.58 \pm 0.04$ $\rho_{11} = 0.42 \pm 0.02$ $\rho_{22} = -0.01 \pm 0.02$ $\rho_{33} = -0.20 \pm 0.02$	$\rho_{1-1} = -0.01 \pm 0.03$ $\rho_{2-2} = 0.03 \pm 0.02$ $\rho_{3-3} = 0.02 \pm 0.02$ $\text{Re}\rho_{10} = -0.01 \pm 0.02$ $\text{Re}\rho_{20} = 0.01 \pm 0.01$ $\text{Re}\rho_{30} = 0.01 \pm 0.01$ $\text{Re}\rho_{21} = -0.06 \pm 0.02$ $\text{Re}\rho_{2-1} = 0.02 \pm 0.02$ $\text{Re}\rho_{31} = -0.01 \pm 0.02$ $\text{Re}\rho_{3-1} = -0.01 \pm 0.02$ $\text{Re}\rho_{32} = -0.04 \pm 0.01$ $\text{Re}\rho_{3-2} = 0.01 \pm 0.01$

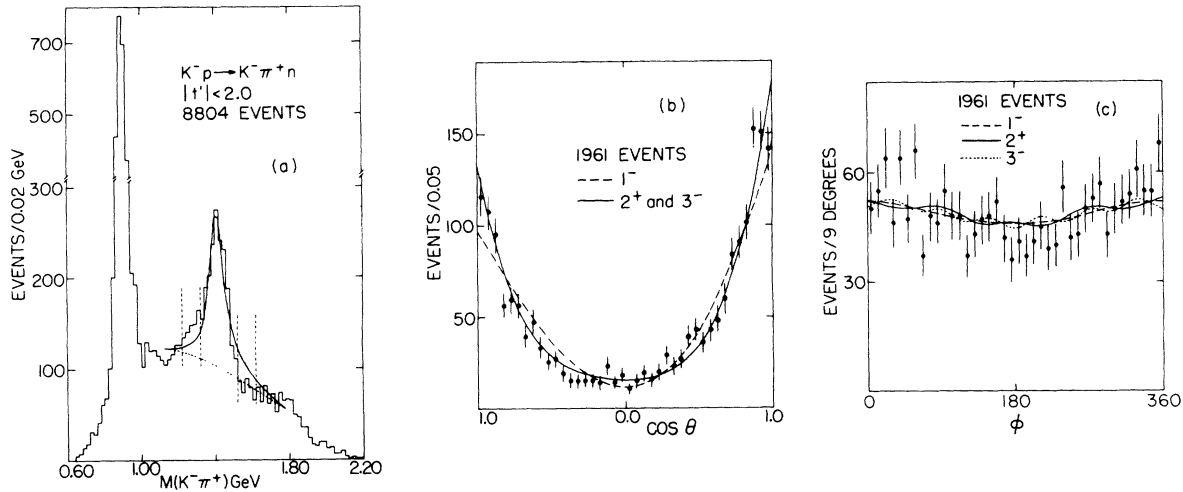


FIG. 60. (a)  $K^-\pi^+$  effective-mass distribution for reaction  $K^-p \rightarrow K^-\pi^+n$  in the momentum-transfer interval  $|t'| < 2.0$   $\text{GeV}^2$ . The solid curve is the result of the fit described in the text, and the dotted line is the calculated background. The vertical dotted lines define the resonance and background regions. (b), (c) Jackson and Treiman-Yang decay angular distribution for events in the region  $1.32 \leq M(K^-\pi^+) \leq 1.52$   $\text{GeV}$ . The curves are the predictions of various  $J^P$  hypotheses and are described in the text.

$S$ -wave  $K\pi$  interaction which, as we have seen in the  $K^*(890)$  analysis, is almost entirely contained in the forward  $|t'|$  region (see Fig. 31).

The peripheral production properties of the  $K(1420)^0$  led to a small sample of events in the region  $|t'| > 0.5$   $\text{GeV}^2$  which was insufficient to make conclusive statements on the spin parity of the  $K(1420)$ . Table XXVII and Fig. 62 show the results obtained in this momentum-transfer region. The  $1^-$ ,  $2^+$ , and  $3^-$  hypotheses give identical predictions for the Jackson and Treiman-Yang angular distributions.

In summary, no information could be obtained from the neutral mode, since interference effects combined with the peripheral characteristics of the  $K(1420)^0$  production reduced the available sample of events by a large factor.

4.2.2. *Charged  $K(1420)$ .* A similar approach was followed for the negatively charged  $K(1420)$ . The

results obtained from the entire  $(K\pi)^-$  sample [ $\sim 1000$  resonance events in the region  $1.32 \leq m_{(K\pi)^-} \leq 1.52$   $\text{GeV}$  and  $|t'| < 2.0$   $\text{GeV}^2$ ] are displayed in Table XXVIII and Fig. 63. Again, anomalous values for  $\rho_{22}$  and  $\rho_{33}$  were found, similar to those observed in the neutral mode. Moreover, the three hypotheses gave equally good fits to the Jackson angular distribution; however, all gave very low-probability descriptions of the Treiman-Yang angular distribution.

The investigation of the momentum-transfer dependence of the density-matrix elements (see Table XXIX and Fig. 64) revealed normal behavior of  $\rho_{22}$  in the region  $|t'| > 0.3$   $\text{GeV}^2$ ; however, because of the better signal-to-noise ratio, only events in the momentum-transfer region  $0.5 \leq |t'| \leq 2.0$   $\text{GeV}^2$  were considered. The less peripheral production properties of the  $K(1420)$ , in the non-charge-exchange reaction, afforded a good statis-

TABLE XXVI. Density-matrix elements for the  $K(1420)^0$ .

$ t' $ interval ( $\text{GeV}^2$ )	No. events <sup>a</sup>	No. $K(1420)$ events <sup>a</sup>	Probabilities (%)							
			$\rho_{00}$	$\rho_{11}$	$\rho_{22}$	$\rho_{1-1}$	$\rho_{2-2}$	$\text{Re}\rho_{20}$	$\cos\theta$ $\phi$	
0.00-0.05	492	236	$1.02 \pm 0.06$	$0.33 \pm 0.04$	$-0.34 \pm 0.05$	$0.08 \pm 0.12$	$-0.14 \pm 0.08$	$0.00 \pm 0.08$	6	67
0.05-0.10	297	175	$0.68 \pm 0.06$	$0.34 \pm 0.04$	$-0.18 \pm 0.04$	$-0.03 \pm 0.14$	$0.09 \pm 0.10$	$0.00 \pm 0.20$	47	74
0.10-0.20	360	176	$0.94 \pm 0.06$	$0.25 \pm 0.04$	$-0.22 \pm 0.04$	$-0.07 \pm 0.15$	$0.10 \pm 0.10$	$0.00 \pm 0.19$	1	23
0.20-0.30	220	128	$0.86 \pm 0.06$	$0.30 \pm 0.04$	$-0.23 \pm 0.05$	$0.06 \pm 0.15$	$0.10 \pm 0.14$	$0.00 \pm 0.18$	11	99
0.30-0.50	207	116	$0.82 \pm 0.06$	$0.36 \pm 0.05$	$-0.27 \pm 0.04$	$-0.20 \pm 0.16$	$-0.14 \pm 0.14$	$0.00 \pm 0.20$	32	13
0.50-1.00	218	120	$0.40 \pm 0.08$	$0.36 \pm 0.05$	$-0.05 \pm 0.06$	$-0.18 \pm 0.16$	$0.00 \pm 0.14$	$0.00 \pm 0.18$	7	75
1.00-2.00	167	63	$0.40 \pm 0.08$	$0.28 \pm 0.09$	$0.02 \pm 0.09$	$0.24 \pm 0.20$	$-0.15 \pm 0.24$	$0.13 \pm 0.16$	15	29

<sup>a</sup> Events in the region  $1.32 \leq M(K^-\pi^+) \leq 1.52$   $\text{GeV}$ .

TABLE XXVII. Density matrix of the  $K(1420)^0$  produced in the reaction  $K^-p \rightarrow K^- \pi^+ n$ .

$ t' $ interval		0.5–2.00 GeV <sup>2</sup>
Mass region		1.32–1.52 GeV
Events		385
Resonance events		135
$J^P = 1^-$	$\rho_{00} = 0.84 \pm 0.10$	$\rho_{1-1} = 0.05 \pm 0.08$
	$\rho_{11} = 0.08 \pm 0.10$	$\text{Re}\rho_{10} = -0.08 \pm 0.07$
$J^P = 2^+$	$\rho_{00} = 0.46 \pm 0.07$	$\rho_{1-1} = -0.02 \pm 0.09$
	$\rho_{11} = 0.36 \pm 0.04$	$\rho_{2-2} = 0.04 \pm 0.08$
	$\rho_{22} = -0.09 \pm 0.06$	$\text{Re}\rho_{21} = -0.07 \pm 0.06$
		$\text{Re}\rho_{10} = -0.02 \pm 0.07$
		$\text{Re}\rho_{20} = 0.05 \pm 0.04$
		$\text{Re}\rho_{2-1} = 0.11 \pm 0.07$
$J^P = 3^-$	$\rho_{00} = 0.24 \pm 0.11$	$\rho_{1-1} = 0.00 \pm 0.08$
	$\rho_{11} = 0.35 \pm 0.06$	$\rho_{2-2} = 0.06 \pm 0.09$
	$\rho_{22} = 0.17 \pm 0.07$	$\rho_{3-3} = 0.05 \pm 0.06$
	$\rho_{33} = -0.14 \pm 0.06$	$\text{Re}\rho_{10} = 0.01 \pm 0.06$
		$\text{Re}\rho_{20} = -0.02 \pm 0.04$
		$\text{Re}\rho_{30} = 0.10 \pm 0.05$
		$\text{Re}\rho_{21} = -0.05 \pm 0.06$
		$\text{Re}\rho_{2-1} = 0.07 \pm 0.07$
		$\text{Re}\rho_{31} = 0.05 \pm 0.04$
		$\text{Re}\rho_{3-1} = 0.01 \pm 0.06$
	$\text{Re}\rho_{32} = -0.06 \pm 0.05$	
	$\text{Re}\rho_{3-2} = -0.08 \pm 0.04$	

TABLE XXVIII. Density-matrix elements of the  $K(1420)^-$  produced in the reaction  $K^-p \rightarrow (K\pi)p$ .

$ t' $ interval		0.00–2.00 GeV <sup>2</sup>
Mass region		1.32–1.52 GeV
Events		2304
Resonance events		961
$J^P = 1^-$	$\rho_{00} = 0.76 \pm 0.04$	$\rho_{1-1} = 0.11 \pm 0.03$
	$\rho_{11} = 0.12 \pm 0.04$	$\text{Re}\rho_{10} = -0.16 \pm 0.02$
$J^P = 2^+$	$\rho_{00} = 0.44 \pm 0.03$	$\rho_{1-1} = 0.13 \pm 0.03$
	$\rho_{11} = 0.33 \pm 0.02$	$\rho_{2-2} = -0.06 \pm 0.02$
	$\rho_{22} = -0.05 \pm 0.02$	$\text{Re}\rho_{21} = -0.13 \pm 0.02$
		$\text{Re}\rho_{10} = -0.04 \pm 0.02$
		$\text{Re}\rho_{20} = 0.04 \pm 0.01$
		$\text{Re}\rho_{2-1} = -0.05 \pm 0.03$
$J^P = 3^-$	$\rho_{00} = 0.42 \pm 0.04$	$\rho_{1-1} = 0.10 \pm 0.03$
	$\rho_{11} = 0.31 \pm 0.02$	$\rho_{2-2} = -0.11 \pm 0.03$
	$\rho_{22} = 0.17 \pm 0.03$	$\rho_{3-3} = 0.01 \pm 0.02$
	$\rho_{33} = -0.19 \pm 0.02$	$\text{Re}\rho_{10} = -0.01 \pm 0.02$
		$\text{Re}\rho_{20} = 0.06 \pm 0.02$
		$\text{Re}\rho_{30} = -0.05 \pm 0.02$
		$\text{Re}\rho_{21} = -0.05 \pm 0.02$
		$\text{Re}\rho_{2-1} = -0.06 \pm 0.02$
		$\text{Re}\rho_{31} = -0.01 \pm 0.02$
		$\text{Re}\rho_{3-1} = 0.00 \pm 0.02$
	$\text{Re}\rho_{32} = -0.09 \pm 0.02$	
	$\text{Re}\rho_{3-2} = 0.01 \pm 0.02$	

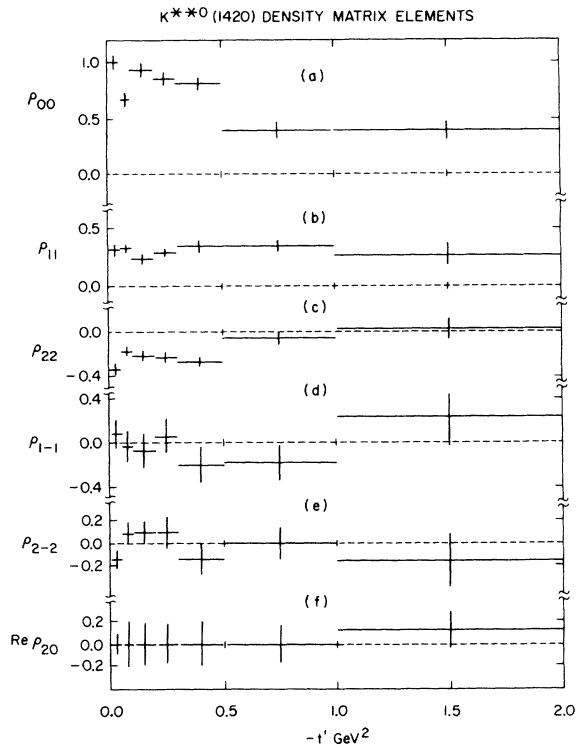


FIG. 61. Density-matrix elements of the  $K(1420)^0$  in the Gottfried-Jackson frame as a function of momentum transfer.

tical sample in this nonforward region. The results of a complete analysis, which included polar-azimuthal correlations, are displayed in Fig. 65 and Tables XXX and XXXI. A striking change in the form of the Jackson angular distribution is observed, once this momentum-transfer selection has been imposed [compare Fig. 65(b) with Fig.

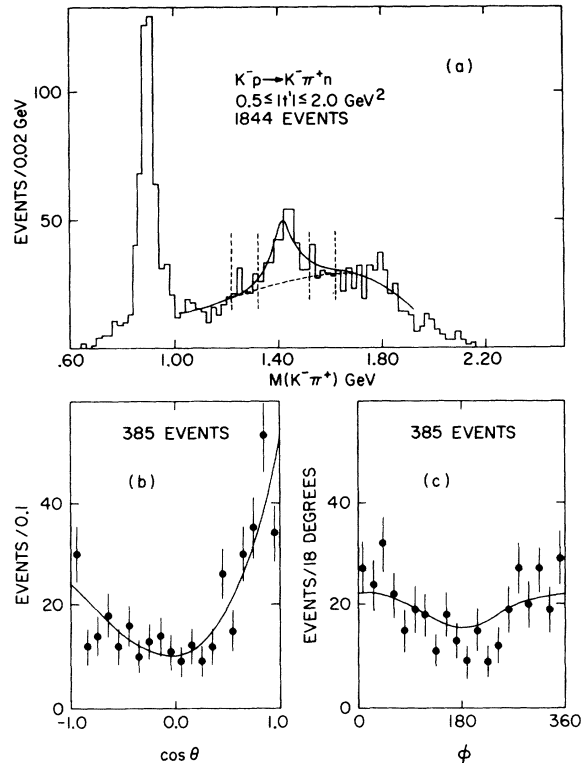


FIG. 62. Same as Fig. 60 but the momentum-transfer region considered is  $0.5 \leq |t'| \leq 2.0 \text{ GeV}^2$ .

63(b)], with a significant depopulation of events observed in the forward and backward regions of  $\cos\theta$  which cannot be described by the  $J^P = 1^-$  spin-parity assignment. We also note that none of the three hypotheses gave an entirely satisfactory description of the Treiman-Yang angular distribution, which may reflect some inadequacy in some of the

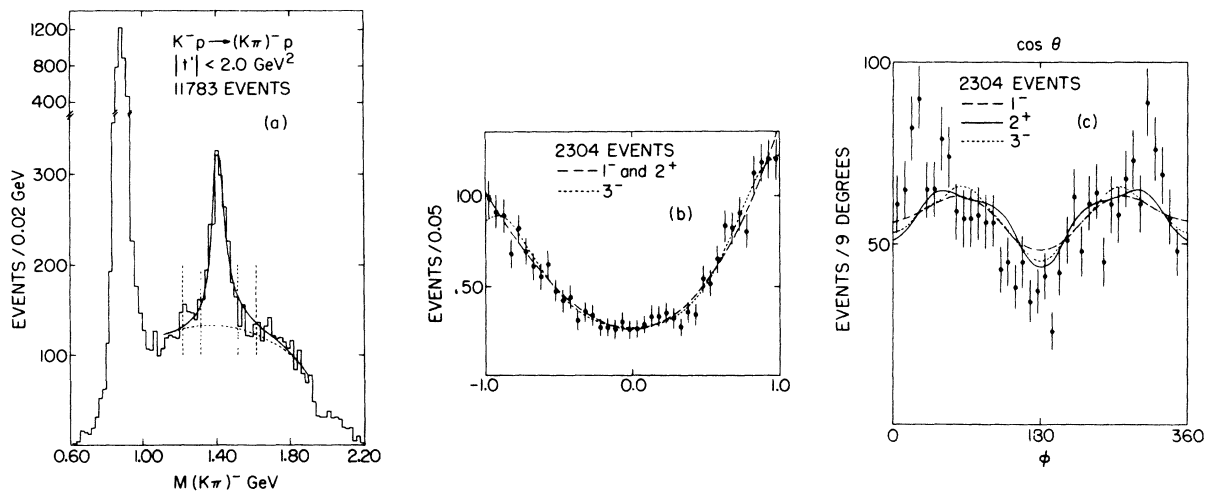


FIG. 63. Same as Fig. 60 but for the reaction  $K^-p \rightarrow (K\pi)^-p$  in the momentum-transfer region  $|t'| < 2.0 \text{ GeV}^2$ .

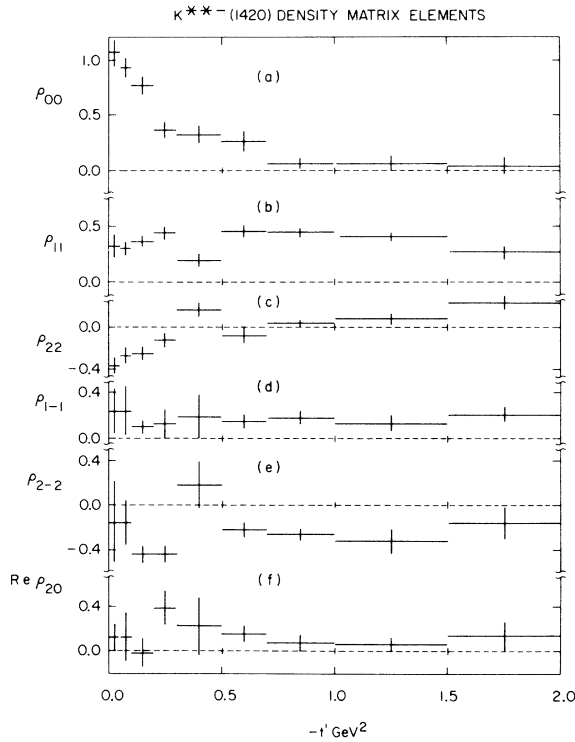


FIG. 64. Density-matrix elements of the  $K(1420)^-$  in the Gottfried-Jackson frame as a function of momentum transfer.

assumptions used. In particular, since our parametrization does not adequately reproduce the azimuthal distribution for the background (see Fig. 66), the quoted  $\chi^2$  probabilities should be considered with some caution.

In order to avoid the problems associated with the parametrization of the background, a different approach was tried. This method ignored  $\cos\theta-\phi$  correlations and employed a  $\chi^2$  fit on the background-subtracted  $\cos\theta$  and  $\phi$  distributions. The results of the fits to these distributions are shown in Figs. 67(a) and 67(b) and Table XXXII. We note that this method provided acceptable descriptions of the  $\phi$  distribution. A comparison of the relative goodness of the three fits to the  $\cos\theta$  distribution rules out the  $1^-$  hypotheses (as did the approach described above). We further made the dynamical assumption that  $t$ -channel exchanges with  $J > 1$  were not present (i.e.,  $\rho_{mm'} = 0$  for  $m, m' \geq 2$ ), and refit the pertinent distributions with a reduced form of the decay angular distribution for the  $J^P = 2^+$  and  $3^-$  hypotheses. The results of the fits, as shown in Figs. 67(c), 67(d) and listed in parentheses in Table XXXII, ruled out the  $3^-$  hypothesis. We then conclude that this sample of events strongly favors the traditionally accepted  $2^+$  spin-parity assignment for the  $K(1420)$  meson.

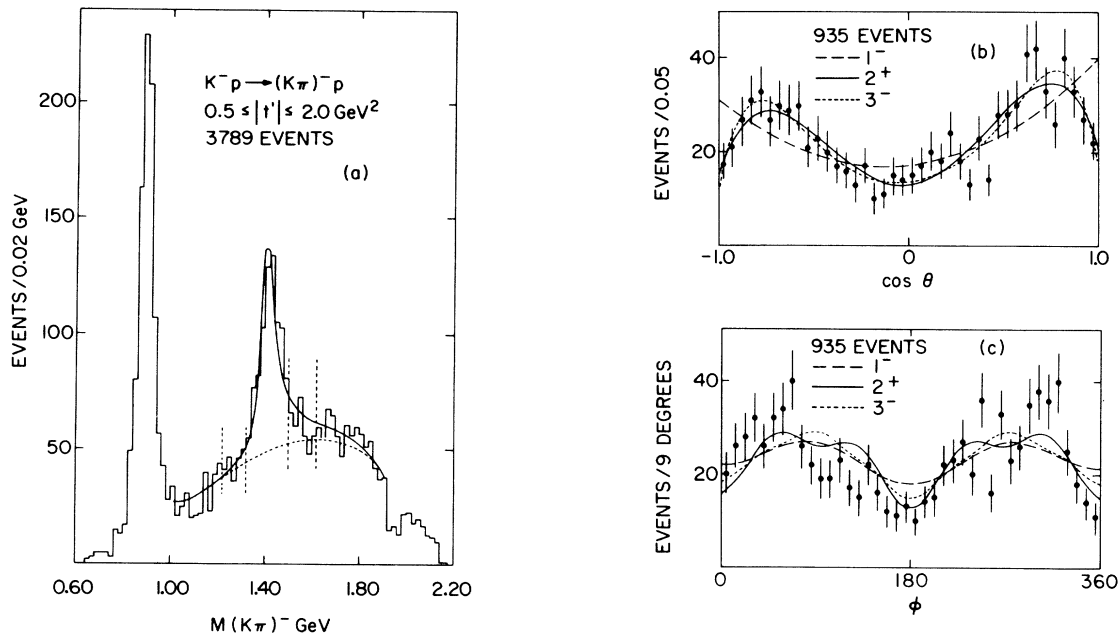


FIG. 65. Same as Fig. 63 but the momentum transfer considered is  $0.5 \leq |t'| \leq 2.0 \text{ GeV}^2$ .

TABLE XXIX. Density-matrix elements for the  $K(1420)^-$ .

$ t' $ interval (GeV <sup>2</sup> )	No. events <sup>a</sup>	No. $K(1420)$ events <sup>a</sup>	$\rho_{00}$	$\rho_{11}$	$\rho_{22}$	$\rho_{1-1}$	$\rho_{2-2}$	$\text{Re}\rho_{20}$	Probability (%)	$\phi$
0.00-0.05	276	66	1.06±0.12	0.32±0.10	-0.35±0.07	0.24±0.20	-0.15±0.36	0.13±0.15	1	2
0.05-0.10	244	90	0.92±0.09	0.30±0.06	-0.26±0.07	0.24±0.22	-0.15±0.20	0.13±0.22	99	3
0.10-0.20	307	117	0.76±0.08	0.36±0.05	-0.24±0.06	0.10±0.06	-0.44±0.08	-0.01±0.13	25	1
0.20-0.30	233	105	0.36±0.08	0.44±0.06	-0.12±0.05	0.13±0.12	-0.44±0.08	0.39±0.15	23	7
0.30-0.50	309	130	0.32±0.08	0.19±0.06	0.15±0.06	0.19±0.20	0.18±0.21	0.23±0.26	34	1
0.50-0.70	217	104	0.26±0.09	0.45±0.06	-0.08±0.07	0.15±0.06	-0.22±0.06	0.16±0.07	11	15
0.70-1.00	245	115	0.06±0.05	0.44±0.04	0.03±0.02	0.18±0.06	-0.26±0.05	0.08±0.07	78	85
1.00-1.50	292	175	0.06±0.06	0.40±0.04	0.07±0.04	0.13±0.07	-0.32±0.11	0.07±0.05	52	3
1.50-2.00	181	98	0.04±0.08	0.27±0.06	0.21±0.06	0.21±0.07	-0.16±0.13	0.14±0.13	78	17

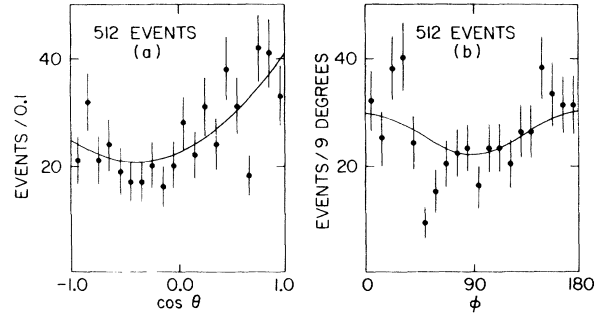
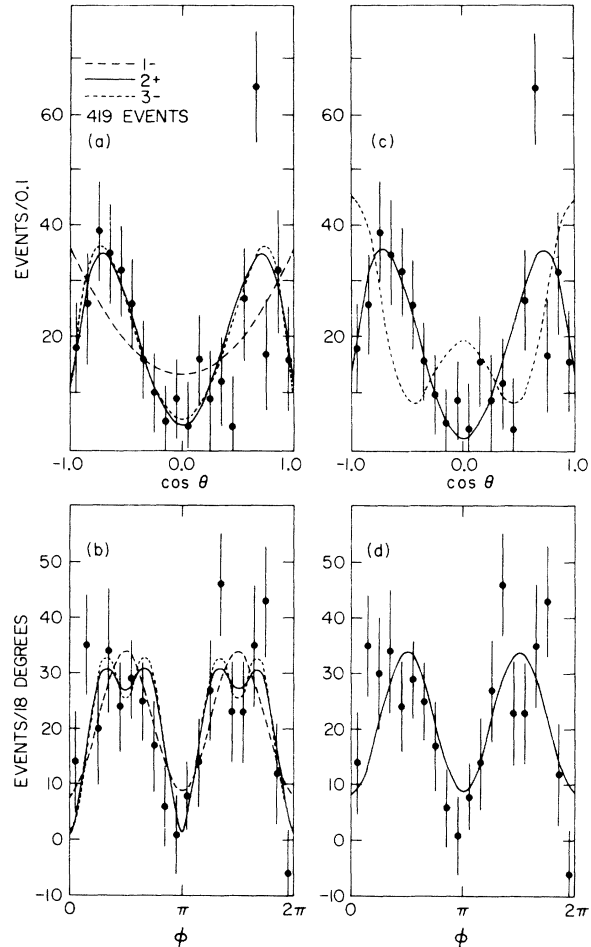
<sup>a</sup> Events in the region  $1.32 \leq M(K\pi)^- \leq 1.52$  GeV.FIG. 66. Jackson and Treiman-Yang angular distribution for events in control regions [ $1.22 \leq M(K\pi)^- \leq 1.32$  GeV and  $1.52 \leq M(K\pi)^- \leq 1.62$  GeV] for reaction  $K^- \bar{p} \rightarrow (K\pi)^- \bar{p}$  in the momentum-transfer interval  $0.5 \leq |t'| \leq 2.0$  GeV<sup>2</sup>.FIG. 67. (a), (b) Subtracted Jackson and Treiman-Yang decay angular distributions of the  $K(1420)^-$  in the momentum-transfer region  $0.5 \leq |t'| \leq 2.0$  GeV<sup>2</sup>. (c), (d) Same as (a), (b) but the curves correspond to a simplified assumption on the production mechanism (only exchanged particles with  $J \leq 1$  are allowed).

TABLE XXX. Density-matrix elements of the  $K(1420)^-$  produced in the reaction  $K^-p \rightarrow (K\pi)^-p$ .

$ t' $ interval	0.50–2.00 GeV <sup>2</sup>	
Mass region	1.32–1.52 GeV	
Events	935	
Resonance events	419	
$J^P = 1^-$	$\rho_{00} = 0.62 \pm 0.06$ $\rho_{11} = 0.19 \pm 0.06$	$\rho_{1-1} = 0.16 \pm 0.05$ $\text{Re}\rho_{10} = -0.20 \pm 0.03$
$J^P = 2^+$	$\rho_{00} = 0.06 \pm 0.03$ $\rho_{11} = 0.44 \pm 0.02$ $\rho_{22} = 0.03 \pm 0.02$	$\rho_{1-1} = 0.26 \pm 0.04$ $\rho_{2-2} = -0.15 \pm 0.04$ $\text{Re}\rho_{21} = -0.18 \pm 0.03$ $\text{Re}\rho_{10} = -0.07 \pm 0.03$ $\text{Re}\rho_{20} = 0.02 \pm 0.02$ $\text{Re}\rho_{2-1} = -0.11 \pm 0.03$
$J^P = 3^-$	$\rho_{00} = -0.06 \pm 0.05$ $\rho_{11} = 0.24 \pm 0.03$ $\rho_{22} = 0.37 \pm 0.03$ $\rho_{33} = -0.08 \pm 0.03$	$\rho_{1-1} = 0.23 \pm 0.04$ $\rho_{2-2} = -0.20 \pm 0.04$ $\rho_{3-3} = 0.04 \pm 0.03$ $\text{Re}\rho_{10} = 0.00 \pm 0.03$ $\text{Re}\rho_{20} = 0.06 \pm 0.02$ $\text{Re}\rho_{30} = -0.09 \pm 0.02$ $\text{Re}\rho_{21} = -0.13 \pm 0.03$ $\text{Re}\rho_{2-1} = -0.11 \pm 0.03$ $\text{Re}\rho_{31} = -0.05 \pm 0.02$ $\text{Re}\rho_{3-1} = -0.04 \pm 0.03$ $\text{Re}\rho_{32} = -0.13 \pm 0.02$ $\text{Re}\rho_{3-2} = 0.02 \pm 0.02$

## VI. CONCLUSIONS

An investigation of the properties of the  $K(890)$  and  $K(1420)$  mesons has been presented. We have found the mass difference between the neutral and charged  $K^*(890)$  to be  $5.7 \pm 1.7$  MeV. No splitting of the  $K(1420)$  was observed, and its traditionally accepted  $J^P$  of  $2^+$  was confirmed. A new branching ratio for this meson,  $K^*(890)\pi/K\pi = 0.47 \pm 0.08$ , was presented.

A large  $I=0$   $t$ -channel exchange contribution to production of the charged  $K^*$ 's was inferred from the different production properties of the  $K^-p \rightarrow K^*{}^-p$  and  $K^-p \rightarrow K^*{}^0n$  final states. In particular, we used charge independence to compare the  $K^*(890)d\sigma/dt$  and  $\rho_{00}d\sigma/dt$  distributions from these reactions. We suggest that interesting results may be obtained from similar comparisons on these and other conjugate reactions (e.g.,  $\pi^-p \rightarrow \rho^0n$  and  $\pi^-p \rightarrow \rho^-p$ ) as a function of energy.

TABLE XXXI.  $\chi^2$ , degrees of freedom, and probabilities for relevant distribution and spin-parities using the density-matrix elements from Table XXX.

Distribution	$J^P$		$1^-$			$2^+$			$3^-$		
	$\chi^2$	$N$	$\chi^2$	$N$	$P$ (%)	$\chi^2$	$N$	$P$ (%)	$\chi^2$	$N$	$P$ (%)
$\cos\theta$	64.4	38	0.5	28.7	37	83.4	25.6	36	90.1	36	90.1
$\phi$	85.1	38	$\sim 10^{-5}$	61.6	36	0.5	76.6	33	$\sim 10^{-5}$	33	$\sim 10^{-5}$
$\cos\theta - \phi$	102.1	46	$\sim 10^{-6}$	75.0	43	0.2	80.1	34	$\sim 10^{-5}$	34	$\sim 10^{-5}$

TABLE XXXII. Density-matrix elements of the  $K(1420)^-$  produced in the reaction  $K^-p \rightarrow (K\pi)^-p$ .

$J^P$	Density-matrix elements	Confidence levels %	
		$\cos\theta$	$\phi$
$1^-$	$\rho_{00} = 0.58 \pm 0.03$ $\rho_{11} = 0.21 \pm 0.03$ $\rho_{1-1} = 0.30 \pm 0.06$	0.1	8.1
$2^+$	$\rho_{00} = 0.06 \pm 0.06$ (0.10 $\pm$ 0.03) $\rho_{11} = 0.44 \pm 0.04$ (0.45 $\pm$ 0.03) $\rho_{22} = 0.03 \pm 0.04$ (0.00) $\rho_{1-1} = 0.30 \pm 0.06$ (0.30 $\pm$ 0.06) $\rho_{2-2} = -0.17 \pm 0.07$ (0.00) $\text{Re}\rho_{20} = -0.01 \pm 0.04$ (0.00)	24.4 (27.2)	23.6 (8.6)
$3^-$	$\rho_{00} = 0.04 \pm 0.08$ (0.28 $\pm$ 0.04) $\rho_{11} = 0.20 \pm 0.05$ (0.36 $\pm$ 0.04) $\rho_{22} = 0.35 \pm 0.05$ (0.00) $\rho_{33} = -0.07 \pm 0.04$ (0.00) $\rho_{1-1} = 0.29 \pm 0.06$ (0.30 $\pm$ 0.06) $\text{Re}\rho_{31} = 0.00 \pm 0.11$ (0.00) $\text{Re}\rho_{20} = 0.00 \pm 0.03$ (0.00) $\rho_{2-2} = -0.17 \pm 0.08$ (0.00) $\text{Re}\rho_{3-1} = 0.00 \pm 0.04$ (0.00) $\rho_{3-3} = -0.05 \pm 0.06$ (0.00)	20.8 ( $<10^{-8}$ )	11.9 (8.6)

## ACKNOWLEDGMENTS

The constant support, advice, and encouragement of Dr. N. P. Samios are deeply appreciated. We acknowledge the help in many stages of this experiment of Dr. V. E. Barnes, Dr. D. Bassano, Dr. E. Flaminio, Dr. K. Jaeger, and Dr. D. Pandoulas, and numerous discussions with Dr. G. Cohen-

Tannoudji, Dr. L. Gutay, and Dr. G. Kane. We thank Dr. S. U. Chung for many suggestions and enlightening discussions. We thank Mrs. G. Schiro for her typing of this manuscript. We also thank the AGS and 80-in. bubble chamber staffs and crews for their help in obtaining the pictures, and our data-handling personnel for their efforts.

\*Work performed under the auspices of the U. S. Atomic Energy Commission.

†Present address: University of Birmingham, Birmingham, England.

<sup>1</sup>M. Aguilar-Benitez, D. Bassano, R. L. Eisner, J. B. Kinson, N. P. Samios, and V. E. Barnes, *Phys. Rev. Letters* **25**, 1362 (1970); M. Aguilar-Benitez, V. E. Barnes, D. Bassano, R. L. Eisner, J. B. Kinson, and N. P. Samios, *ibid.* **26**, 466 (1971); M. Aguilar-Benitez, R. L. Eisner, J. B. Kinson, N. P. Samios, and J. M. Scarr, BNL Report No. 15707 (unpublished).

<sup>2</sup>See review by J. D. Jackson, *Rev. Mod. Phys.* **42**, 12 (1970).

<sup>3</sup>Data on  $K^*(890)$  production in  $K^-p$  interactions in this energy region have been presented by F. Schweingruber *et al.*, *Phys. Rev.* **166**, 1317 (1968); Y. W. Kang, *ibid.* **176**, 1587 (1968).

<sup>4</sup>The microbarn equivalent was determined from  $\tau$  count which was recorded throughout the experiment. The estimated systematic uncertainty in this number is 10–15%. The quoted errors on the cross sections in the text are only statistical.

<sup>5</sup>For more details on selection procedures and contamination studies in the two-prong-plus-vee topology, see

K. B. Jaeger, Ph.D. thesis, Syracuse University, 1970 (unpublished).

<sup>6</sup>G. Giacomelli *et al.*, *Phys. Letters* **31B**, 321 (1970).

<sup>7</sup>L. Moscoso *et al.*, *Phys. Letters* **32B**, 513 (1970).

<sup>8</sup>P. Astbury *et al.*, *Phys. Letters* **23**, 396 (1966).

<sup>9</sup>J. D. Jackson, *Nuovo Cimento* **34**, 1644 (1964).

<sup>10</sup>Systematic shifts in the absolute mass scale due to the different topologies used in determination of resonance parameters have been studied. The values obtained for  $M$  and  $\Gamma$  for the  $K^{*0}(890)$  in the two-prong topology (i.e., reactions 2 and 3) and in the two-prong-plus-vee topology (reaction 5) are in excellent agreement, which rules out the possibility of differences due to the constraint classes.

<sup>11</sup>The lower limits in momentum transfer for the differential cross-section distributions are 0.007 GeV<sup>2</sup> (0.005 GeV<sup>2</sup>) at 3.9 GeV/c (4.6 GeV/c). These values have been used in order to avoid biases due to the spread of the  $t_{\min}$  distributions caused by the finite width of the  $K^{*0}(890)$ . They correspond to  $|t_{\min}|$  for a  $K\pi$  mass of  $\sim 940$  MeV.

<sup>12</sup>Similar asymmetry in  $K^{*0}(890)$  production was found in the reaction  $K^+p \rightarrow K^{*0}(890)\Delta^{++}$  by T. G. Trippe *et al.*, *Phys. Letters* **28B**, 203 (1968).

<sup>13</sup>This form has been used in analysis of the reaction

$\pi^-p \rightarrow \rho^0 n$ ; see for instance D. H. Miller *et al.*, Phys. Rev. **153**, 1423 (1967).

<sup>14</sup>See review by G. L. Kane, in *Proceedings of the Philadelphia Conference on Experimental Meson Spectroscopy, 1970*, edited by C. Baltay and A. H. Rosenfeld (Columbia Univ. Press, New York, 1970).

<sup>15</sup>An investigation of the scanning bias angle (i.e., the angle between the normal to the production plane and the camera axis) reveals no significant depopulation of events for the regions of momentum transfer shown in the inserts.

<sup>16</sup>We have also performed a fit on the first two bins of momentum transfer including  $S$ - $P$ -wave interference. The results for the resonance density-matrix elements were found to be consistent with those quoted in the text. Additional fits were performed on the high  $K^{*+}(890)$  region, and again the results were consistent with those quoted in the text.

<sup>17</sup>K. Gottfried and J. D. Jackson, Nuovo Cimento **33**, 309 (1964).

<sup>18</sup>M. LeBellac and G. Plaut, Lett. Nuovo Cimento **1**, 721 (1969), have demonstrated that the natural-parity Regge-pole exchange contribution to  $\rho_{00}^H$ , even in the presence of absorption, should vanish as order  $1/s^2$ .

<sup>19</sup>The cross sections have been averaged over the two momenta.

<sup>20</sup>The corresponding  $\chi^2$  are 46.1 (or 63.4) in the region 1.20–1.64 GeV and 13.8 (or 31.2) in the limited region 1.37–1.47 GeV for the Breit-Wigner (or dipole) fits. A series of fits has been performed using an extended region [ $1.00 \leq M(K^-\pi^+) \leq 1.80$  GeV] and various forms for the background. No significant improvement was observed in the  $\chi^2$  probability (calculated in the narrow-mass region) for the dipole hypothesis.

<sup>21</sup>P. J. Davis *et al.*, Phys. Rev. Letters **23**, 1071 (1969).

<sup>22</sup>Unweighted Monte Carlo events were used for this analysis.

<sup>23</sup>Using the values obtained for the mass and width from the ten experimental distributions of Fig. 47(a)–47(j), a  $\chi^2$  compatibility test was performed (with respect to the weighted averaged values  $M = 1419.4 \pm 2.0$  MeV,  $\Gamma = 99.2 \pm 6.4$  MeV), leading to confidence levels 93% and 33%, respectively. A similar test made using the dipole parameters (average values  $M = 1422.3 \pm 1.2$  MeV,  $\Gamma = 27.8 \pm 1.4$  MeV) gave 3% and 65% for the corresponding confidence levels.

<sup>24</sup>The  $\chi^2$  probabilities, for the Breit-Wigner hypothesis, calculated in the restricted mass region 1.37–1.47 GeV are 14.6% and 16.3% for the neutral and charged modes, respectively. Similar confidence levels were calculated for the dipole hypotheses (an average resolution,  $\sigma = 7.5$  MeV, was used), and a value of 0.2% was obtained for both the neutral and charged mass distributions.

<sup>25</sup>We assumed that only quasi-two-body decay modes of the  $K(1420)$  were present. The fit was also performed allowing an uncorrelated  $K\pi\pi$  decay mode without any significant improvement in the likelihood function.

<sup>26</sup>More complicated expressions for the resonance term which takes into account angular momentum barriers (Zemach factors) were considered. The branching ratios so obtained are in close agreement with the ones quoted in the text.

<sup>27</sup>A  $\chi^2$  test on the  $M(\bar{K}^0\pi^-)$  vs  $M(\pi^+\pi^-)$  distribution gave a 12% confidence level.

<sup>28</sup>The systematic uncertainty in the microbarn equivalent does not affect these branching ratios which only depend on the relative pathlength, scanning, and throughput efficiencies.

<sup>29</sup>Particle Data Group, Rev. Mod. Phys. **42**, 87 (1970).

<sup>30</sup>For the  $2^+$  nonet SU(3) analysis [see E. Flaminio *et al.*, BNL Report No. 14572 (unpublished)] the input parameters (mass, width, and decay rates) were taken from: (a) for the  $A_2$ , M. Alston-Garnjost *et al.*, Phys. Letters **34B**, 156 (1971); (b) for the  $K(1420)$ , the present work; (c) for the  $f^0$ , Particle Data Group, Phys. Letters **33B**, 1 (1970); and (d) for the  $f^*$ , V. E. Barnes *et al.*, Phys. Rev. Letters **19**, 964 (1967).

<sup>31</sup>The fits were performed in the region  $1.1 \leq M(K\pi) \leq 1.8$  GeV with  $K(1420)^-$  mass and width fixed at the values given in Sec. V 1. Second-order polynomial forms in the mass were used as backgrounds. The number of resonance events and the total corrected  $(K\pi)^-$  cross sections so obtained were as follows.

3.9 GeV/c, reaction 2:  $289 \pm 40$  events;  $222 \pm 31 \mu\text{b}$ .  
 reaction 3:  $297 \pm 40$  events;  $171 \pm 23 \mu\text{b}$ .  
 reaction 5:  $251 \pm 31$  events;  $181 \pm 22 \mu\text{b}$ .  
 4.6 GeV/c, reaction 2:  $152 \pm 33$  events;  $209 \pm 45 \mu\text{b}$ .  
 reaction 3:  $125 \pm 28$  events;  $129 \pm 29 \mu\text{b}$ .  
 reaction 5:  $206 \pm 31$  events;  $132 \pm 20 \mu\text{b}$ .

<sup>32</sup>K. Gottfried and J. D. Jackson, Nuovo Cimento **33**, 309 (1964).

<sup>33</sup>G. Bassompierre *et al.*, Nucl. Phys. **B13**, 189 (1969).

<sup>34</sup>The advantage of using simultaneously the  $K\pi$  and  $K^*(890)\pi$  decay modes of the  $K(1420)$  in order to obtain information on the  $J^P$  has been pointed out in Ref. 33. However, the  $K(890)\rho$  overlap in the  $K(1420)$  decay Dalitz plot makes it difficult to extract a clean sample of  $K(890)\pi$  events and, moreover, our  $K^*\pi/K\pi$  decay rate is such that the number of expected events in the  $K^*\pi$  mode is considerably diminished. In particular, the sample which gives the best information on the spin-parity [reaction  $K^-\bar{p} \rightarrow K(1420)^-\bar{p} \rightarrow (K\pi)^-\bar{p}$  in the momentum-transfer interval  $0.5 \leq |t'| \leq 2.0$  GeV<sup>2</sup>] consists of  $419 \pm 38$  resonance events [in the region  $1.32 \leq M(K\pi)^- \leq 1.52$  GeV]. Using our branching ratios, Clebsch-Gordan coefficients, and different microbarn equivalents for the different topologies, we expected to find  $140 \pm 30$   $K(1420)$  events in the reaction  $K^-\bar{p} \rightarrow K^-\pi^+\pi^-\bar{p}$  in the same mass and momentum-transfer intervals after requiring  $0.84 \leq M(K^-\pi^+) \leq 0.94$  GeV. We have investigated this mass spectrum (which is relatively free of the  $Q$  effect due to the antiperipheral selection) and found  $110 \pm 35$  events and a rather weak signal-to-noise ratio ( $\sim 0.24$ ). The reduced number of events, together with the large background present, makes the determination of the density-matrix elements unreliable and subject to large systematic uncertainties so that the three-body decay modes of the  $K(1420)$  were not considered for the  $J^P$  analysis.

<sup>35</sup>It is important to realize, with the present noninterference assumption, that it is impossible to fix all the diagonal elements at physical values (for the  $2^+$  and  $3^-$  hypotheses) and at the same time obtain a reasonable representation of the data. This feature does not significantly depend on the uncertainties in the amount or parametrization of the background. A similar situation occurs in the reaction  $\pi^-p \rightarrow f^0 n$ ; see, for instance, Y. Y. Lee *et al.*, Phys. Rev. Letters **12**, 342 (1964).